

Global Structure of the Mantle Transition Zone Discontinuities and Site Response Effects in the Atlantic and Gulf Coastal Plain

Zhen Guo

Dissertation submitted to the Faculty of the
Virginia Polytechnic Institute and State University
in partial fulfillment of the requirements for the degree of

Doctor of Philosophy
in
Geosciences

Ying Zhou, Chair
Martin C. Chapman
John A. Hole
Julianne Chung

August 14, 2019
Blacksburg, Virginia

Keywords: mantle transition zone, body waves, mantle return flow, site response, ground
motion prediction

Copyright ©2019, Zhen Guo

Global Structure of the Mantle Transition Zone Discontinuities and Site Response Effects in the Atlantic and Gulf Coastal Plain

Zhen Guo

(ABSTRACT)

This dissertation focuses on two different topics in seismology: imaging the global structures of the mantle transition zone discontinuities and studying the site response effects in the Atlantic and Gulf Coastal Plain.

Global structures of the mantle transition zone discontinuities provide important constraints on thermal structures and dynamic processes in the mid mantle. In this dissertation, global topographic structures of the 410- and 660-km discontinuities are obtained from finite-frequency tomography of SS precursors. The finite-frequency sensitivities of SS waves and precursors are calculated based on a single-scattering (Born) approximation and can be used for data selection. The new global models show a number of smaller-scale features that were absent in back-projection models. Good correlation between the mantle transition zone thickness and wave speed variations suggests dominantly thermal origins for the lateral variations in the transition zone.

The high-resolution global models of the 410- and 660-km discontinuities in this dissertation show strong positive correlation beneath western North America and eastern Asia subduction zones with both discontinuities occurring at greater depths. Wavespeed and anisotropy models support vertical variations in thermal structure in the mid mantle, suggesting return flows from the lower mantle occur predominantly in the vicinity of stagnant slabs and the region overlying the stagnant slabs. In oceanic regions, the two discontinuities show a weak anti-correlation, indicating the existence of a secondary global far-field return flow.

The Atlantic and Gulf Coastal Plain is covered by extensive Cretaceous and Cenozoic marine sediments. In this dissertation, the site response effects of sediments in the Coastal

Plain region relative to the reference condition outside that region are investigated using Lg and coda spectral ratios. The high-frequency attenuation factors (κ) in the Coastal Plain are strongly correlated with the sediment thickness. At frequencies between 0.1-2.86 Hz, the Lg spectral ratio amplitudes are modeled as functions of frequency and thickness of the sediments in the Coastal Plain. Analysis of the residuals from the stochastic ground motion prediction method suggests that incorporating the site response effects as functions of sediment thickness may improve ground motion prediction models for the Coastal Plain region.

Global Structure of the Mantle Transition Zone Discontinuities and Site Response Effects in the Atlantic and Gulf Coastal Plain

Zhen Guo

(GENERAL AUDIENCE ABSTRACT)

The mantle transition zone is the region in the Earth's interior between depths of ~ 410 km and ~ 660 km. The structure of the mantle transition zone plays an important role in understanding temperature variations and mass exchanges in the interior of the Earth. This dissertation aims at resolving depth variations of the top and bottom boundaries of the mantle transition zone at a global scale using underside reflected seismic waves. The advanced method used here resolved stronger small-scale depth variations of the boundaries than a conventional method using the same dataset. The two mantle transition zone boundaries both occur at depths greater than the global average beneath eastern Asia and western North America where cold oceanic lithosphere subducted under the continents. This positively correlated behaviors of the two boundaries agree with a scenario where cold subducted slabs have been horizontally deflected and stagnant above the bottom boundary of the mantle transition zone while hot materials beneath the mantle transition zone flow upwards due to the stagnant slabs penetrating the bottom boundary of the mantle transition zone. This dissertation also provides an examination of the differences between response of earthquake ground shaking in the Atlantic and Gulf Coastal Plain and that outside the Coastal Plain using seismic-wave spectral ratios. Ground shaking in the Coastal Plain is found to be amplified at low frequencies and de-amplified at high frequencies relative to that outside the Coastal Plain due to the extensive marine sediments in the Coastal Plain region. The amplification and attenuation factors can be estimated from spectral ratios and are found to be strongly correlated with the sediment thickness in the Coastal Plain. The spectral ratio functions derived in this dissertation may be adopted by studies on analyzing the seismic hazard in the Central and Eastern United States.

Acknowledgments

Pursuing the Ph.D degree in geosciences in Virginia Tech has been a precious and unforgettable experience for me. During my graduate study, I received tremendous help, support and encouragement from a lot of people that lead me to the successful defense.

First of all, I would like to thank my advisors Dr. Ying Zhou and Dr. Martin C. Chapman for their great patience and thoughtful guidance. I'm truly grateful for being able to work with Dr. Zhou on global seismology. She has been inspiring and guiding me to be prepared as a seismologist. I have benefited a lot from her professional skills and solid knowledge. Dr. Chapman has also been a great mentor for me. He guided me into the fields of ground motion predictions and analyzing seismic sources. It has been an honor working with such a knowledgeable professor as him. I also want to thank my committee members, Dr. Julianne Chung and Dr. John A. Hole, for their continuous support and constructive suggestions on my Ph.D researches.

I would like to thank other faculty members in the Department of Geosciences, Dr. Scott King, Dr. James Spotila, Dr. Sarah Stamps and Dr. Robert Weiss for their informative lectures and instructive discussions.

I also want to express my great gratitude to Geosciences staffs Sharron Collins, Mark Lemon, Connie Lowe, Mary McMurray, Mary Jane Smith and Jo Thomason for their support

and help during my graduate study in Derring Hall.

Many thanks to my fellow graduate students Amin Abbasi Baghbadorani, Jessica DePaolis, Joshua Jones, Shangxin Liu, Tahiry Rajaonarison, Tyler Rasmussen, Shuyang Sun and Hao Wu for their encouragement and help. I also want to thank my dear friends Liang Han, Kannikha Kolandaivelu and Qimin Wu for their support and help during my researches. I have been enjoying the chatting and discussions with them.

I would like to express my deep gratitude to my mom, dad and brothers. They have always been there supporting and comforting me. My parents have spared no effort to encourage me to fulfill my dreams. I also want to thank my sister in-law for taking care of my family. Finally, I would like to deeply thank my husband, Hongrong Wu, who has been continuously supporting and helping me during my graduate life. With his patient and gentle encouragements, he has been helping me live through difficult times.

Contents

Abstract	ii
General Audience Abstract	iv
Acknowledgments	v
List of Figures	x
List of Tables	xxiii
1 Introduction	1
1.1 Global Structure of the Mantle Transition Zone Discontinuities	1
1.2 Site Response Effects in the Atlantic and Gulf Coastal Plain	4
1.3 Summary of Dissertation Chapters	6
Bibliography	9
2 Finite-Frequency Imaging of the Global 410-km and 660-km Discontinuities Using SS Precursors	14
2.1 Introduction	14

2.2	Finite-Frequency Traveltime Measurements	17
2.3	Finite-Frequency Sensitivities to Boundary Perturbations	18
2.4	The Inverse Problem	21
2.5	Finite-Frequency Effects in Discontinuity Imaging	22
2.6	Crust and Mantle Corrections	24
2.7	Discontinuity Topography and Wavespeed Structure	27
2.8	Comparison with Previous Global Models	29
2.9	Conclusions	30
	Bibliography	32
3	Global Return Flow above Stagnant Slabs from Mantle Transition Zone	
	Tomography	54
3.1	Introduction	54
3.2	Data and Methods	56
3.2.1	Finite-frequency sensitivity kernels	58
3.2.2	The inverse problem	58
3.3	The Global Subduction Zones	59
3.4	Global Return Flow above Stagnant Slabs	61
3.5	Structures in Global Oceanic Regions	63
3.6	Comparison with Previous Global Models	64
3.7	Conclusions	65
	Bibliography	67

4 Using Spectral Ratios to Examine Amplification and Attenuation Effects in the Atlantic and Gulf Coastal Plain	84
4.1 Introduction	84
4.2 Data and Analysis	90
4.3 Quantifying Site Response as a Function of Sediment Thickness	99
4.4 Target Spectra for the Stochastic Method and Evaluation of the Site Response Model Using Residual Analysis	102
4.5 Conclusions	108
Bibliography	109

List of Figures

2.1	Ray paths of SS , $S410S$ and $S660S$ waves at epicentral distances of 110° and 150° . The star and triangles indicate locations of the earthquake event and the recording stations, respectively.	37
2.2	(a) Distribution of 1117 teleseismic earthquakes ($6.0 < M_w < 8.5$) used in this study. The epicentral distance of the dataset ranges from 90° to 160° . (b) Locations of 150 GSN stations used in this study.	38
2.3	(a) and (b) are a 100-second cosine taper in the time domain and its spectrum in the frequency domain, respectively. (c) Example observed and synthetic seismograms with clear SS , $S410S$ and $S660S$ waves, recorded at station EFI (longitude= -58.06° , latitude= -51.68°) for a 2003 Indonesia earthquake ($M_w = 6.9$). The shaded areas indicate time windows used for traveltime measurements.	39
2.4	(a) Bird-eye view of example finite-frequency sensitivity of an $S410S$ wave at a period of 20 seconds to depth perturbations of the 410-km discontinuity. The epicentral distance is 133° and the mapview of the sensitivity kernel is plotted in (c) where the earthquake (star) is located off the west coast of Mexico and the station LBTB (triangle) is in Africa. The sensitivity of the corresponding $S660S$ to depth perturbations on the 660-km discontinuity is plotted in (b) and (d).	40

2.5	Zoom-in view of sensitivity kernels of $S410S$, $S660S$ and SS waves recorded at station BJT (longitude= 116.17° , latitude= 40.02°) with an epicentral distance of 120° from a M_w 6.3 earthquake in Puerto Rico area. The SS sensitivities are much smaller in magnitude and plotted on difference color scales. SdS and SS waves have different sensitivity polarity as a depression of the 410-km (or 660-km) discontinuity will speed up SdS waves but slow down SS waves, and vice versa for an uplift.	41
2.6	Finite-frequency effects in imaging depth perturbations of the 410-km and the 660-km discontinuities. (a) depth perturbations of the 410-km discontinuity inverted from SdS - SS traveltime measurements using finite-frequency sensitivity kernels. (b) and (c) are ray-theoretical back-projection models where perturbations are averaged in a moving circular cap with a radius of 6° (BP1) and 4° (BP2). (d)–(f) are the finite-frequency and ray-theoretical back-project models for depth perturbations on the 660-km discontinuity. The finite-frequency model and ray-theoretical back-project models are obtained using the same traveltime data without crustal and mantle wavespeed corrections.	42
2.7	(a) is the sensitivity density (diagonal elements of the matrix $A^T A$) in finite-frequency tomography of the 410-km discontinuity. (b) and (c) are the number of traces per circular cap in the back-projection models BP1 and BP2, respectively. (d)–(f) are the same as (a)–(c) but for the 660-km discontinuity models in Fig. 2.6.	43
2.8	(a) Correlation coefficient as a function of spherical harmonic degree between the finite-frequency 410-km discontinuity model and the two back-projection models in Fig. 2.6. (b) Same as (a) but for the 660-km discontinuity models.	44

2.9	(a) and (b) are $S410S-SS$ and $S660S-SS$ differential traveltimes measurements at a period of 20 s without crustal and mantle corrections. The measurements are plotted at the bounce points of SS waves. (c) and (d) are the same as (a) and (b) but with data corrected for crustal and mantle wavespeed variations using models CRUST1.0 and S40RTS. (e) and (f) are the same as (c) and (d) but with mantle corrections using model S362ANI+M.	45
2.10	(a) Scatterplot of $S410S-SS$ differential traveltimes measurements with mantle corrections made using model S40RTS (Ritsema et al., 2011) and model S362ANI+M (Moulik & Ekstrom, 2014). (b) and (c) are depth perturbations of the 410-km discontinuity from finite-frequency tomography with traveltimes corrections made using model S40RTS and S362ANI+M, respectively. (d)-(f) are the same as (a)-(c) but for the 660-km discontinuity.	46
2.11	(a) spectra power per spherical harmonic degree of the finite-frequency 410-km and 660-km discontinuity models in Fig. 2.6 and the corresponding mantle transition zone thickness. (b) and (c) are the same as (a) but for discontinuity models in Fig. 2.10 where traveltimes corrections have been made using model S40RTS and S362ANI+M respectively. (d) Correlation coefficients as a function of spherical harmonic degree between the discontinuity models obtained with and without corrections based on model S40RTS (Figs 2.6 & 2.10). (e) is the same as (d) for models with and without traveltimes corrections made using model S362ANI+M. (f) correlation coefficients between models obtained with corrections made using models S40RTS and S362ANI+M.	47

2.12	(a) and (c) are the finite-frequency 410-km and 660-km discontinuity models with data corrections made using model S40RTS (Fig. 2.10). (b) and (d) are wavespeed perturbations in model S40RTS at depths of 410 and 660 km, respectively. (e) and (f) are maps of the mantle transition zone thickness and average wavespeed in the mantle transition zone, respectively. (g) correlation between discontinuity depth perturbations and wavespeed perturbations as a function of spherical harmonic degree; (f) correlation between the 410-km and 660-km discontinuity models in 1-D (no correction) and 3-D (with correction) wavespeed models.	48
2.13	Average mantle transition zone thickness in 1-D (left) and 3-D (right) wavespeed models. In the oceans, the thickness is averaged over every 20-million year age band and there is no apparent dependence on the age of the sea floor. The average thickness of the mantle transition zone in continental areas is calculated for Asia (AS), Europe (EUR), North America (NA), South America (SA), Africa (AFR) and Australia (AUS). The mantle transition zone is thicker under the continents than under the oceans, especially after crustal and wave speed corrections are applied.	49
2.14	This figure compares the topography of the 410-km and 660-km discontinuity as well as the thickness of the mantle transition zone from (a)-(c) this study, (d)-(f) Lawrence & Shearer (2008), (g)-(i) Gu et al. (2003) and (j)-(l) Houser et al. (2008).	50
2.15	Correlation between discontinuity models in this study and model LS08 (Lawrence & Shearer, 2008). The coefficients are plotted as function of spherical harmonic degree from 1 to 20 for depth perturbations on the 410-km discontinuity, the 660-km discontinuity and the thickness of the mantle transition zone.	51

2.16	(a) the 410-km discontinuity model in this study filtered to spherical harmonic $l \leq 2$, $l \leq 6$ and $l \leq 12$. (b) is the same as (a) but for the 410-km discontinuity model from Lawrence & Shearer (2008). (c) and (d) are the same as (a) and (b) but for the 660-km discontinuity.	52
2.17	Same as Fig. 2.16 but for models from Gu et al. (2003) and Houser et al. (2008).	53
3.1	Tradeoff curves of the inverse problem $(\mathbf{G}^T \mathbf{G} \mathbf{m} - \mathbf{G}^T \mathbf{d}) + \alpha^2 \mathbf{m} = 0$ with a varying Tikhonov regularization parameter α . The horizontal axis is $\ \mathbf{m}\ $ and vertical axis is $\ \mathbf{G}^T \mathbf{G} \mathbf{m} - \mathbf{G}^T \mathbf{d}\ $. The optimal models plotted in Fig. 3.3 are indicated by stars.	72
3.2	(a) and (b) are resolutions of the 410-km and 660-km discontinuity models in Fig. 3.3, plotted in every $4^\circ \times 4^\circ$ grid cell based on diagonal elements of the resolution matrix \mathbf{R} . (c) and (d) are the corresponding sensitivity density (diagonal elements of the matrix $\mathbf{G}^T \mathbf{G}$).	73

3.3	<p>(a) and (b) are global depth perturbations of the 410-km and 660-km discontinuities imaged from finite-frequency tomography of S410S-SS and S660S-SS differential traveltimes measurements. (c) correlation between the 410-km and 660-km discontinuity depth perturbations represented by the sum of the absolute perturbations at the two discontinuities. The correlation is positive (in blue) in regions where both the 410-km and 660-km discontinuities occur at depths greater than the global average; and is negative (in red) in region where the 410-km discontinuity is deeper while the 660-km discontinuity is shallower (typical anti-correlation signature for mantle plumes). Only regions with both discontinuity depth perturbations larger than uncertainties (5 km) are plotted. (d)–(f) are the same as (a)–(c) but models obtained using traveltimes measurements corrected for 3-D seismic structure in the crust (CRUST1.0) as well as wavespeed variations in the mantle (S40RTS).</p>	74
3.4	<p>Circum-Pacific positive correlation between the 410 and the 660. (a) correlation between the 410 and the 660 depth perturbations represented by the sum of their absolute perturbations. The correlation is positive (in blue) in regions where both discontinuities occur at depths greater than the global average; and is negative (in red) in region where the 410 is deeper while the 660 is shallower (typical anti-correlation signature for mantle plumes). Only regions with both perturbations larger than uncertainties (5 km) are plotted. (b) the same as (a) but obtained using traveltimes measurements corrected for 3-D wavespeed structure in the crust (CRUST1.0) and mantle (S40RTS). . .</p>	75

3.5	Tomographic resolution tests for the 410-km and 660-km discontinuity models in Fig. 3.3. The input models have a spherical harmonic structure, with degree $l = 12$ (top) and $l = 20$ (bottom), respectively. We generate synthetic data using the input models and finite-frequency sensitivity kernels for the same earthquake-station configuration, and the output models are obtained with the same inversion regularization parameters as used for the real data. We have added 20% of random noise in all synthetic data in the resolution tests.	76
3.6	(a)–(f) are global models of the 410 km and 660-km discontinuities LS08 (Lawrence & Shearer, 2008), H08 (Houser et al., 2008) and G03 (Gu et al., 2003). (g)–(i) are correlations maps calculated as in Fig. 3.4.	77
3.7	Warm mantle above stagnant slab in the Western US. (a) and (b) are S-wave velocity perturbations at depths of 400 km and 650 km, respectively (Tian et al., 2011). (c) correlation between the 410 and the 660 in the Western US, only regions with consistent anomalies in Fig. 3.4(a) and (b) are plotted. (d) average radial anisotropy in the MTZ in model US22 (Zhu et al., 2017) where negative ($V_{SH} < V_{SV}$) radial anisotropy indicates dominant vertical mantle flow. Dark red lines are major geological boundaries; black dashed line indicates subduction front in the MTZ. 3-D wavespeed model in the red box red in (a) and (b) is plotted in Fig. 3.8.	78

3.8	3-D wavespeed structure in the Western US and Cartoon illustration of subduction with stagnant slab (a) 3-D rendering of S-wave slab anomalies in the Western US. The isosurface represents 1% fast and slow seismic wavespeed anomalies at depths from 50 km to 1600 km US State boundaries are plotted at the surface for geographic reference. Fast anomalies in the upper mantle beneath the craton have been removed for better illustration of the slab. (b) Cartoon (not to scale) illustrating the sinking of a stagnant slab from the mantle transition zone into the lower mantle. The blue triangle indicates the <i>trench</i> in the MTZ. The 660-km discontinuity occurs deeper (not illustrated) due to the cold stagnant slab in the lower MTZ and the 410-km discontinuity also occurs at greater depths (not illustrated) due to warm return flows in a super adiabatic mantle and possible <i>trench retreat</i> in the MTZ.	79
3.9	Warm mantle above stagnant slab in Eastern Asia. (a) and (b) are S-wave velocity perturbations at depths of 400 km and 650 km from Schaeffer and Lebedev (2013). (c) correlation between the 410 and the 660 in Eastern Asia, only regions with consistent anomalies in Fig. 3.4 (a) and (b) are plotted. (d) average radial anisotropy in the MTZ in model SGLOBE-rani (Chang et al., 2014), where negative radial anisotropy ($V_{SH} < V_{SV}$) indicates dominant vertical mantle flow. Two dashed lines indicate subduction systems in the MTZ, roughly parallel to the present-day Ryukyu trench.	80
3.10	The Hess Rise (HR) anomaly. (a) and (b) are correlations between the 410-km and 660-km discontinuity depth perturbations in the Pacific (same as Fig. 3.4a and b); (c) the same correlation calculated using discontinuity models published by Lawrence and Shearer (2008). The anomaly west of the island of Hawaii (HW) becomes much weaker after wave speed corrections. The <i>plume-like</i> structure south of Hess Rise (HR) is a consistent feature in all three models.	81

3.11	The 410 and the 660 in oceanic regions. (a) depth perturbations of the 410 and the 660 in global oceanic regions, averaged over every 20-million year age band; (b) the same as (a) but for models inverted using travelttime data corrected using model CRUST1.0 and S40RTS	82
3.12	(a) depth perturbations of the 410-km and 660-km discontinuities in global oceanic regions, averaged over every 20-million year age band in models inverted using travelttime data corrected for 3-D crust and mantle wavespeed structures (S40RTS). (b) thickness of the MTZ as a function of seafloor age in global oceanic regions. (c) and (d) are the same as (a) and (b) but for models inverted with travelttime measurements corrected using model S362ANI+M.	83
4.1	Geologic map of the central and eastern United States. Locations and station codes of the Earthscope Transportable Array (TA) stations (triangles), the United States National Seismic Network (US) stations (hexagons), the Central and Eastern US Network (N4) stations (circles), the Lamont-Doherty Cooperative Seismographic Network (LD) stations (stars) and the Southeastern Suture of the Appalachian Margin Experiment (Z9) stations (diamonds) used in this study are indicated. The thick solid curve shows the boundary of the Atlantic and Gulf Coastal Plain. Adapted from Garrity & Soller (2009).	115
4.2	Epicenters of earthquakes (circles) used in this study. Sizes of the circles are scaled to the moment magnitude listed in Table 4.1.	116

4.3 (a) Horizontal-component acceleration seismograms recorded at station 440A in eastern Texas and station N35A in eastern Nebraska, from the Mw 5.65 06 November 2011 earthquake in Oklahoma. The stations are at a distance of ~ 590 km. The shaded areas from left to right denote the windows used for calculating Lg and coda spectra respectively. (b) Corresponding geometric mean of coda and Lg spectra from the two horizontal recordings at station 440A and station N35A using the windows defined in (a). (c) and (d) are the same as (a) and (b) but recorded at station W02 in northern Florida and station T56A in western Virginia, from the Mw 4.11 15 February 2014 earthquake in South Carolina, with epicentral distance of ~ 390 km. (e) and (f) are the same as (a) and (b) but recorded at station 438A in southeastern Texas and station 433A in the Llano uplift of central Texas, from the Mw 4.33 13 October 2010 earthquake in Oklahoma, with epicentral distance of ~ 500 km. 117

- 4.4 In the top panel, (a) shows the geometric mean of Fourier acceleration amplitude spectra for horizontal-component coda waves, computed from a 20 s window at a lapse time of 334 s after the origin time of the 06 November 2011 Prague earthquake in Oklahoma. The black line and gray line are computed from coda waves recorded at Coastal Plain stations 440A and Z41A, underlain by sediments of thickness ~ 8 km and ~ 2.5 km respectively. The thicker line is the mean coda reference spectrum computed for non-Coastal Plain stations. (b) Ratios of coda spectra at station 440A (black) and station Z41A (gray) shown in (a), to the mean reference spectrum (thicker line in (a)). The solid line segments indicate the frequency ranges of spectral ratios used for linear regression (thicker lines). (c) and (d) are the same as (a) and (b) but for coda waves from the 15 February 2014 South Carolina earthquake recorded at station W02 with sediment thickness ~ 2.5 km and station W21 with ~ 0.5 km of sediment. Coda spectra are calculated at a lapse time of 280 s after the event origin time. (e) and (f) are the same as (a), (b) but for coda waves from the 13 October 2010 Oklahoma earthquake recorded at station 438A with sediment thickness ~ 8.0 km and station Z38A with ~ 3.0 km of sediment. Coda spectra are calculated at a lapse time of 225 s after the event origin time. 118
- 4.5 Differential kappa (δk) from linear least square regression of coda spectral ratios in this study (dots) and Lg kappa from Chapman and Conn (2016) (crosses) versus thickness of the post-Jurassic marine sedimentary section. Outliers at the 5% and 95% level from an initial regression were removed for the final regression results shown here. Solid line shows the least-square regression fit to both data sets, $\delta k = e^{-2.932} Z^{0.339}$ (regression model: $\ln(\delta k) = (-2.932 \pm 0.029) + (0.339 \pm 0.020)\ln(Z)$), where Z is the thickness of Coastal Plain marine sediment in km. The dashed lines are the 84 percentile and 16 percentile levels, calculated by adding and subtracting the regression standard error of estimate to the log-log data fit. 119

4.6	(a) Shear wave velocity and Q versus depth assumed for the Coastal Plain (5 km sediment thickness). (b) Same as (a) for 12 km sediment thickness. (c) Differential kappa (δk) values for the assumed model (dots), compared to observed δk and Lg kappa values (crosses).	120
4.7	Natural logarithms of Lg spectra amplitude ratios versus sediment thickness, averaged over 8 frequency bands. The thick solid lines indicate the piecewise linear regression model fit to the data. The corresponding 84 percentile and 16 percentile levels were calculated by adding and subtracting the regression standard error of estimate to the means, and are indicated by the dashed lines. The lower figure is zoomed into a smaller thickness range for a better view of the transition thickness (triangle).	121
4.8	Natural logarithms of Lg spectra amplitude ratios (crosses) averaged in 4 successive frequency bins versus sediment thickness, compared to predicted amplitude ratios (dots) based on equation (4.9) with the δk model in equation (4.11). The shaded area shows the 84 percentile and 16 percentile range of the predicted amplitude ratios, based on the 16–84 percentile range of the δk model calculated by adding and subtracting the regression standard error of estimate to the log-log data fit (Equation 4.10).	122
4.9	Lg spectral ratios $Ratio(f, Z)$ from equations (4.15) and (4.16) with parameters listed in Table 4.4 for frequencies less than 2.86 Hz. Higher frequency values are from equations (4.29) and (4.11). At the bottom, the shaded region indicates the area bounded by the 16 percentile and 84 percentile levels for the ratio function with different sediment thickness.	123
4.10	Uncorrected and corrected Coastal Plain station residuals and reference station residuals at different frequencies plotted versus distance and Coastal Plain sediment thickness for the 08 November 2011 earthquake in central Oklahoma.	124
4.11	Same as Figure 4.10 but for the 08 April 2011 Arkansas earthquake.	125

4.12	Same as Figure 4.10 but for the 10 November 2012 Kentucky earthquake.	126
4.13	Same as Figure 4.10 but for the 20 October 2011 Texas earthquake.	127
4.14	Same as the last two rows in Figure 4.13 except that the residuals at reference stations (open circles) have been corrected for the attenuation effects of the sediments near the earthquake source. The sediment thickness at the epicenter is 5.5 km.	128
4.15	Mean residuals as a function of frequency for earthquake numbers 01-06 in Table 4.1. At each frequency, the mean residual is obtained by averaging all the residuals at the Coastal Plain stations or at the reference stations respectively.	129
4.16	Same as Figure 4.15 but for earthquake numbers 07-12 in Table 4.1.	130
4.17	Same as Figure 4.15-4.16 but for earthquake numbers 13-17 in Table 4.1.	131
4.18	Mean residuals as a function of frequency for earthquake numbers 10 and 13 in Table 4.1 (located in the Coastal Plain of Texas). At each frequency, the mean residual is obtained by averaging all the residuals at the Coastal Plain stations or at the reference stations respectively. The residuals at reference stations outside the Coastal Plain have been corrected for attenuation effects of the sediments near the source.	132

List of Tables

4.1	Earthquakes Used in This Study	133
4.2	Network Instruments Used in This Study	134
4.3	Number of Recordings for Each Earthquake Used in This Study	135
4.4	Linear Regression Coefficients of Natural Logarithms of Lg Fourier Spectra Amplitude Ratios as a Function of Sediment Thickness in Kilometers	136
4.5	Linear Regression Coefficients of Natural Logarithms of Lg Fourier Spectra Amplitude Ratios as a Function of Sediment Thickness in Kilometers at the 84 percentile level	137
4.6	Linear Regression Coefficients of Natural Logarithms of Lg Fourier Spectra Amplitude Ratios as a Function of Sediment Thickness in Kilometers at the 16 percentile level	138
4.7	Seismic stations in the Coastal Plain	139

Chapter 1

Introduction

This dissertation focuses on two different topics in seismology: imaging the global structures of the mantle transition zone discontinuities using SS precursors and studying the site response effects in the Atlantic and Gulf Coastal Plain using Lg and coda Fourier amplitude spectral ratios.

1.1 Global Structure of the Mantle Transition Zone Discontinuities

The mantle transition zone is the region separating the upper and lower mantle, bounded by two global seismic discontinuities at depths of about 410 and 660 km. It has been commonly accepted that the 410- and 660-km discontinuities are caused by pressure-induced phase transitions of olivine (Ringwood, 1975; Anderson, 1967; Ita & Stixrude, 1992). Phase transition of olivine to wadsleyite happens at a depth of about 410 km with a positive Claypeyron slope while ringwoodite transforms to prevskite and magnesiowustite at about 660 km depth with a negative Claypeyron slope (Helffrich, 2000; Ye et al., 2014). Thermal and compositional variations in the transition zone will change the exact depths of the 410-

and 660-km discontinuities at which the phase transitions occur. For example, the 410-km discontinuity will be elevated and the 660-km discontinuity will be depressed in the presence of low-temperature anomalies such as cold subducting oceanic plates. Hot anomalies (e.g. high-temperature upwellings) in the transition zone will depress the 410-km discontinuity but elevate the 660-km discontinuity. Depth perturbations of the two mantle transition zone discontinuities and the variations in mantle transition zone thickness have been observed in global studies since the 1990s and have been used to study thermal heterogeneities in the mantle transition zone (Shearer, 1991; Flanagan & Shearer, 1998; Gu et al., 2003; Lawrence & Shearer, 2006; Houser et al., 2008).

Resolving the lateral undulations on the 410- and 660-km discontinuities with high resolution are important for understanding the thermal structures and dynamical processes in the mid mantle. For example, the style of mantle convection may be determined by the nature of the 660-km discontinuity which is generally considered a possible barrier for whole mantle convection due to its negative Clapeyron slope (Christensen, 1996; Deuss, 2009). A major motivation in this dissertation is to study the less-constrained convection patterns in the mid- and lower mantle from high-resolution topographic maps of the mantle transition zone boundaries.

A variety of techniques can be applied to image the topographies on the 410- and 660-km discontinuities, including P-to-S converted waves (Shen et al., 1996; Li & Yuan, 2003; Gao & Liu, 2014; Zhou, 2018; Lawrence & Shearer, 2006), multiple-ScS reverberations (Niu et al., 2000; Wang et al., 2017) and PP/SS precursors (Shearer, 1991; Shearer & Masters, 1992; Shearer, 1993; Shearer et al., 1999; Xu et al., 1998; Gu & Dziewonski, 2002; Gu et al., 2003; Chambers et al., 2005; Deuss, 2009). PP and SS precursors are underside reflected PP and SS waves off the seismic discontinuities and arrive earlier than the PP and SS waves in the seismograms. PP and SS precursors are highly sensitive to the structures near the bounce point, which is approximately half way between the source and receiver, thus can provide better coverage in oceanic regions than P-to-S converted waves. Compared with SS precursors, the PP precursors typically have much lower amplitude and are less detectable

(Estabrook & Kind, 1996; Deuss, 2009; Lessing et al., 2014). This dissertation focuses on the SS precursors because of their relatively high signal-to-noise ratios and good global coverage.

Previous SS precursor studies on imaging the global 410- and 660-km discontinuities are mostly based on conventional ray theory (Flanagan & Shearer, 1998; Gu & Dziewonski, 2002). When the scale length of anomalies becomes smaller than the width of the first Fresnel zone of SS precursors, ray theory breaks down and wave-front healing, scattering and other finite-frequency effects become significant. Therefore, the resolution in previous global 410 and 660 topographic models is limited by the large Fresnel zone of SS precursors (~ 1000 km at 20 s). To improve the resolution of small-scale features in the topographies, finite-frequency effects of the SS precursors have to be accounted for. Over the years, efforts have been made to calculate the sensitivities of the SS precursor to the depth perturbations of the corresponding discontinuity (Neele & de Regt, 1999; Dahlen, 2005). Lawrence & Shearer (2008) published the first global finite-frequency topographic models of the 410- and 660-km discontinuities using finite-frequency sensitivity kernels of SS precursors calculated based on ray tracing (Dahlen, 2005).

In this dissertation, we calculate sensitivities of the SS precursors to the topographic variations of the 410- and 660-km discontinuities in the framework of traveling-wave mode coupling. The finite-frequency sensitivity kernels take into account wave diffractive effects and phase interactions within the measuring window, which are then used to invert for high-resolution topographic maps of the 410- and 660-km discontinuities. The new finite-frequency 410 and 660 models provide important constraints on the convection in the mid mantle.

1.2 Site Response Effects in the Atlantic and Gulf Coastal Plain

The near surface structures of the Atlantic and Gulf Coastal Plain in the southern and southeastern United States are characterized as a series of Cretaceous and Cenozoic sedimentary formations (Salvador, 1991; Thomas et al., 1989). The landward limit of the Atlantic Coastal Plain sediments is marked by the Fallline which lies in the Piedmont province with a northeastern orientation. Sedimentary units in the Atlantic Coastal Plain form a seaward thickening wedge with maximum thickness reaching ~ 2 km. Basement rocks beneath the sediments in the Atlantic Coastal Plain are basically Paleozoic rocks which are the same as the exposed rocks in the Piedmont region. The Gulf Coastal Plain roughly extends westwards from Alabama to Texas with the sediments dipping towards the Gulf of Mexico. Along the axis of the Mississippi embayment, the sediment thickness is the greatest and reaches to 10 km near the Gulf coast (Galloway, 2008). The basement rocks beneath the Gulf Coastal Plain sediments form the transitional continental crust that has experienced Early Mesozoic extension and post-Jurassic sediment accumulation (Sawyer et al., 1991; Galloway, 2008). Marine sediments in the Gulf Coastal Plain of Mississippi, Louisiana and Texas are significantly thicker than that in the Atlantic Coastal Plain.

The unconsolidated or only partly consolidated sediments in the Coastal Plain overlying a pre-Cambrian to Triassic basement of much older consolidated rocks may have profound effects on earthquake ground motions. Chapman et al. (1990) found high-frequency attenuation effects ($> 3 - 10$ Hz) and low-frequency amplification effects of the Atlantic Coastal Plain sediments on ground motion from the 1886 Charleston, South Carolina, earthquake using linear regression analysis and ground motion modeling. Pratt et al. (2017) found strong amplification in the 0.7 to 4 Hz frequency range for sites on sediments in Washington DC region using seismic data from temporary seismometer array.

Modeling the site response effects of the marine sediments is a significant step in devel-

oping ground motion prediction models for the Coastal Plain region. Recently, Chapman & Conn (2016) reported geographic variation of the near surface attenuation factor κ in the Gulf Coastal Plain using Lg waves. The Lg phase is the largest amplitude part of the high-frequency seismogram and is comprised of shear waves that are guided by the crustal structure. κ is a parameter that defines the degree of frequency-dependent attenuation (Anderson & Hough, 1984). κ is equal to wave traveltime divided by the quality factor Q and has the physical dimension of time. Large values of κ imply strong attenuation at high frequencies. They observed a strong positive correlation between the κ values and the sediment thickness in the Coastal Plain. They showed that high-frequency ground motion predictions in the Gulf Coastal Plain can be improved by incorporating a thickness-dependent Lg κ model in the stochastic ground motion simulations. Nonetheless, an extensive examination of the site response effects of the sediments over a broad frequency range is still lacking for the whole Atlantic and Gulf Coastal Plain region.

The most common empirical method to estimate the site response factors is the spectral ratio technique (Borcherdt, 1970), where the spectrum at a target station is divided by the spectrum at the reference site. The resulting spectral ratio represents a good estimate of relative amplification or/and attenuation factors of the target station to the reference site, if the source and path effects at the target and reference sites are effectively canceled out.

In this dissertation, we quantify the relative difference between site response in the Coastal Plain and the region outside the Coastal Plain using coda and Lg spectral ratios. The reference spectrum is defined as the average of all qualified coda (Lg) spectra at stations outside the Coastal Plain region. The latter part of this dissertation provides a detailed description on modeling the coda and Lg spectral ratios in terms of frequency and sediment thickness and incorporating the spectral ratio functions into the ground motion prediction models for the Coastal Plain regions.

1.3 Summary of Dissertation Chapters

In **Chapter 2**, we report finite-frequency imaging of the global 410-km and 660-km discontinuities using boundary sensitivity kernels for traveltimes measurements made on SS precursors. The application of finite-frequency sensitivity kernels overcomes the resolution limits in previous studies associated with large Fresnel zones, low signal-to-noise ratios of SS precursors as well as interference with other seismic phases. In this chapter, we calculate the finite-frequency sensitivities of SS waves and their precursors based on a single-scattering (Born) approximation in the framework of travelling-wave mode summation. The global discontinuity surface is parameterized using a set of triangular grid points with a lateral spacing of about 4° , and we solve the linear finite-frequency inverse problem (2D tomography) based on the singular value decomposition (SVD). The new global models start to show a number of features that were absent (or weak) in ray-theoretical back-projection models at spherical harmonic degrees greater than 6. The thickness of the mantle transition zone correlates well with wave speed perturbations at a global scale, suggesting dominantly thermal origins for the lateral variations in the mantle transition zone. However, an anti-correlation between the topography of the 410-km discontinuity and wavespeed variations is not observed at a global scale. Overall, the mantle transition zone is about 2-3 km thicker beneath the continents than in oceanic regions. The new models of the 410-km and 660-km discontinuities show better agreement with the finite-frequency study by Lawrence & Shearer (2008) than other global models obtained using SS precursors. However, significant discrepancies between the two models exist in the Pacific Ocean and major subduction zones at spherical harmonic degrees greater than 6. This indicates the importance of accounting for wave interactions in the calculations of sensitivity kernels as well as the use of finite-frequency sensitivities in data quality control.

Slab pull is generally considered as the dominant force that drives the global movement of tectonic plates. This convection mode is well constrained in the upper mantle but its convection pattern in the mid mantle is less understood. In **Chapter 3**, we show that

the finite-frequency 410 and 660 topographic models obtained in this dissertation reveal a strong positive correlation between the two discontinuities under major subduction zones, where both discontinuities occur at depths greater than the global average. This structure correlates well with seismic wavespeed anomalies, suggesting return flows from the lower mantle occur predominantly in the vicinity of stagnant slabs. This mode of mass exchange between the upper and lower mantle is largely decoupled from slab pull that drives plate tectonics. In oceanic regions, the two discontinuities show a weak anti-correlation, indicating the existence of a secondary global far-field return flow. The characteristic anti-correlation between the 410- and 660-km discontinuities for mantle plumes is observed at some oceanic hotspots but the anomalies are very sensitive to mantle wave speed corrections. The most robust plume-like feature in the discontinuity models is located south of the Hess Rise, where geoid anomalies at intermediate wavelength also suggest a possible mid-mantle origin of the anomaly.

In **Chapter 4**, the difference in response between sites in the Atlantic and Gulf Coastal Plain and sites outside the Coastal Plain was investigated using Fourier spectral ratios from regional earthquakes happening in 2010-2018. The average coda and Lg spectra for sites outside the Coastal Plain were used as the reference. Ground motions at the Coastal Plain sites show low-frequency amplification and high-frequency attenuation effects compared to the average condition outside the Coastal Plain. The differential kappa values estimated using high-frequency coda spectral ratios show strong positive correlations with the sediment thickness in the Coastal Plain and agree well with previous kappa values estimated from Lg-waves. We observed consistent patterns in the amplitudes of Lg spectral ratio as a function of sediment thickness, which were then modeled as bi-linear functions within frequency range 0.1-2.86 Hz. The kappa values determine the amplitudes of the spectral ratios at frequencies above 3 Hz when the thickness of the sediments exceeds ~ 0.5 km. The peak frequency and maximum relative amplification at frequencies less than ~ 1.0 Hz depend on sediment thickness. Examination of residuals between observed and predicted ground motions proves the effectiveness of the ratio functions in improving the ground motion prediction models for

the Coastal Plain region.

Bibliography

- Anderson, D. L., 1967. Phase changes in the upper mantle, *Science*, **157**, 1165–1173.
- Anderson, J. & Hough, S., 1984. A model for the shape of the Fourier amplitude spectrum of acceleration at high frequencies, *Bull. Seismol. Soc. Am.*, **74**, 1969–1993.
- Borcherdt, R. D., 1970. Effects of local geology on ground motion near San Francisco Bay, *Bull. Seismol. Soc. Am.*, **60**, 29–61.
- Chambers, K., Woodhouse, J., & Deuss, A., 2005. Topography of the 410-km discontinuity from PP and SS precursors, *Earth and Planetary Science Letters*, **235**, 610–622.
- Chapman, M. & Conn, A., 2016. A model for Lg propagation in the Gulf Coastal Plain of the southern United States, *Bull. Seismol. Soc. Am.*, **106**, 349–363.
- Chapman, M. C., Bollinger, G. A., Sibol, M. S., & Stephenson, D. E., 1990. The influence of the Coastal Plain sedimentary wedge on strong ground motions from the 1886 Charleston, South Carolina, earthquake, *Earthquake Spectra*, **6**, 617–640.
- Christensen, U., 1996. The influence of trench migration on slab penetration into the lower mantle, *Earth Planet. Sci. Lett.*, **140**, 27–39.
- Dahlen, F., 2005. Finite-frequency sensitivity kernels for boundary topography perturbations, *Geophys. J. Int.*, **162**, 525–540.
- Deuss, A., 2009. Global observations of mantle discontinuities using SS and PP precursors, *Surv. Geophys.*, **30**, 301–326.

- Estabrook, C. H. & Kind, R., 1996. The nature of the 660-kilometer upper-mantle seismic discontinuity from precursors to the PP phase, *Science*, **264**, 1179–1182.
- Flanagan, M. & Shearer, P., 1998. Global mapping of topography on transition zone discontinuities by stacking of SS precursors, *J. Geophys. Res.*, **103**, 2673–2692.
- Galloway, W. E., 2008. Depositional evolution of the gulf of mexico sedimentary basin, in *Sedimentary Basins of the United States and Canada*, pp. 505–548, ed. Miall, A., Sedimentary Basins of the World, Elsevier, Amsterdam, The Netherlands.
- Gao, S. S. & Liu, K. H., 2014. Mantle transition zone discontinuities beneath the contiguous United States, *J. Geophys. Res. Solid Earth*, **119**, 6452–6468.
- Gu, Y., Dziewonski, A., & Ekstrom, G., 2003. Simultaneous inversion for mantle shear velocity and topography of transition zone discontinuities, *Geophys. J. Int.*, **154**, 559–583.
- Gu, Y. J. & Dziewonski, A. M., 2002. Global variability of transition zone thickness, *Journal of Geophysical Research*, **107**, doi:10.1029/2001JB000489.
- Helfrich, G., 2000. Topography of the transition zone seismic discontinuities, *Reviews of Geophysics*, **38(1)**, 141–158.
- Houser, C., Masters, G., Flanagan, M., & Shearer, P., 2008. Determination and analysis of long-wavelength transition zone structure using SS precursors, *Geophys. J. Int.*, **174**, 178–194.
- Ita, J. & Stixrude, L., 1992. Petrology, elasticity, and composition of the mantle transition zone, *Journal of Geophys. Res.*, **97**, 6849–6866.
- Lawrence, J. & Shearer, P., 2006. A global study of transition zone thickness using receiver functions, *J. Geophys. Res.*, **111**, doi:10.1029/2005JB003973.
- Lawrence, J. F. & Shearer, P. M., 2008. Imaging mantle transition zone thickness with SdS-SS finite-frequency sensitivity kernels, *Geophysical Journal International*, **174**, 143–158.

- Lessing, S., Thomas, C., Rost, S., Cobden, L., & Dobson, D. P., 2014. Mantle transition zone structure beneath india and western china from migration of PP and SS precursors, *Geophys. J. Int.*, **197**, 396–413.
- Li, X. & Yuan, X., 2003. Receiver functions in northeast China - implications for slab penetration into the lower mantle in northwest pacific subduction zone, *Earth and Planetary Science Letters*, **216**, 679–691.
- Neele, F. & de Regt, H., 1999. Imaging upper-mantle discontinuity topography using underside-reflection data, *Geophys. J. Int.*, **137**, 91–106.
- Niu, F. L., Inoue, H., Suetsugu, D., & Kanjo, K., 2000. Seismic evidence for a thinner mantle transition zone beneath the South Pacific Superswell, *Geophys. Res. Lett.*, **27(13)**, 1981–1984.
- Pratt, T. L., Horton, J. W., Munoz, J., Hough, S. E., Chapman, M. C., & Olgun, C. G., 2017. Amplification of earthquake ground motions in Washington, DC, and implications for hazard assessments in central and eastern North America, *Geophys. Res. Lett.*, **44**, 12150–12160.
- Ringwood, A. E., 1975. *Composition and petrology of the Earth's mantle*, McGraw-Hill, New York.
- Salvador, A., 1991. The gulf of mexico basin, chapter 1 introduction, in *The Gulf of Mexico Basin*, vol. J, pp. 1–12, ed. Salvador, A., The Geology of North America, Geological Society of America, Boulder, Colorado.
- Sawyer, D. S., Buffler, R. T., & Pilger Jr., A., 1991. The crust under the Gulf of Mexico basin, in *The Gulf of Mexico Basin*, vol. J, pp. 53–72, ed. Salvador, A., The Geology of North America, Geological Society of America, Boulder, Colorado, 1-12.
- Shearer, P. M., 1991. Constraints on upper mantle discontinuities from observations of

- long-period reflected and converted phases, *Journal of Geophysical Research*, **96**, 18,147–18,182.
- Shearer, P. M., 1993. Global mapping of upper mantle reflectors from long-period SS precursors, *Geophys. J. Int.*, **115**, 878–904.
- Shearer, P. M. & Masters, G., 1992. Global mapping of topography on the 660-km discontinuity, *Nature*, **355**, 791–796.
- Shearer, P. M., Flanagan, M. P., & Hedlin, M. A., 1999. Experiments in migration processing of ss precursor data to image upper mantle discontinuity structure, *J. Geophys. Res.*, **104**, 7229–7242.
- Shen, Y., Solomon, S. C., Bjarnason, I. T., & Purdy, G. M., 1996. Hot mantle transition zone beneath Iceland and the adjacent Mid-Atlantic Ridge inferred from P-to-S conversions and the 410- and 660-km discontinuities, *Geophys. Res. Lett.*, **23**, 3527–3530.
- Thomas, W. A., Chowns, T. M., Daniels, D. L., Neathery, T. L., & Glover III, L., 1989. The subsurface Appalachians beneath the Atlantic and Gulf Coastal Plains, in *he Appalachian-Ouachita Orogen in the United States*, vol. F-2, pp. 445–458, eds Hatcher, R. D., Thomas, W. A., & Viele, G. W., The Geology of North America, Geological Society of America, Boulder, Colorado.
- Wang, X., Li, J., & Chen, Q.-F., 2017. Topography of the 410km and 660km discontinuities beneath the Japan Sea and adjacent regions by analysis of multiple-ScS waves, *J. Geophys. Res. Solid Earth*, **122**, 1264–1283.
- Xu, F., Vidale, J. E., Earle, P. S., & Benz, H. M., 1998. Mantle discontinuities under southern africa from precursors to p'p'diff, *Geophys. Res. Lett.*, **25**, 571–574.
- Ye, Y., Gu, C., Shim, S.-H., Meng, Y., & Prakapenka, V., 2014. The postspinel boundary in pyrolitic compositions determined in the laser-heated diamond anvil cell, *Geophys. Res. Lett.*, **41**, 3833–3841.

Zhou, Y., 2018. Anomalous mantle transition zone beneath the Yellowstone hotspot track, *Nature Geoscience*, **11**, 449–453.

Chapter 2

Finite-Frequency Imaging of the Global 410-km and 660-km Discontinuities Using SS Precursors

(An edited version of this chapter has been submitted to Geophysics Journal International.)

2.1 Introduction

The 410-km and 660-km discontinuities have been progressively mapped out in global seismic imaging since the 1990s (Revenaugh & Jordan, 1991; Shearer, 1991; Flanagan & Shearer, 1998; Gu et al., 1998, 2003; Lawrence & Shearer, 2006; Deuss, 2009). High temperature and pressure mineral physics experiments suggest that the two discontinuities are associated with pressure-induced phase transitions of olivine to wadsleyite at about 410 km and ringwoodite to perovskite + magnesiowustite at about 660 km, respectively (Anderson, 1967; Ita & Stixrude, 1992). In regional and local seismic imaging, P-to-S converted waves have been widely used to map the two discontinuities at relatively high resolutions, especially in regions

where seismic data have been recorded by small aperture station arrays (Shen et al., 1998; Li & Yuan, 2003; Lee et al., 2014; Gao & Liu, 2014; Kosarev et al., 2017; Kaviani et al., 2018; Zhou, 2018). In general, global models obtained using P-to-S converted waves have lower resolution in oceanic areas because of limited data coverage (Chevrot et al., 1999; Lawrence & Shearer, 2006). In global studies, the underside reflections of SS waves (SS precursors) have been used to map the global depth perturbations of the 410 and the 660. SS precursors are most sensitive to discontinuity structures near the SS wave bounce points and therefore they provide better global coverage than P-to-S converted waves, especially in oceanic regions where very few seismic stations are deployed.

SS precursors are secondary waves reflected at the underside of the 410-km and the 660-km discontinuities, their amplitudes are relatively small due the low impedance ratio across the two seismic discontinuities (Fig. 2.1). Previous SS precursor studies in imaging the global mantle transition zone structures commonly chose to stack the SS precursors in large circular bins to improve the signal-to-noise ratios and obtain depth perturbations on the discontinuities based on the conventional JWKB ray theory (Shearer, 1991; Gu et al., 1998, 2003; Schmerr & Garnero, 2006; Houser et al., 2008; Deuss, 2009). Ray theory is a high-frequency approximation which assumes that seismic waves travel through the earth along infinitesimally narrow paths. In reality, however, seismic waves have finite frequency and SS waves are sensitive to a large area on the boundary centered at the bounce point. It has been suggested by several studies that topographic structures with sizes smaller than the first Fresnel zone may not be resolved properly using the traditional ray theory (Neele et al., 1997). The resolution of the ray-theoretical models is limited by the large Fresnel zone of SS waves and their precursors (~ 1000 km at 20 second period) and only large-scale features are reliable. A better theory, which can account for scattering, wavefront healing and other finite frequency effects of seismic waves is needed to improve the resolution of smaller scale topographic anomalies. Neele & de Regt (1999) proposed a method to approximate the finite-frequency sensitivities of SS and PP precursors over the first Fresnel zone. They applied the method to a large synthetic data set and showed that depth variations with a lateral scale

smaller than the first Fresnel zone but larger than the dominant wavelength can be well resolved. The first global topographic maps of the 410 and the 660 based on finite-frequency theory were published by Lawrence & Shearer (2008) using traveltime sensitivity kernels of SS precursors calculated based on ray tracing (Dahlen, 2005). The power spectra of the seismic phases in the reference model were approximated by the observed power spectra, and the sensitivity kernels were stacked in circular bins of different sizes in the inversions.

In this study, we construct a global data set of finite-frequency traveltime measurements of SS waves and SS precursors by measuring traveltime differences between the observed and synthetic seismograms in the frequency domain. One major concern in imaging the 410 and the 660 using SS precursors is phase interactions (e.g., precursors of ScSScS wave and the postcursors of S_{diff} interfere with SS precursors). To reduce possible uncertainties in SS precursor data, earlier studies often chose to limit the range of epicentral distance to avoid possible phase interference, which limits the spatial resolution of available data (Schmerr & Garnero, 2006; Deuss, 2009; Lessing et al., 2014). To overcome the above limitations, we calculate sensitivity kernels in the framework of traveling-wave mode coupling, which fully accounts for interference of seismic waves arriving in the measurement windows, the effects of source radiation and seismogram windowing/tapering. This study is the first study to image the 410-km and 660-km discontinuities using single-trace SS (and precursor) traveltime measurements and individual finite-frequency sensitivity kernels.

The sensitivity kernels can be used to identify measurements that are heavily influenced by shallower multiples, and those measurements can be excluded when they are not most sensitive to the depth perturbations of the 410 and the 660. We will focus on finite-frequency effects in the imaging of the 410 and the 660 using single trace traveltime measurements of SS precursors by investigating models obtained using 2-D diffractive tomography and those obtained from ray-theoretical back-projections using the the same dataset. We compare our finite-frequency discontinuity model with previous studies and show that the new model agrees better with the finite-frequency model by Lawrence & Shearer (2008) than other global models imaged using SS precursors based on ray theory. We will discuss major discrepancies

between the two finite-frequency models and the significance of data processing in finite-frequency imaging.

2.2 Finite-Frequency Traveltime Measurements

We built a global dataset of the finite-frequency traveltime measurements using seismograms recorded at 150 stations in the Global Seismological Network (GSN) for earthquakes occurred between January 2003 and September 2014 (Fig. 2.2). The earthquakes have moment magnitudes ranging from 6.0 to 8.5 and focus depths less than 100 km. All available seismograms with epicentral distances between 90 and 160 degrees are downloaded from the Data Management Center at the Incorporated Research Institutions for Seismology (IRIS). Initial data processing includes removing instrument responses, rotating the horizontal components to obtain the transverse component seismograms and applying bandpass filter with corner frequencies at 0.01 and 0.1 Hz. We visually inspected seismograms and carefully selected the ones with high signal-to-noise ratios and clear SS waves and precursors. We corrected abnormal polarities of the transverse component seismograms at several stations and we discarded seismograms with highly deformed SS waveforms. The final dataset contains a total number of about 6400 seismograms from 1117 earthquakes.

Synthetic seismograms are calculated in a 1-D reference earth model IASP91 (Kennett & Engdahl, 1991) based on travelling-wave mode summation (Liu & Zhou, 2016). The global centroid-moment-tensor (CMT) solution and the USGS Preliminary Determination of Epicenters (PDE) source locations and origin times are used in the calculations of the 1-D synthetic seismograms. The same band-pass filter is applied to the synthetic seismograms. We manually pick measurement windows centered near the maximum amplitudes of the phases (SS or SS precursors) and the length of the measurement time windows ranges from 70 to 120 seconds. Finite-frequency traveltime measurements are made with a cosine taper of the same length to limit spectra leakage (Fig. 2.3). The spectrum of the cosine taper

shows a relatively broad central peak and very weak side lobes (Deng & Zhou, 2015). The differences in traveltimes between the synthetic and observed signals are calculated in the frequency domain (Xue et al., 2015).

Figure 2.3 shows example observed and synthetic seismograms from the dataset. The observed seismogram is recorded at station EFI on East Falkland Island from a moment magnitude 6.9 earthquake in Indonesia occurred in 2003. The epicentral distance of this seismogram is 130° . Time windows used for measuring the traveltime residuals of SS waves and SS precursors are shaded on the seismograms. It is important to point out that finite-frequency traveltime measurements depend on the length and position of the measurement windows as well as the time-domain taper applied in making the measurements. The effects of windowing and tapering are accounted for in the calculation of the finite-frequency sensitivity of each measurement. In this chapter, we will focus on inversions using data obtained at a measurement period of 20 seconds.

2.3 Finite-Frequency Sensitivities to Boundary Perturbations

Depth perturbations on seismic discontinuities will cause arrival time anomalies of SS waves and SS precursors. The differences in arrival times between the observed and synthetic seismic phases can be used to image lateral variations of the seismic discontinuities with respect to a 1-D reference earth model. Theoretically, the traveltime difference between an observed and a synthetic SdS wave, δt_{SdS} , can be written as a two-dimensional integration over the global surface of the corresponding discontinuity Σ (the 410-km or the 660-km discontinuity),

$$\delta t_{SdS}(\omega) = \iint_{\Sigma} K_{\Sigma}^{SdS}(\mathbf{x}, \omega) \delta d(\mathbf{x}) d\Sigma, \quad (2.1)$$

where $K_{\Sigma}^{SdS}(\mathbf{x}, \omega)$ is the sensitivity of an individual SS precursor (SdS) traveltime measurement at an angular frequency ω to depth perturbations $\delta d(\mathbf{x})$ of the discontinuity Σ . In

ray theory, seismic waves propagate as rays along infinitesimally narrow paths following the *Snell's* law. Therefore, the arrival time perturbation of an SS precursor depends only on the discontinuity depth perturbation at the bounce point. Eq. (2.1) then becomes a simple product of the 1-D time-depth derivative and the depth perturbation at the bounce point (Gu & Dziewonski, 2002). In finite frequency theory, seismic waves experience scattering, wave-front healing and other diffractive effects during wave propagation. Therefore, the traveltimes of SS precursors are not only sensitive to the structure at the bounce point but also to structures within a broad area centered at the bounce point on the discontinuity. In this chapter, we calculate the finite-frequency sensitivity $K_{\Sigma}^{SdS}(\mathbf{x}, \omega)$ based on single-scattering (Born) approximation in the frame work of traveling wave mode coupling,

$$K_{\Sigma}^{SdS}(\mathbf{x}, \omega) = \text{Im} \left[\omega^{-1} \frac{[\mathcal{K}_{\Sigma}(\mathbf{x}, \omega) \otimes h(\omega)] [s(\omega) \otimes h(\omega)]^*}{[s(\omega) \otimes h(\omega)] [s(\omega) \otimes h(\omega)]^*} \right], \quad (2.2)$$

where $s(\omega)$ is the displacement spectrum in the reference earth model and $h(\omega)$ is the spectrum of the cosine taper used in making the measurement. The operator \otimes denotes convolution in frequency domain and the asterisk denotes the complex conjugate. The complex waveform kernel for boundary depth perturbations $\mathcal{K}_{\Sigma}(\mathbf{x}, \omega)$ is

$$\mathcal{K}_{\Sigma}(\mathbf{x}, \omega) = \sum_{\sigma'} \sum_{\sigma''} S' \left[\frac{e^{-i(k'\Delta' + \pi/4)}}{\sqrt{8\pi k' |\sin \Delta'|}} \right] \times \left[\frac{e^{-i(k''\Delta'' + \pi/4)}}{\sqrt{8\pi k'' |\sin \Delta''|}} \right] R'' \times [\Omega^{(1)} + \Omega^{(2)}]_{-}^{+}. \quad (2.3)$$

In the above equation, the single prime and double primes represent quantities calculated along the great circle path from the source to the scatter (mode σ') and the scatter to the receiver (mode σ''), respectively. Δ is the great circle distance between the source and receiver and k is the wave number. The source and receiver terms are S' and R' respectively and $\Omega^{(1)}$ and $\Omega^{(2)}$ are boundary scattering coefficients. Detailed expressions of the source and receiver terms as well as scattering coefficients can be found in Zhou et al. (2005).

For SS waves, traveltime delays caused by depth perturbations on the seismic discontinuity Σ can be expressed as

$$\delta t_{SS}(\omega) = \iint_{\Sigma} K_{\Sigma}^{SS}(\mathbf{x}, \omega) \delta d(\mathbf{x}) d\Sigma, \quad (2.4)$$

where $K_{\Sigma}^{SS}(\mathbf{x}, \omega)$ is the SS wave sensitivity to the depth perturbations on the boundary Σ . Equations (2.1) and (2.4) shows a linear relation between the traveltime measurements and boundary depth perturbations, which leads to a simple expression for SdS-SS differential measurements

$$\delta t_{SdS}(\omega) - \delta t_{SS}(\omega) = \iint_{\Sigma} [K_{\Sigma}^{SdS}(\mathbf{x}, \omega) - K_{\Sigma}^{SS}(\mathbf{x}, \omega)] \delta d(\mathbf{x}) d\Sigma. \quad (2.5)$$

We calculate finite-frequency sensitivity kernels for SS waves and their precursors (K_{Σ}^{SS} and K_{Σ}^{SdS}) in a 1-D reference earth model IASP91, fully accounting for phase interactions, source radiation patterns, time-domain windowing and tapering applied in making frequency-dependent traveltime measurements (Zhou et al., 2005; Zhou, 2009; Deng & Zhou, 2015).

Fig. 2.4 shows examples of 2-D traveltime sensitivity of S410S and S660S waves to depth perturbations of the 410-km and 660-km discontinuities. The epicentral distance is 133° and the kernels are calculated for traveltime measurements at a period of 20 seconds. The sensitivity kernels show the typical X shape with maximum positive values in the center of the X and alternating side bands in the second and third Fresnel zones. The size of the first Fresnel zone (with positive sensitivity) is about $15^{\circ} \times 15^{\circ}$, indicating that ray theory, which assumes traveltime sensitive only to structure at the bounce point, is a rather crude approximation in this case.

In general, the boundary sensitivity of SS waves is about an order of magnitude smaller than the sensitivity of SdS waves (Fig. 2.5). Therefore, the sensitivity kernels of the $SdS-SS$ differential measurements show only minor differences from the SdS sensitivity kernels. We point out that the boundary sensitivity kernels often have structures more complex than those plotted in Figs 2.4 and 2.5 due to interfering seismic phases arriving within the measurement windows. For those measurements, the typical X -shape structure due to the minimum-maximum nature of the precursors will be deformed and the amplitudes of the sensitivity may become extreme. The complexity of the finite-frequency sensitivity kernels can be used to identify measurements associated with wave interference due to multiples of a shallower interface or other seismic phases. We exclude those measurements as linear perturbation

theory may not apply when the reference phase is much weaker than scattered waves.

2.4 The Inverse Problem

We parametrize the surface of the Earth using a set of spherical triangular grid points. The spherical triangles are 16-fold, with 2562 vertexes and a lateral spacing of about 4.3° (Zhou et al., 2005). With this model parametrization, the matrix form of the inverse problem in equation (2.1) can be expressed as

$$\mathbf{Ax} = \mathbf{b}, \quad (2.6)$$

where \mathbf{x} is the model vector of unknown depth perturbations on the discontinuity and \mathbf{b} is the data vector of *SdS-SS* traveltime residuals. \mathbf{A} is the sensitivity matrix with components a_{ij} representing the sensitivity of the *i*th observed data to the depth perturbation at the *j*th model grid.

Due to uneven data coverage and the presence of noise, the inverse problem is ill-posed and regularization is required to find an optimal solution. We apply Tikhonov regularization to eq. (2.6) and solve a regularized problem

$$(\mathbf{A}^T \mathbf{A} + \alpha^2 \mathbf{I}) \mathbf{x} = \mathbf{A}^T \mathbf{b} \quad (2.7)$$

where α is the Tikhonov regularization parameter and \mathbf{I} is an identity matrix.

To solve the above inverse problem, matrix \mathbf{A} is decomposed using the singular value decomposition (SVD),

$$\mathbf{A} = \mathbf{U} \mathbf{\Sigma} \mathbf{V}^T, \quad (2.8)$$

where \mathbf{u}_i in \mathbf{U} and \mathbf{v}_i in \mathbf{V} are the left and right singular vectors respectively, and the matrix $\mathbf{\Sigma}$ is a diagonal matrix containing the singular values σ_i .

The Tikhonov solution to the least-square problem is then written as

$$\mathbf{x} = \sum_i \frac{\sigma_i^2}{\sigma_i^2 + \alpha_i^2} \frac{\mathbf{u}_i^T \mathbf{b}}{\sigma_i} \mathbf{v}_i. \quad (2.9)$$

The choice of the regularization parameter α is made by studying the tradeoffs between the model norm and data misfit. Typically, the optimal value of the regularizing parameter is chosen near the lower left corner of the trade-off curve where further reduction in model norm starts to introduce a large increase in data misfit.

2.5 Finite-Frequency Effects in Discontinuity Imaging

The 410-km and 660-km discontinuity models obtained from finite-frequency inversions are plotted in Fig. 2.6. We have removed the mean perturbations of the two discontinuities and the reference depths of the 410-km and the 660-km discontinuities in Fig. 2.6 are 411.6 and 660.4 km, respectively. Positive perturbations (in blue) indicate discontinuity depths greater than the reference depths, and negative perturbations (in red) indicate shallower discontinuity. Overall, the 660-km discontinuity shows larger depth variations than the 410-km discontinuity, which is consistent with traveltimes observations. The $S660S$ and $S410S$ measurements have similar standard deviations (6.14 s and 6.10 s respectively) while the same amount of depth perturbations on the two discontinuities would predict larger traveltimes anomalies in the $S410S$ waves than the $S660S$ waves. Stronger topographic variations of the 660-km discontinuity have also been observed in several previous studies (Flanagan & Shearer, 1998; Gu et al., 2003; Lawrence & Shearer, 2008).

The 660-km discontinuity structure shows a striking contrast between oceans and continents. The discontinuity is overall shallower in oceanic regions and deeper in a broad region across the Eurasia and along the west coast of the North America. Regional studies using receiver functions and PP/SS precursors have reported similar depressed 660 topography in the Sea of Okhotsk, Eastern Russia, Northeastern China as well as the North American Farallon subduction zone (Schmerr & Thomas, 2011; Zheng et al., 2015; Heit et al., 2010; Gao & Liu, 2014; Wang & Pavlis, 2016; Zhou, 2018). The 660-km discontinuity beneath the Mediterranean Sea and the Middle East shows several small-scale depressions which were

also imaged by Kaviani et al. (2018).

The ocean-continent contrast is much weaker on the 410-km discontinuity. There is an apparent age-dependent signature in the Pacific Ocean, where the 410 becomes deeper towards the middle ocean spreading centers. The 410-km discontinuity is depressed in the western North America and eastern Asia extending from Tibet through central and northern China to the western Sea of Okhotsk, in general agreement with regional studies (Heit et al., 2010; Gao & Liu, 2014; Wang & Pavlis, 2016).

In Fig. 2.6, we compare the finite-frequency models of the 410- and 660-km discontinuities with depth perturbations obtained from back-projection using the same SdS - SS traveltime measurements. In ray-theoretical data back projection, we do not invert the traveltime measurements but estimate discontinuity depth perturbations from traveltime residuals using 1-D time-depth derivatives. The depth perturbations are averaged in a moving circular cap with a constant radius and plotted in Fig. 2.7. When the cap size is small (4°), the resulting back-projection maps become more noisy due to rather small number of data points available in the averaging cap, especially in South America and Western Australia where data sampling is sparse. When the radius of the cap is 6° , the structure becomes more smooth. Overall, the long-wavelength structures of the 410-km and 660-km discontinuity maps obtained using ray-theoretical data back projection agree well with finite-frequency models.

In Fig. 2.7, the finite-frequency sensitivity density and the back-projection ray density show similar coverage and smoothness when the size of the circular cap used in ray-theoretical back projection is 6° . The resulting models show large discrepancies in their dominant structure length scales (Fig. 2.6). The finite-frequency models show much stronger small-scale structures that are absent in the ray-theoretical back-projection models. This is expected as finite-frequency sensitivity kernels account for wave diffractive effects. For example, the anomalies along the western North America are much narrower and mostly confined in the continent regions while anomalies are much broader and diffused in the ray-theoretical back-projection models, regardless of the cap size.

We calculate the correlation coefficients between the finite-frequency models and the back-projection models as a function of spherical harmonic degree up to $l = 20$ in Fig. 2.8. Models obtained using finite-frequency tomography and ray-theoretical back projection are positively correlated at all spherical harmonic degrees, regardless of the averaging cap size. The two 410-km discontinuity models are well correlated with a correlation coefficient of 0.96 in their large-scale structures ($l < 5$), and the correlation coefficient decreases to ~ 0.8 at intermediate length scales ($6 \leq l \leq 14$). For smaller scale structure with harmonic degree $l \geq 15$ (wavelength $< \sim 2500$ km), the correlation coefficient decreases to ~ 0.5 . The correlation between the two 660-km discontinuity models show very similar variations as a function of spherical harmonic degree, except that small-scale structures show better correlations with the finite-frequency model when a 4° cap is used in the back-projection model.

2.6 Crust and Mantle Corrections

Lateral variations in crustal structure and seismic wavespeed in the upper mantle will introduce traveltime differences between observed and synthetic seismograms calculated in the 1-D reference earth model, IASP91 (Kennett & Engdahl, 1991). These traveltime anomalies can be subtracted from SS and SdS measurements by applying corrections using published 3-D crust and mantle velocity models. In this section, we investigate the impact of crustal and mantle corrections on the imaging of the 410-km and 660-km discontinuities in finite-frequency tomography. We calculate expected traveltime anomalies caused by the 3-D structure of the crust using a global crustal model CRUST1.0 (Laske et al., 2013). This is a $1^\circ \times 1^\circ$ model which parametrized wavespeeds and density in the crust and uppermost mantle as 8 layers in every $1^\circ \times 1^\circ$ cell. Crustal corrections are positive beneath continents and negative in oceanic areas. The maximum correction is about 4.6 seconds for SS waves with bounce points in the Tibetan Plateau where the crust is about 60 km thicker than in the reference model.

Mantle wavespeed corrections are often applied to account for traveltime anomalies caused by 3-D wavespeed structure in the mantle using global models from independent studies. This method has been suggested to be more straightforward and accurate in SS precursor imaging than joint inversions to resolve discontinuity depth variations and wavespeed perturbations simultaneously (Houser et al., 2008). This is because datasets required to image discontinuity depths are different from those that constrain seismic wavespeed in the bulk mantle, including surface waves, body waves and free oscillations (Panning & Romanowicz, 2006; Zhou et al., 2006; Ritsema et al., 2011; Schaeffer & Levedev, 2013; Moulik & Ekstrom, 2014). We calculate traveltime corrections using two different global 3-D mantle models, S40RTS (Ritsema et al., 2011) and S362ANI+M (Moulik & Ekstrom, 2014). In model S40RTS, wavespeed perturbations are with respect to a 1-D reference earth model PREM (Dziewonski & Anderson, 1981) while the 3-D model S362ANI+M is anisotropic and wavespeed perturbations are deviations from a 1-D reference model STW105 (Kustowski et al., 2008). We calculate wavespeed perturbations in S40RTS and S362ANI+M with respect to the same 1-D reference model IASP91 and then integrate traveltime anomalies along the ray paths of SS waves and SS precursors. In general, wave speed corrections for SdS - SS measurements are smaller than that for individual SS and SdS waves, which is not unexpected as wave speed structure in the lower mantle introduces similar shifts in both the SS and SdS travel times.

The absolute traveltime corrections are significant with maximum values up to 15-20 seconds for some paths, but the corrections do not change the general geographic pattern of the SdS - SS traveltime residues when plotted at the SS-wave bounce points (Fig. 2.9). However, the corrections do affect the amplitudes and the extract locations of the discontinuity anomalies in the final models (Fig. 2.10). For example, the age-dependent depth perturbation of the 410-km discontinuity in the Pacific Ocean in Fig. 2.6 becomes much weaker after wavespeed correlations are applied. In addition to oceanic regions, crustal and mantle corrections also have an impact on discontinuity structures beneath stable cratons (e.g., the Canadian shield and the Baltic Shield) where the magnitude of SdS - SS traveltime measure-

ments is either reduced or changes polarity after crustal and mantle wavespeed corrections (Fig. 2.10). This can be explained by early arrivals of SS waves associated with increased wave speed in the upper mantle in those regions. The strong discontinuity anomalies beneath California also become much weaker after the corrections are applied. It is noteworthy that traveltime corrections made using different global mantle wavespeed models (S40RTS vs. S362ANI) are highly correlated and the final models after wavespeed correlations do not show major differences (Figs 2.10 & 2.11).

The impact of crustal and mantle wavespeed corrections on discontinuity structures at different length scales are plotted in Fig. 2.11. In spherical harmonic analysis, the power spectra is expected to decrease rapidly with angular degree when the peak amplitude of lateral variations remains the same. For example, the spectra power at degree $l = 2$ is about one order of magnitude larger than the spectra power at degree $l = 12$ when depth perturbations at the two harmonics degrees have the same peak amplitude. In general, crustal and mantle corrections emphasize low spherical harmonic degree structures in the discontinuity maps (Figs 2.10 & 2.11). For example, the maximum spectra power of the 660-km discontinuity map is at degree $l = 2$ without data corrections, while the degree-one ($l = 1$) structure becomes the strongest after crustal and mantle wavespeed corrections are applied. This leads to low correlation coefficients between models obtained with and without corrections at degrees 1-2. The correlation is positive but weak at degrees $l = 4 - 5$ and increases with spherical harmonic degree with strongest correlations at degrees $l \geq 8$ (length scale ≤ 2500 km). The thickness of the mantle transition zone is least sensitive to crust and mantle wavespeed corrections and is strongly correlated between models with and without the corrections. Overall, the discontinuity models with and without crust and mantle wavespeed corrections are well correlated regardless of the 3-D wavespeed model used in making the corrections.

2.7 Discontinuity Topography and Wavespeed Structure

The Clapeyron slope, which is the change in pressure over the change in temperature dP/dT , is positive for the olivine to wadsleyite phase transformation (the 410-km discontinuity) and negative for the ringwoodite to perovskite and magnesio-wüstite phase transformation (the 660-km discontinuity). If undulations of the two discontinuities are dominantly caused by lateral thermal variations in the mantle transition zone, we would expect a negative correlation between the 410 topography and variations in seismic wavespeed. For example, in regions where cold slab materials reside in the mantle transition zone, seismic wavespeed increases while the depth of the 410-km discontinuity decreases, resulting a negative correlation. In contrast, the correlation between wavespeed and discontinuity depth would be positive for the 660-km discontinuity due to its opposite Clapeyron. Examining the correlations between perturbations in wavespeed and discontinuity depth will in turn allow us to investigate dominant mechanisms responsible for depth perturbations of the 410-km and 660-km discontinuities.

In Fig. 2.12, we investigate the correlation between discontinuity depth perturbations and seismic wavespeed variations in the mantle transition zone using a global model S40RTS (Ritsema et al., 2011). The discontinuity models are obtained from traveltimes data with corrections made using the same wavespeed model. There is no clear correlation between the topography of the 410-km discontinuity and wavespeed variations at a global scale, except for at spherical harmonics degree $l = 4$ (length scale of ~ 5000 km) where the correlation is positive. The absence of an overall negative correlation between seismic wavespeed and the 410-km discontinuity suggests possible non-thermal origin of heterogeneities. For example, heterogeneities in chemical composition or changes in water content (Schmerr & Garnero, 2007; Gu et al., 2014; Wang et al., 2017).

The topography of the 660-km discontinuity, on the other hand, shows clear positive

correlations with seismic wavespeed in the mantle transition zone up to spherical harmonic degree $l = 11$ (length scale of ~ 3600 km). This positive correlation supports a thermal origin at a global scale. The correlation becomes weaker at higher spherical harmonic degrees and no apparent correlation is observed at $l > 15$ ((lengthscale ~ 1300 km), which is likely due to different lateral resolutions in the wavespeed and topography models. This change from no (weak) correlation at 410 km depth to significant positive correlation at 660 km depth may also be a result of limitations in depth resolution of the global seismic wavespeed model over a scale of 250 km in the mantle transition zone.

The thickness of the mantle transition zone shows strongest correlation with seismic wavespeed. This positive correlation is not surprising as variations in thickness are dominated by the depth perturbations on the 660-km discontinuity, and, there is a positive correlation between the 660-km discontinuity topography and seismic wavespeed. The correlation is stronger in long wavelength variations at spherical harmonic degree $l < 8$. Geographically, the mantle transition zone is thicker beneath the Pacific subduction zones and thinner beneath the oceans, consistent with previous studies (Flanagan & Shearer, 1998; Gu et al., 1998, 2003).

In Fig. 2.13, we plot the average thickness of the mantle transition zone beneath continental areas in Asia, Europe, North America, South America, Africa and Australia. The average thickness of the mantle transition zone beneath continental areas is overall very close to that in the reference model (250 km). Crustal and mantle wavespeed corrections have little impact on the mantle transition zone thickness except for in Asia, Europe and Australia. The corrections result in a 2.3 km thicker mantle transition zone beneath Asia and 1.0 km and 0.9 km thinner mantle transition zone beneath Europe and Australia, respectively. In oceanic regions, the mantle transition zone is about 1.5 km thinner than the reference model and amount of the thinning increases to 4.6 km when CRUST1.0 and model S40RTS are applied to make travelttime corrections. There is no obvious correlation between the thickness of the mantle transition zone and the age of the seafloor.

2.8 Comparison with Previous Global Models

In Fig. 2.14, we compare the 410-km and 660-km discontinuity models in this study with three recent global models imaged based on SS waves and their precursors: Gu et al. (2003), Houser et al. (2008) and Lawrence & Shearer (2008). The four 660-km discontinuity models all show some consistent features. In particular, along subduction zones in the Western Pacific, the 660-km discontinuity is overall deeper than the global average. The mantle transition zone is thicker in the Western Pacific and thinner in the Pacific Ocean. However, large discrepancies exist in the Pacific Ocean. The most extreme disagreement appears to be structures on the 410-km discontinuity maps. For example, the strong depression of the 410-km discontinuity in the Pacific Ocean in Model H08 (Houser et al., 2008) is either absent or much weaker in the other models. The broad uplift of the 660-km discontinuity in the northern Atlantic Ocean in model Model G03 Gu et al. (2003) is weak (absent) in other models. At regional scales, the discrepancies involve reversed polarities in western North America and southeast Asia.

Among all global models, the 410-km and 660-km discontinuity depth perturbations obtained from this study agree best with the finite-frequency model published by Lawrence & Shearer (2008) (Model LS08). In Fig. 2.15, we plot the correlation coefficients between the two models as a function of spherical harmonic degree. The long-wavelength structures in the 660-km discontinuity depth perturbations between the two models are in good agreement, with a positive correlation of ~ 0.76 at spherical harmonic degrees $l \leq 4$. The correlations are only slightly weaker for the 410-km discontinuity with a correlation coefficient of ~ 0.64 . Significant discrepancies can be observed in their smaller scale features. For example, the 410-km discontinuity models filtered at spherical harmonic degrees $l \leq 6$ starts to show major differences in the Pacific ocean (Fig. 2.16), and the correlation coefficient between the two models decreases to ~ 0.1 at $l = 5 - 7$. At spherical harmonic degree $l \leq 12$, the 410-km discontinuity is depressed beneath the Red Sea in our model which is absent in model LS08. A strong negative anomaly in the 410-km discontinuity along the southeast Indian

ridge into the southern Atlantic ocean in model LS08 is absent (much weaker) in our model. Major discrepancies on the 660-km discontinuity include a strong depression beneath the Arabian plate and the Mediterranean sea in model LS08 and a broad uplift in the Northwest Pacific beneath the old Pacific plate, which are absent in our model as well as in the other two models (Fig. 2.17). Overall, the correlations between the new discontinuity model and model LS08 decreases with spherical harmonic degree and there is no apparent correlation between the two models at degree $l > 15$.

The fact that the general features in the Lawrence & Shearer (2008) model agree better with this study than other ray-theoretical models is somewhat expected as both studies are based on tomographic inversions using finite-frequency sensitivity kernels. The sensitivity kernels in Lawrence & Shearer (2008) were calculated based on ray tracing, which is computationally efficient but the sensitivity kernels do not account for phase interactions and windowing/tapering applied in seismograms. However, it is noteworthy that differences between our finite-frequency models and back-projection models obtained using the exact same dataset are less significant than that between the two finite-frequency models. This reflects the importance of accuracy in the calculations of sensitivity kernels as well as the use of finite-frequency sensitivities in data screening and processing. For example, measurements associated with very complex or extreme sensitivity to depth perturbations of the two discontinuities should be excluded.

2.9 Conclusions

In this chapter, we investigate the finite-frequency effects in imaging the global structure of the 410-km and 660-km discontinuities using SS precursors. The finite-frequency SdS - SS traveltimes measurements are made using seismograms recorded at GSN stations for earthquakes occurred between 2003 and 2014. The finite-frequency traveltimes differences between observed and synthetic seismograms are measured in the frequency domain using

a cosine taper. The sensitivity kernels for SS waves and precursors are calculated in the framework of traveling-wave mode coupling, fully accounts for phase interactions within the measurement window.

The finite-frequency models correlated well with ray-theoretical back-projection models in their large scale structure but the finite-frequency models show much stronger small-scale features when the smoothness (coverage) of the back-projection ray density are comparable to that of the finite-frequency sensitivity density. Crustal and mantle wavespeed corrections do not change the general geographic pattern of the *SdS-SS* traveltime measurements and discontinuity models inverted with and without crustal and mantle corrections are overall well correlated, regardless of the global wavespeed models used in making the corrections.

The finite-frequency 660-km discontinuity model is overall positively correlated with wave speed perturbations in the mantle transition zone, indicating a dominant thermal origin for depth perturbations of the 660-km discontinuity. However, a clear correlation between the 410-km discontinuity and seismic wavespeed is not observed, which suggests possible non-thermal heterogeneities in the upper mantle transition zone or limited vertical resolution in seismic wavespeed tomography. We compare global mantle transition zone discontinuity models obtained from SS precursors and show that our finite-frequency model agree best with the model of Lawrence & Shearer (2008), which is also a finite-frequency model but with sensitivities calculated based on ray tracing and additional kernel stacking. However, major discrepancies exist between the two models in both oceanic regions and subduction zones, suggesting the significance of wave interference in the calculations of sensitivity kernels as well as the use of finite-frequency sensitivities in data quality control. For example, measurements associated with very complex or extreme sensitivity to discontinuity depth perturbations can be identified in travelling-wave mode coupling and those measurements can be excluded from tomographic inversions.

Bibliography

- Anderson, D. L., 1967. Phase changes in the upper mantle, *Science*, **157**, 1165–1173.
- Chevrot, S., Vinnik, L., & Montagner, J.-P., 1999. Global-scale analysis of the mantle Pds phases, *J. Geophys. Res.*, **104**, 20,203–20,219.
- Dahlen, F., 2005. Finite-frequency sensitivity kernels for boundary topography perturbations, *Geophys. J. Int.*, **162**, 525–540.
- Deng, K. & Zhou, Y., 2015. Wave diffraction and resolution of mantle transition zone discontinuities in receiver function imaging, *Geophys. J. Int.*, **201**, 2008–2025.
- Deuss, A., 2009. Global observations of mantle discontinuities using SS and PP precursors, *Surv. Geophys.*, **30**, 301–326.
- Dziewonski, A. & Anderson, D., 1981. Preliminary reference Earth model, *Phys. Earth Planet. Inter.*, **25**, 297–356.
- Flanagan, M. & Shearer, P., 1998. Global mapping of topography on transition zone discontinuities by stacking of SS precursors, *J. Geophys. Res.*, **103**, 2673–2692.
- Gao, S. S. & Liu, K. H., 2014. Mantle transition zone discontinuities beneath the contiguous United States, *J. Geophys. Res. Solid Earth*, **119**, 6452–6468.
- Gu, Y., Dziewonski, A., & Agee, C., 1998. Global de-correlation of the topography of transition zone discontinuities, *Earth Planet. Sci. Lett.*, **157**, 57–67.

- Gu, Y., Dziewonski, A., & Ekstrom, G., 2003. Simultaneous inversion for mantle shear velocity and topography of transition zone discontinuities, *Geophys. J. Int.*, **154**, 559–583.
- Gu, Y. J. & Dziewonski, A. M., 2002. Global variability of transition zone thickness, *Journal of Geophysical Research*, **107**, doi:10.1029/2001JB000489.
- Gu, Y. J., Zhang, Y., Sacchi, M. D., Chen, Y., & Contenti, S., 2014. Sharp mantle transition from cratons to Cordillera in southwestern Canada, *J. Geophys. Res. Solid Earth*, **120**, 5051–5069.
- Heit, B., Yuan, X., Bianchi, M., Kind, R., & Gossler, J., 2010. Study of the lithospheric and upper-mantle discontinuities beneath eastern Asia by SS precursors, *Geophys. J. Int.*, **183**, 252–266.
- Houser, C., Masters, G., Flanagan, M., & Shearer, P., 2008. Determination and analysis of long-wavelength transition zone structure using SS precursors, *Geophys. J. Int.*, **174**, 178–194.
- Ita, J. & Stixrude, L., 1992. Petrology, elasticity, and composition of the mantle transition zone, *Journal of Geophys. Res.*, **97**, 6849–6866.
- Kaviani, A., Sandvol, E., Moradi, A., Rumpker, G., Tang, Z., & Mai, P. M., 2018. Mantle transition zone thickness beneath the Middle East: Evidence for segmented Tethyan slabs, delaminated lithosphere, and lower mantle upwelling, *Journal of Geophys. Res.: Solid Earth*, **123**, 4886–4905.
- Kennett, B. L. N. & Engdahl, E. R., 1991. Traveltimes for global earthquake location and phase identification, *Geophys. J. Int.*, **105**, 429–465.
- Kosarev, G., Oreshin, S., Vinnik, L., & Makeyeva, L., 2017. Mantle transition zone beneath the central Tien Shan: Lithospheric delamination and mantle plumes, *Tectonophysics*, **723**, 172–177.

- Kustowski, B., Ekstrom, G., & Dziewonski, A., 2008. Anisotropic shear-wave velocity structure of the Earth's mantle: A global mode, *J. Geophys. Res.*, **113**, doi:10.1029/2007JB005169.
- Laske, G., Masters, G., Ma, Z., & Pasyanos, M., 2013. Update on CRUST1.0 — a 1-degree global model of Earth's crust, *EGU General Assembly Conference Abstracts*, **15**, 2658.
- Lawrence, J. & Shearer, P., 2006. A global study of transition zone thickness using receiver functions, *J. Geophys. Res.*, **111**, doi:10.1029/2005JB003973.
- Lawrence, J. F. & Shearer, P. M., 2008. Imaging mantle transition zone thickness with SdS-SS finite-frequency sensitivity kernels, *Geophysical Journal International*, **174**, 143–158.
- Lee, S.-H., Rhie, J., Park, Y., & Kim, K.-H., 2014. Topography of the 410 and 660 km discontinuities beneath the Korean peninsula and southwestern Japan using teleseismic receiver functions, *J. Geophys. Res. Solid Earth*, **119**, 7245–7257.
- Lessing, S., Thomas, C., Rost, S., Cobden, L., & Dobson, D. P., 2014. Mantle transition zone structure beneath India and western China from migration of PP and SS precursors, *Geophys. J. Int.*, **197**, 396–413.
- Li, X. & Yuan, X., 2003. Receiver functions in northeast China - implications for slab penetration into the lower mantle in northwest Pacific subduction zone, *Earth and Planetary Science Letters*, **216**, 679–691.
- Liu, K. & Zhou, Y., 2016. Global Rayleigh wave phase-velocity maps from finite-frequency tomography, *Geophysical Journal International*, **205**, 51–66.
- Moulik, P. & Ekstrom, G., 2014. An anisotropic shear velocity model of the Earth's mantle using normal modes, body waves, surface waves and long-period waveforms, *Geophys. J. Int.*, **199**, 1713–1738.
- Neele, F. & de Regt, H., 1999. Imaging upper-mantle discontinuity topography using underside-reflection data, *Geophys. J. Int.*, **137**, 91–106.

- Neele, F., de Regt, H., & VanDecar, J., 1997. Gross errors in upper-mantle discontinuity topography from underside reflection data, *Geophys. J. Int.*, **129**, 194–204.
- Panning, M. & Romanowicz, B., 2006. A three-dimensional radially anisotropic model of shear velocity in the whole mantle, *Geophys. J. Int.*, **167**, 361–379.
- Revenaugh, J. & Jordan, T. H., 1991. Mantle layering from ScS reverberations: The transition zone, *Journal of Geophysical Research*, **96**, 19,763–19,780.
- Ritsema, J., Deuss, A., van Heijst, H., & Woodhouse, J., 2011. S40rts: a degree-40 shear-velocity model for the mantle from new rayleigh wave dispersion, teleseismic traveltimes and normal-mode splitting function measurements, *Geophys. J. Int.*, **184**, 1223–1236.
- Schaeffer, A. & Levedev, S., 2013. Global shear speed structure of the upper mantle and transition zone, *Geophys. J. Int.*, **194**, 417–449.
- Schmerr, N. & Garnero, E., 2006. Investigation of upper mantle discontinuity structure beneath the central Pacific using SS precursors, *Journal of Geophys. Res.*, **111**, doi:10.1029/2005JB004197.
- Schmerr, N. & Garnero, E. J., 2007. Upper mantle discontinuity topography from thermal and chemical heterogeneity, *Science*, **318**, 623–626.
- Schmerr, N. & Thomas, C., 2011. Subducted lithosphere beneath the Kuriles from migration of PP precursors, *Earth and Planetary Science Letters*, **311**, 101–111.
- Shearer, P. M., 1991. Constraints on upper mantle discontinuities from observations of long-period reflected and converted phases, *Journal of Geophysical Research*, **96**, 18,147–18,182.
- Shen, Y., Sheehan, A. F., Dueker, K. G., de Groot-Hedlin, C., & Gilbert, H., 1998. Mantle discontinuity structure beneath the southern East Pacific Rise from P-to-S converted phases, *Science*, **280(5367)**, 1232–1235.

- Wang, X., Li, J., & Chen, Q.-F., 2017. Topography of the 410km and 660km discontinuities beneath the Japan Sea and adjacent regions by analysis of multiple-ScS waves, *J. Geophys. Res. Solid Earth*, **122**, 1264–1283.
- Wang, Y. & Pavlis, G. L., 2016. Roughness of the mantle transition zone discontinuities revealed by highresolution wavefield imaging, *Journal of Geophysical Research*, **121**, doi:10.1002/2016JB013205.
- Xue, J., Zhou, Y., & Chen, Y., 2015. Tomographic resolution of plume anomalies in the lowermost mantle, *Geophysical Journal International*, **201**, 979–995.
- Zheng, Z., Ventosa, S., & Romanowicz, B., 2015. High resolution upper mantle discontinuity images across the Pacific Ocean from SS precursors using local slant stack filters, *Geophys. J. Int.*, **202**, 175–189.
- Zhou, Y., 2009. Multimode surface wave sensitivity kernels in radially anisotropic earth media, *Geophys. J. Int.*, **176**, 865–888.
- Zhou, Y., 2018. Anomalous mantle transition zone beneath the Yellowstone hotspot track, *Nature Geoscience*, **11**, 449–453.
- Zhou, Y., Dahlen, F. A., Nolet, G., & Laske, G., 2005. Finite-frequency effects in global surface-wave tomography, *Geophys. J. Int.*, **163**, 1087–1111.
- Zhou, Y., Nolet, G., Dahlen, F. A., & Laske, G., 2006. Global upper-mantle structure from finite-frequency surface-wave tomography, *Journal of Geophys. Res.*, **111**, doi:10.1029/2005JB003677.

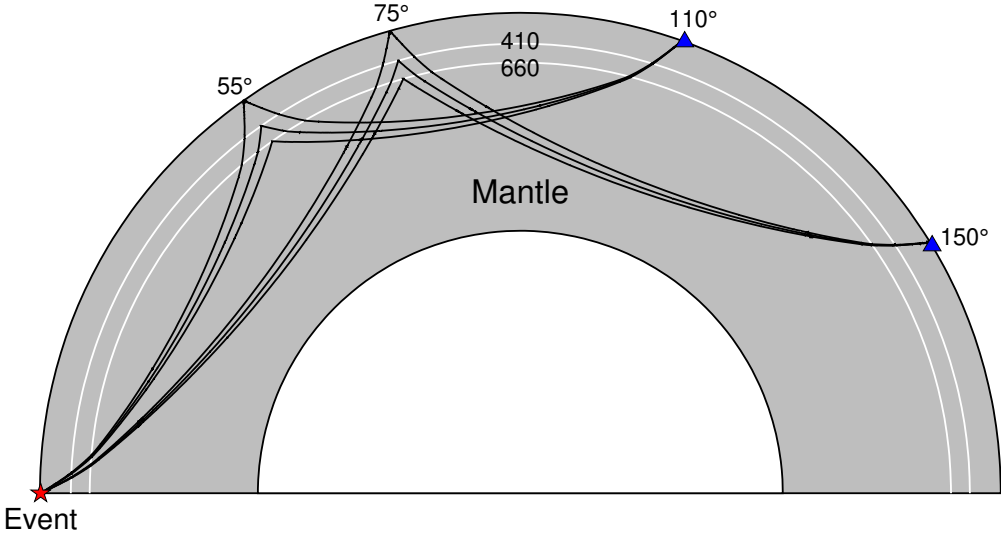


Figure 2.1: Ray paths of SS , $S410S$ and $S660S$ waves at epicentral distances of 110° and 150° . The star and triangles indicate locations of the earthquake event and the recording stations, respectively.

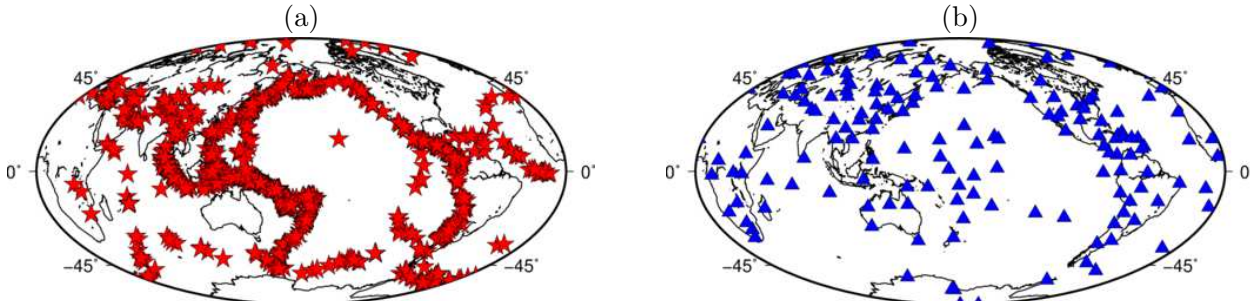


Figure 2.2: (a) Distribution of 1117 teleseismic earthquakes ($6.0 < M_w < 8.5$) used in this study. The epicentral distance of the dataset ranges from 90° to 160° . (b) Locations of 150 GSN stations used in this study.

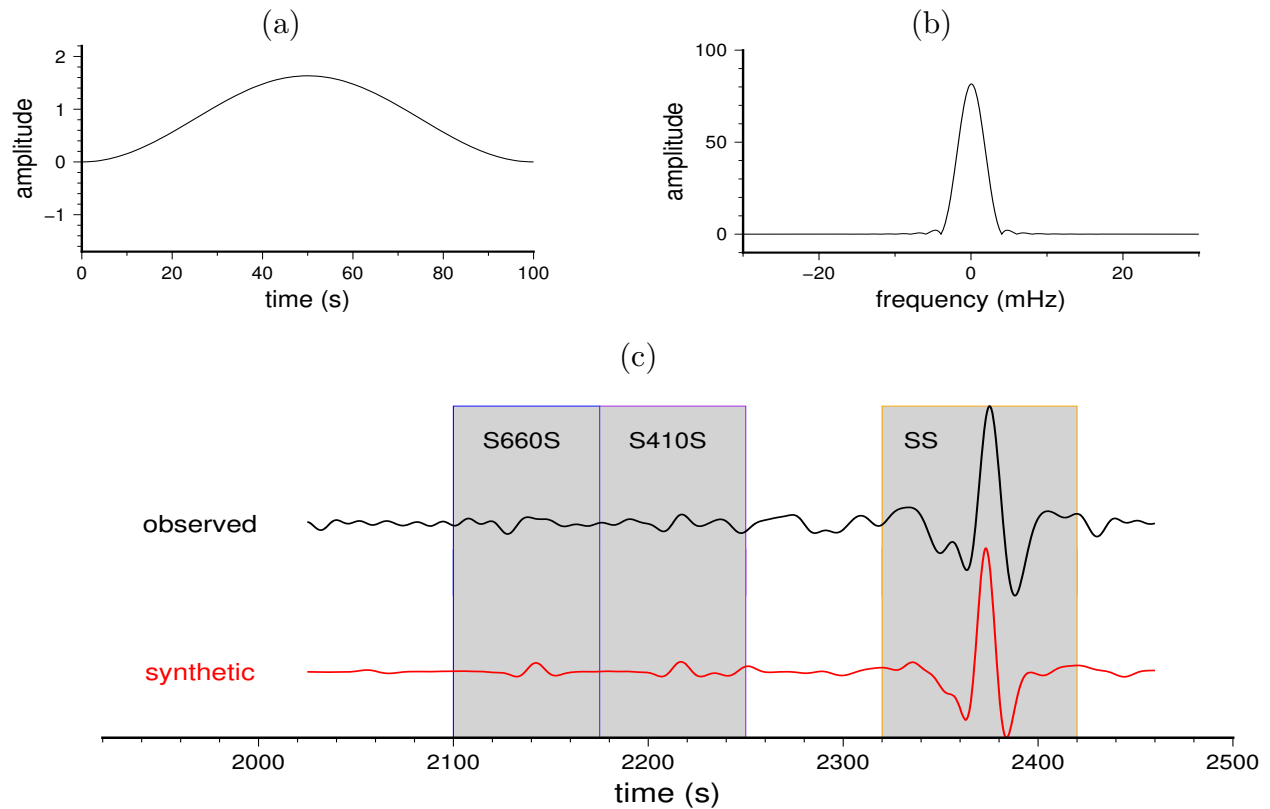


Figure 2.3: (a) and (b) are a 100-second cosine taper in the time domain and its spectrum in the frequency domain, respectively. (c) Example observed and synthetic seismograms with clear *SS*, *S410S* and *S660S* waves, recorded at station EFI (longitude= -58.06° , latitude= -51.68°) for a 2003 Indonesia earthquake ($M_w = 6.9$). The shaded areas indicate time windows used for traveltimes measurements.

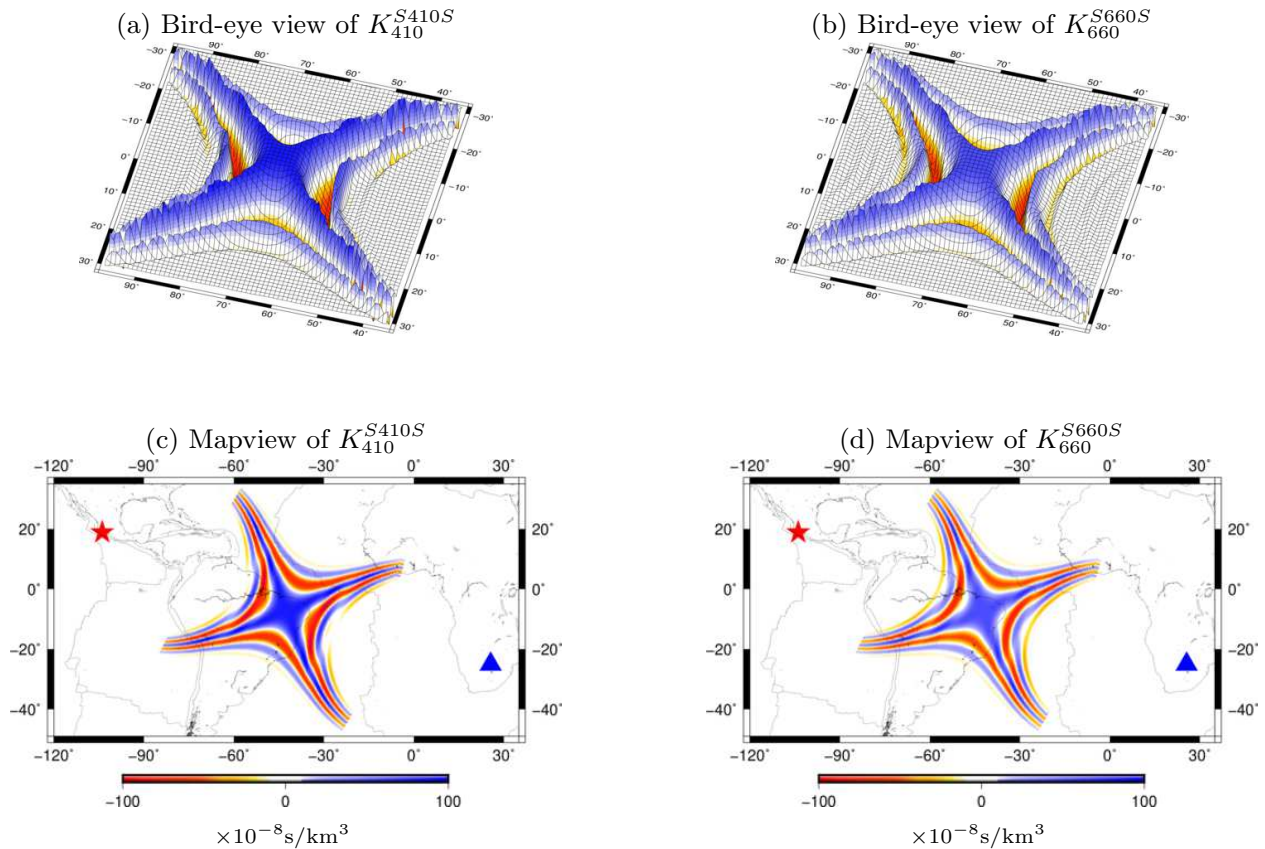


Figure 2.4: (a) Bird-eye view of example finite-frequency sensitivity of an $S410S$ wave at a period of 20 seconds to depth perturbations of the 410-km discontinuity. The epicentral distance is 133° and the mapview of the sensitivity kernel is plotted in (c) where the earthquake (star) is located off the west coast of Mexico and the station LBTB (triangle) is in Africa. The sensitivity of the corresponding $S660S$ to depth perturbations on the 660-km discontinuity is plotted in (b) and (d).

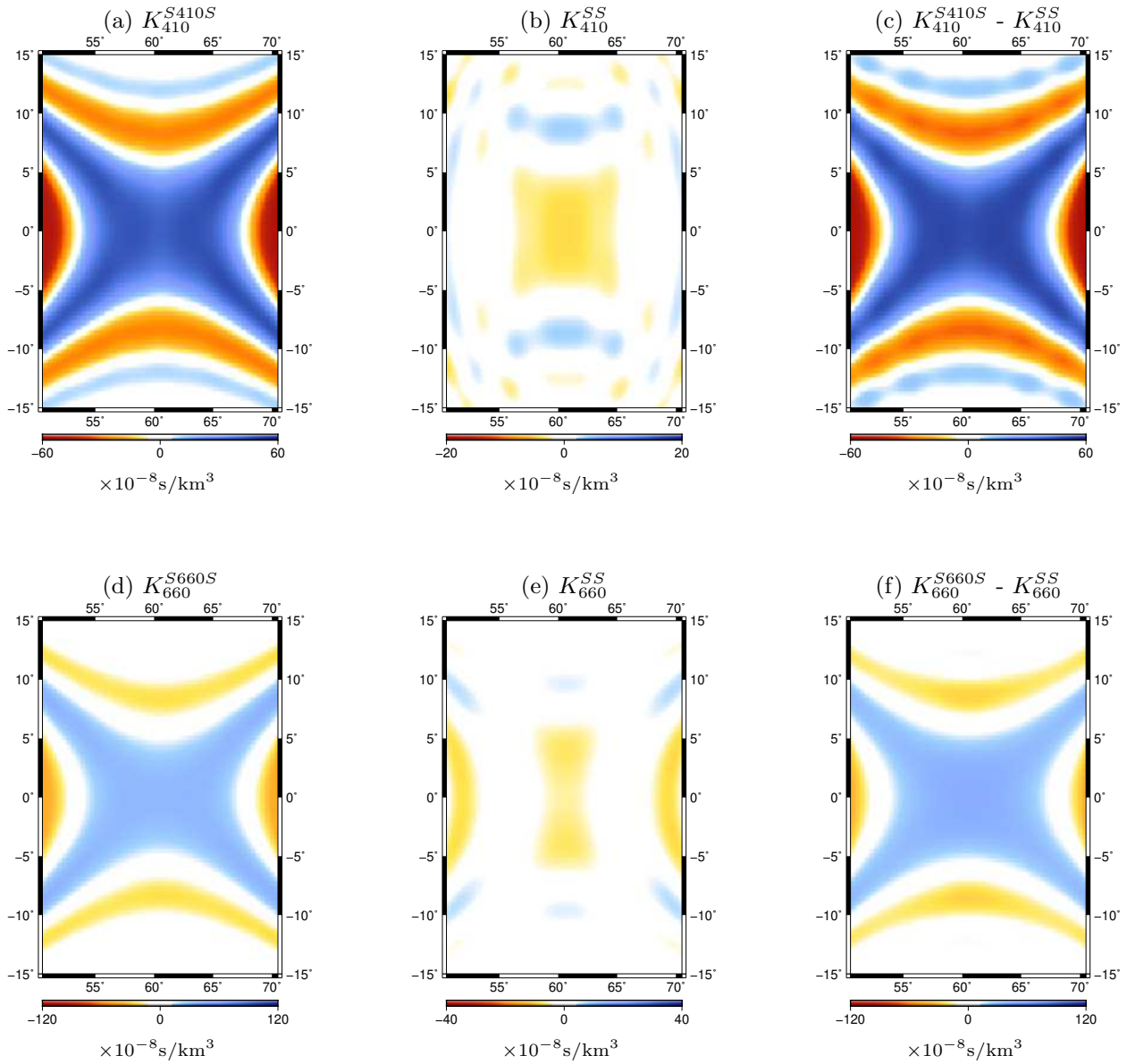


Figure 2.5: Zoom-in view of sensitivity kernels of S_{410S} , S_{660S} and SS waves recorded at station BJT (longitude=116.17°, latitude=40.02°) with an epicentral distance of 120° from a M_w 6.3 earthquake in Puerto Rico area. The SS sensitivities are much smaller in magnitude and plotted on difference color scales. SdS and SS waves have different sensitivity polarity as a depression of the 410-km (or 660-km) discontinuity will speed up SdS waves but slow down SS waves, and vice versa for an uplift.

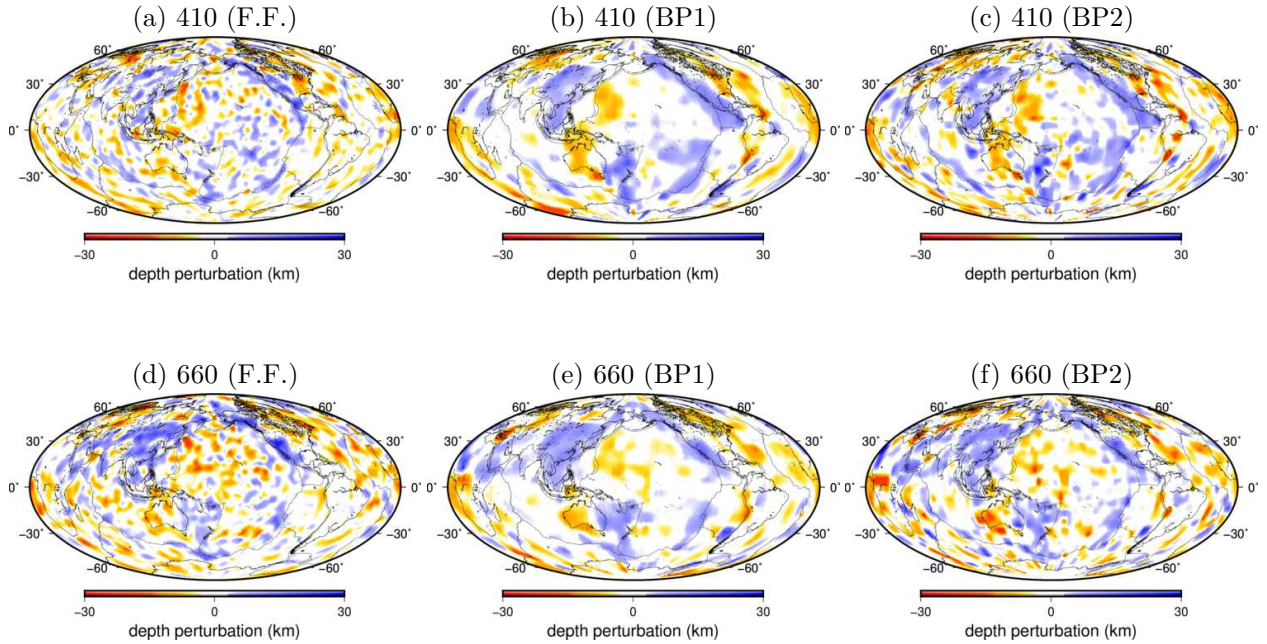


Figure 2.6: Finite-frequency effects in imaging depth perturbations of the 410-km and the 660-km discontinuities. (a) depth perturbations of the 410-km discontinuity inverted from SdS - SS traveltimes measurements using finite-frequency sensitivity kernels. (b) and (c) are ray-theoretical back-projection models where perturbations are averaged in a moving circular cap with a radius of 6° (BP1) and 4° (BP2). (d)–(f) are the finite-frequency and ray-theoretical back-project models for depth perturbations on the 660-km discontinuity. The finite-frequency model and ray-theoretical back-project models are obtained using the same traveltimes data without crustal and mantle wavespeed corrections.

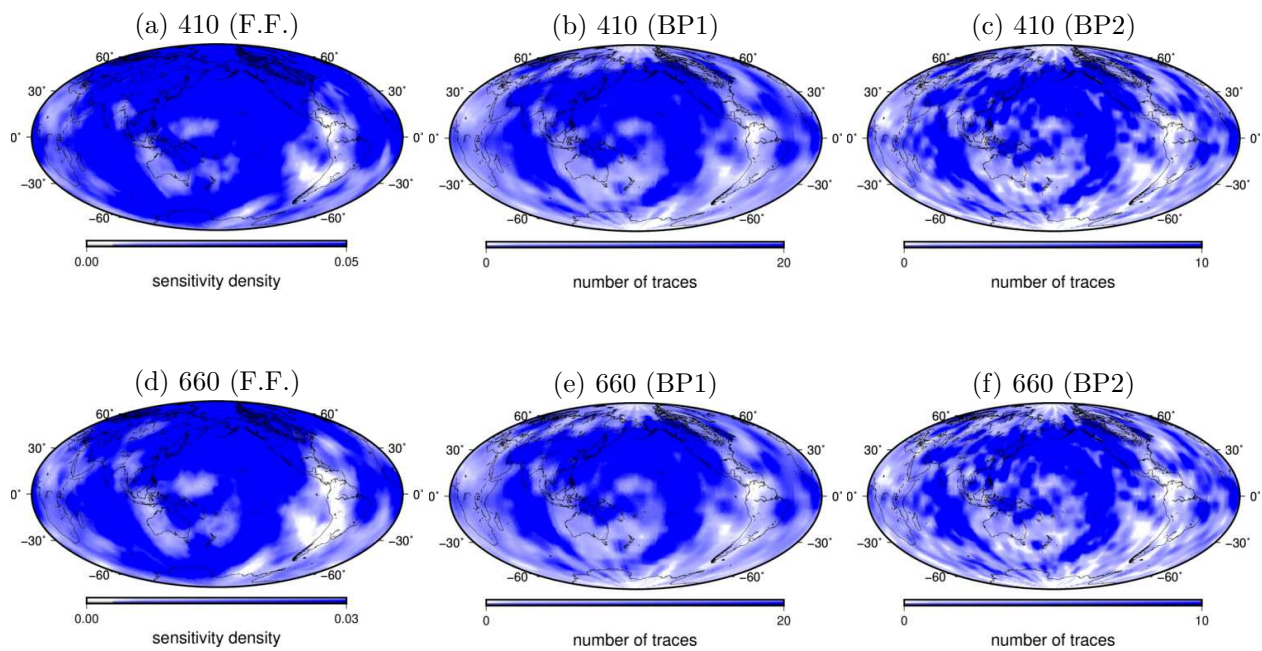


Figure 2.7: (a) is the sensitivity density (diagonal elements of the matrix $A^T A$) in finite-frequency tomography of the 410-km discontinuity. (b) and (c) are the number of traces per circular cap in the back-projection models BP1 and BP2, respectively. (d)-(f) are the same as (a)-(c) but for the 660-km discontinuity models in Fig. 2.6.

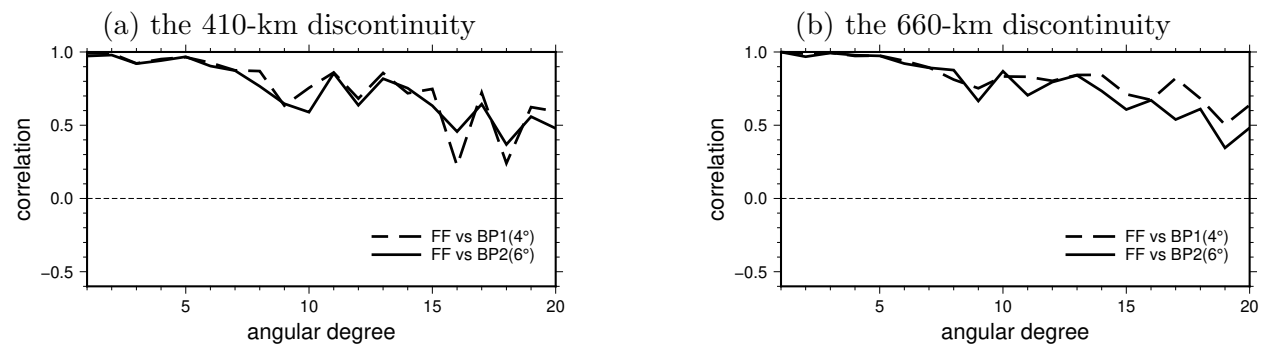


Figure 2.8: (a) Correlation coefficient as a function of spherical harmonic degree between the finite-frequency 410-km discontinuity model and the two back-projection models in Fig. 2.6. (b) Same as (a) but for the 660-km discontinuity models.

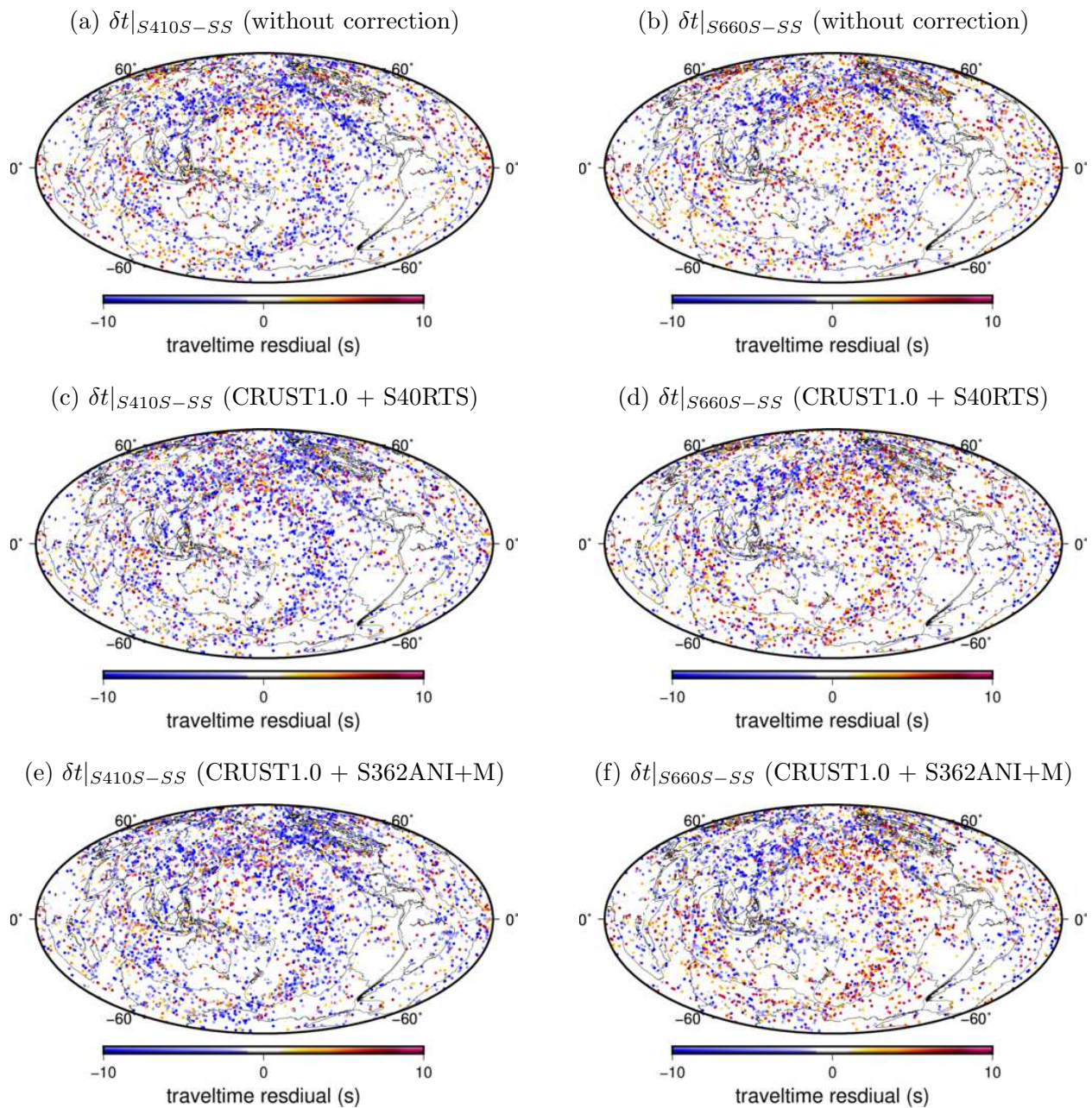


Figure 2.9: (a) and (b) are $S410S-SS$ and $S660S-SS$ differential traveltime measurements at a period of 20 s without crustal and mantle corrections. The measurements are plotted at the bounce points of SS waves. (c) and (d) are the same as (a) and (b) but with data corrected for crustal and mantle wavespeed variations using models CRUST1.0 and S40RTS. (e) and (f) are the same as (c) and (d) but with mantle corrections using model S362ANI+M.

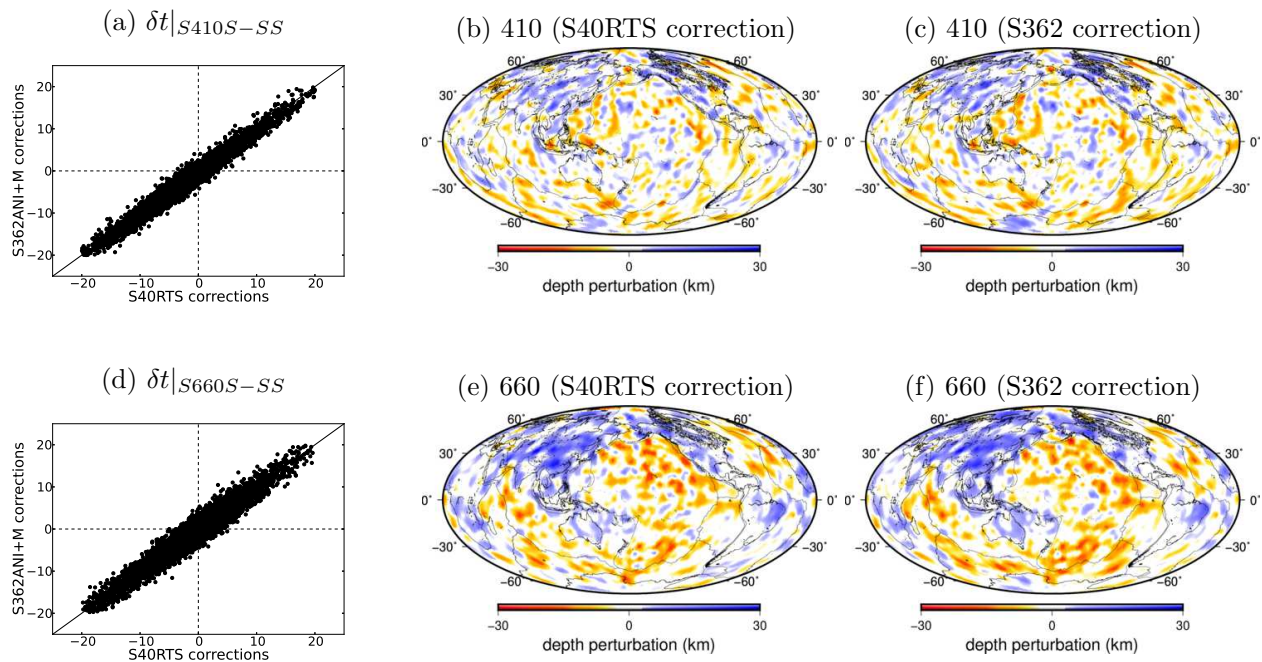


Figure 2.10: (a) Scatterplot of $S410S-SS$ differential traveltime measurements with mantle corrections made using model S40RTS (Ritsema et al., 2011) and model S362ANI+M (Moulik & Ekstrom, 2014). (b) and (c) are depth perturbations of the 410-km discontinuity from finite-frequency tomography with traveltime corrections made using model S40RTS and S362ANI+M, respectively. (d)-(f) are the same as (a)-(c) but for the 660-km discontinuity.

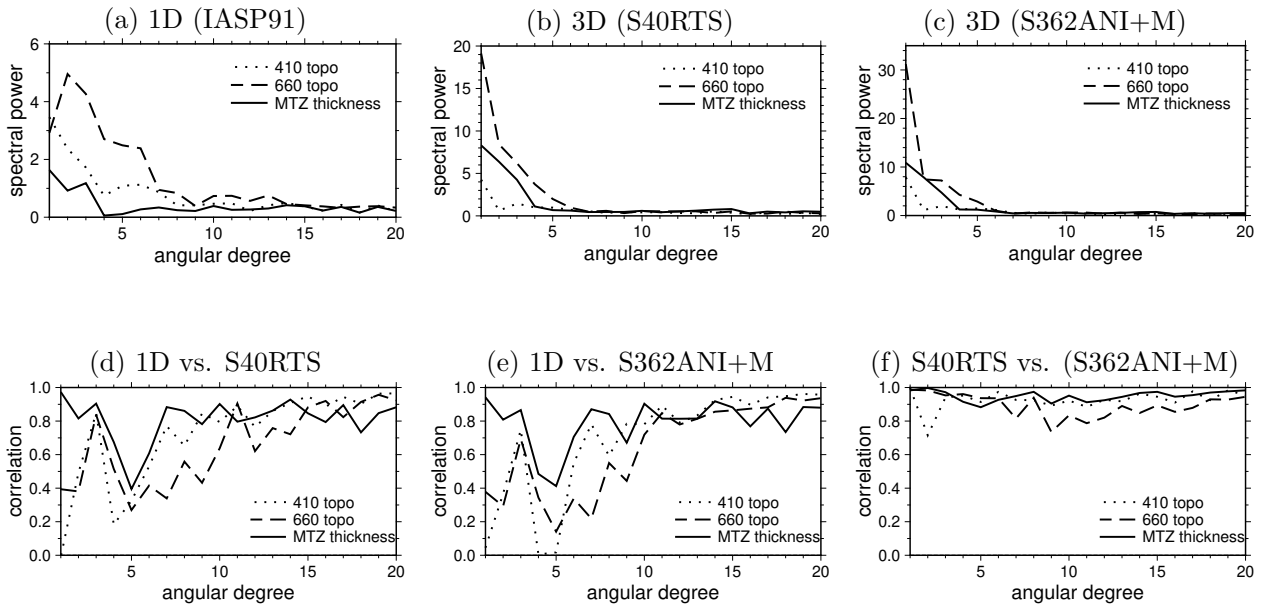


Figure 2.11: (a) spectra power per spherical harmonic degree of the finite-frequency 410-km and 660-km discontinuity models in Fig. 2.6 and the corresponding mantle transition zone thickness. (b) and (c) are the same as (a) but for discontinuity models in Fig. 2.10 where traveltimes corrections have been made using model S40RTS and S362ANI+M respectively. (d) Correlation coefficients as a function of spherical harmonic degree between the discontinuity models obtained with and without corrections based on model S40RTS (Figs 2.6 & 2.10). (e) is the same as (d) for models with and without traveltimes corrections made using model S362ANI+M. (f) correlation coefficients between models obtained with corrections made using models S40RTS and S362ANI+M.

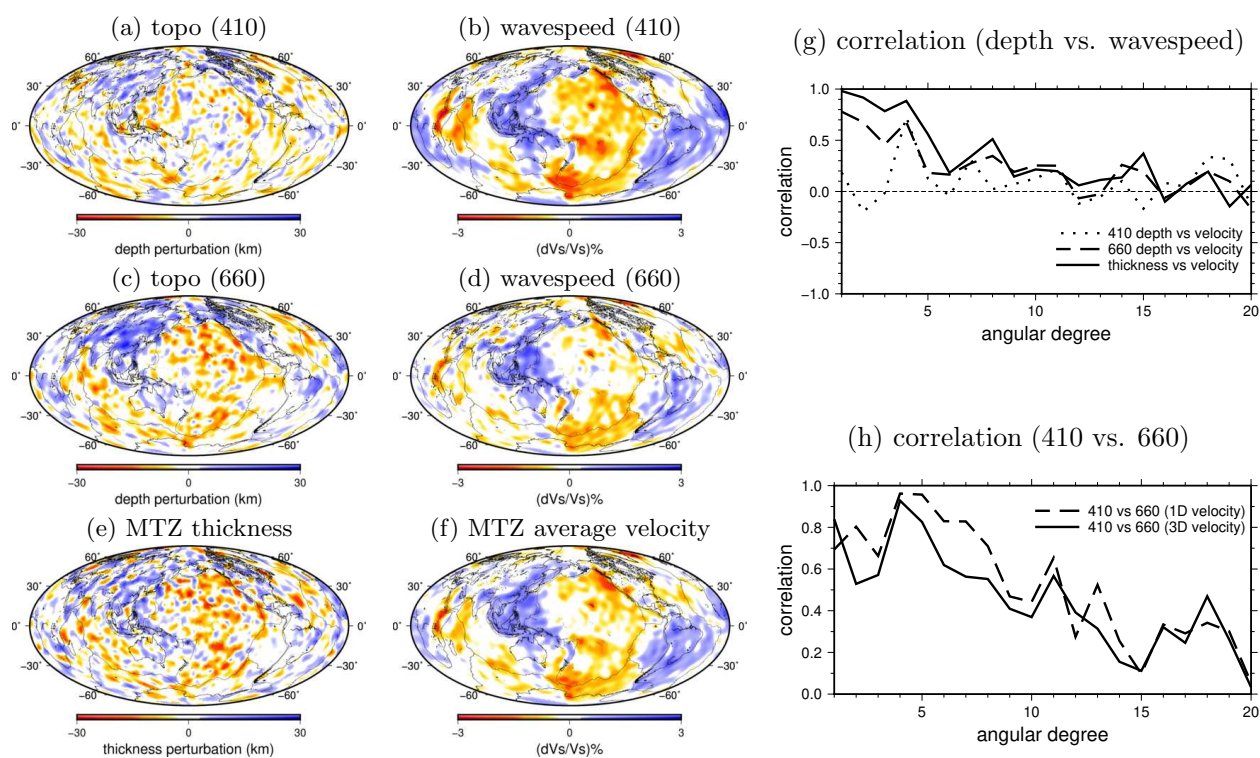


Figure 2.12: (a) and (c) are the finite-frequency 410-km and 660-km discontinuity models with data corrections made using model S40RTS (Fig. 2.10). (b) and (d) are wavespeed perturbations in model S40RTS at depths of 410 and 660 km, respectively. (e) and (f) are maps of the mantle transition zone thickness and average wavespeed in the mantle transition zone, respectively. (g) correlation between discontinuity depth perturbations and wavespeed perturbations as a function of spherical harmonic degree; (f) correlation between the 410-km and 660-km discontinuity models in 1-D (no correction) and 3-D (with correction) wavespeed models.

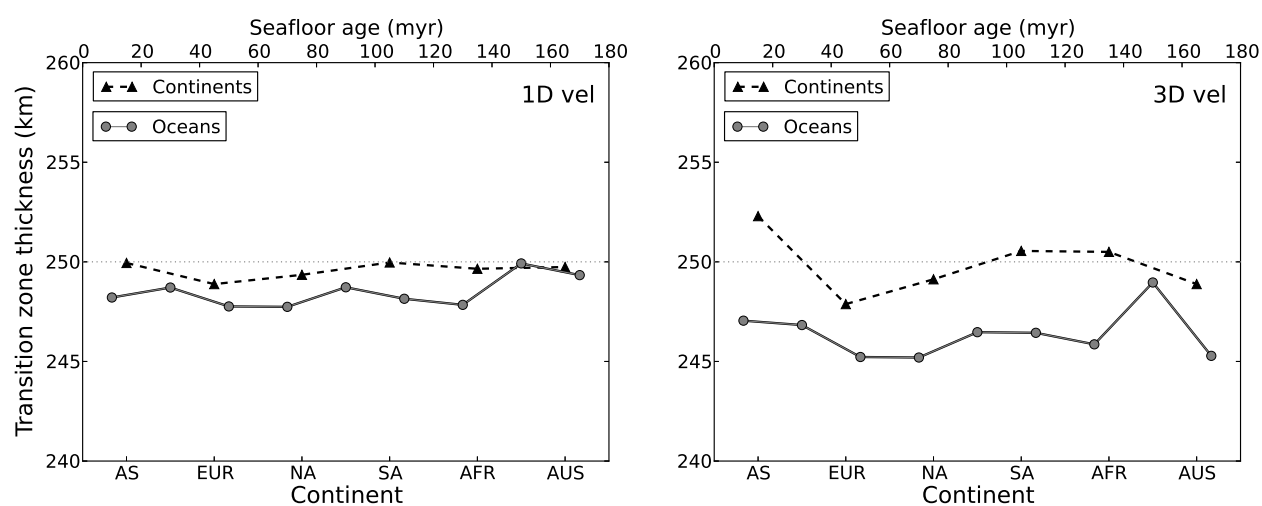


Figure 2.13: Average mantle transition zone thickness in 1-D (left) and 3-D (right) wavespeed models. In the oceans, the thickness is averaged over every 20-million year age band and there is no apparent dependence on the age of the sea floor. The average thickness of the mantle transition zone in continental areas is calculated for Asia (AS), Europe (EUR), North America (NA), South America (SA), Africa (AFR) and Australia (AUS). The mantle transition zone is thicker under the continents than under the oceans, especially after crustal and wave speed corrections are applied.

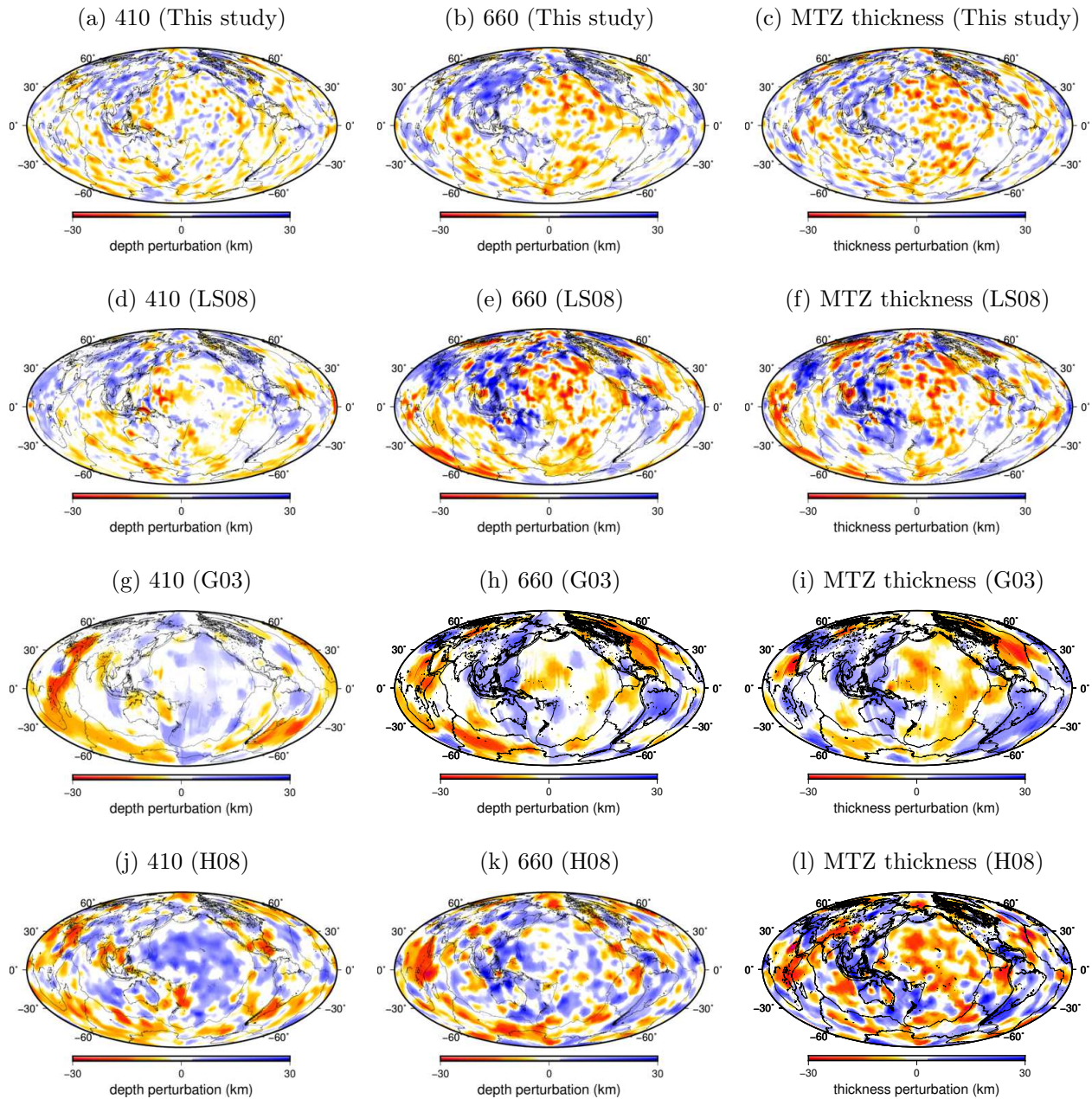


Figure 2.14: This figure compares the topography of the 410-km and 660-km discontinuity as well as the thickness of the mantle transition zone from (a)-(c) this study, (d)-(f) Lawrence & Shearer (2008), (g)-(i) Gu et al. (2003) and (j)-(l) Houser et al. (2008).

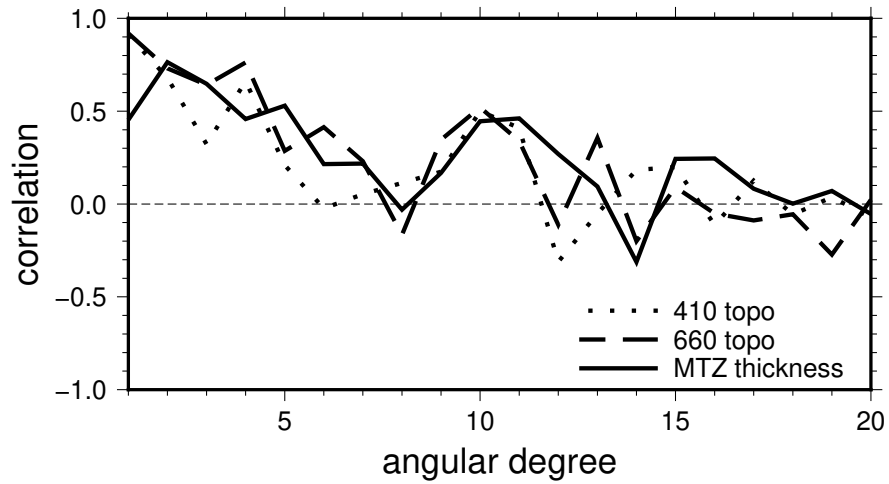


Figure 2.15: Correlation between discontinuity models in this study and model LS08 (Lawrence & Shearer, 2008). The coefficients are plotted as function of spherical harmonic degree from 1 to 20 for depth perturbations on the 410-km discontinuity, the 660-km discontinuity and the thickness of the mantle transition zone.

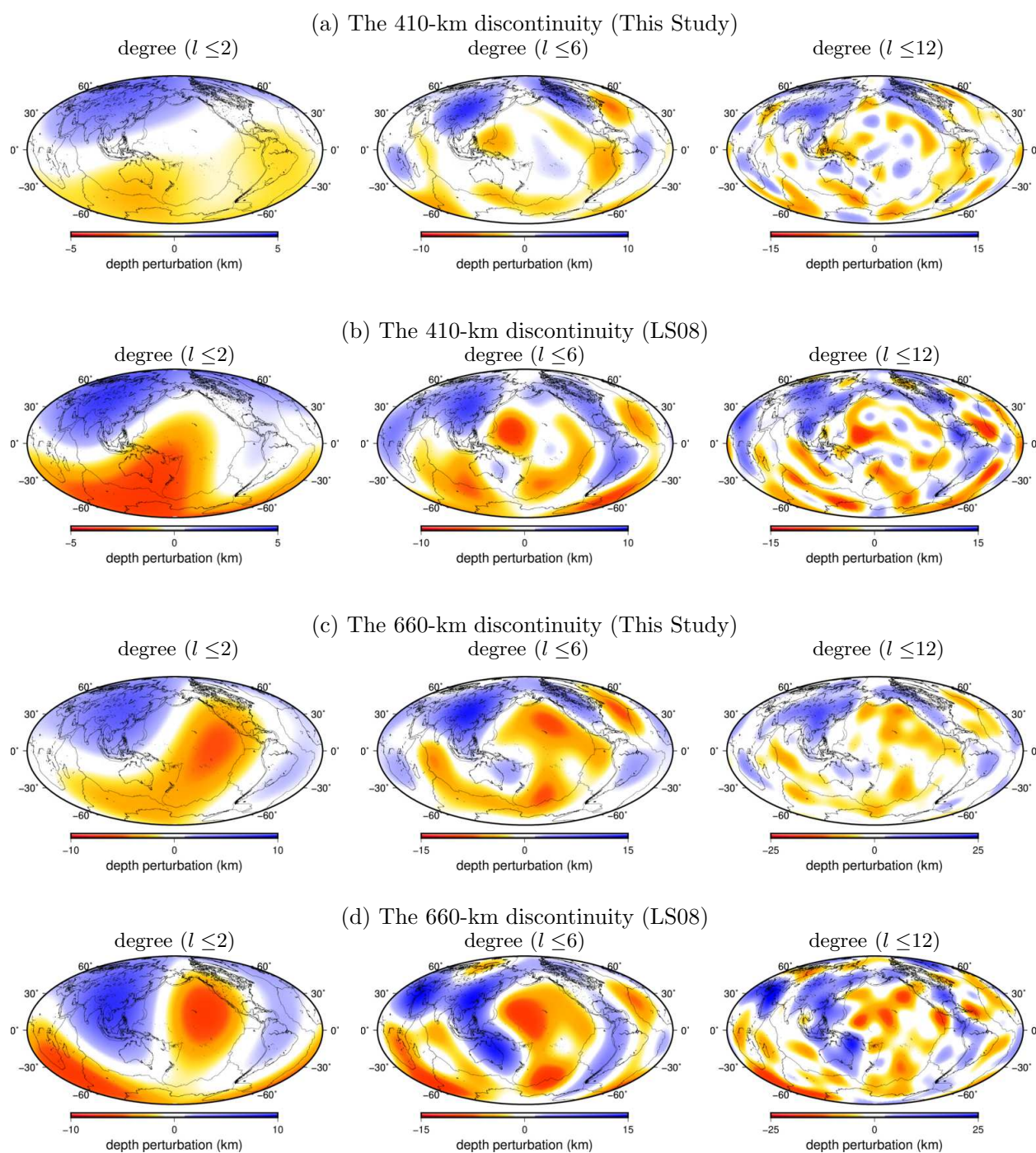


Figure 2.16: (a) the 410-km discontinuity model in this study filtered to spherical harmonic $l \leq 2$, $l \leq 6$ and $l \leq 12$. (b) is the same as (a) but for the 410-km discontinuity model from Lawrence & Shearer (2008). (c) and (d) are the same as (a) and (b) but for the 660-km discontinuity.

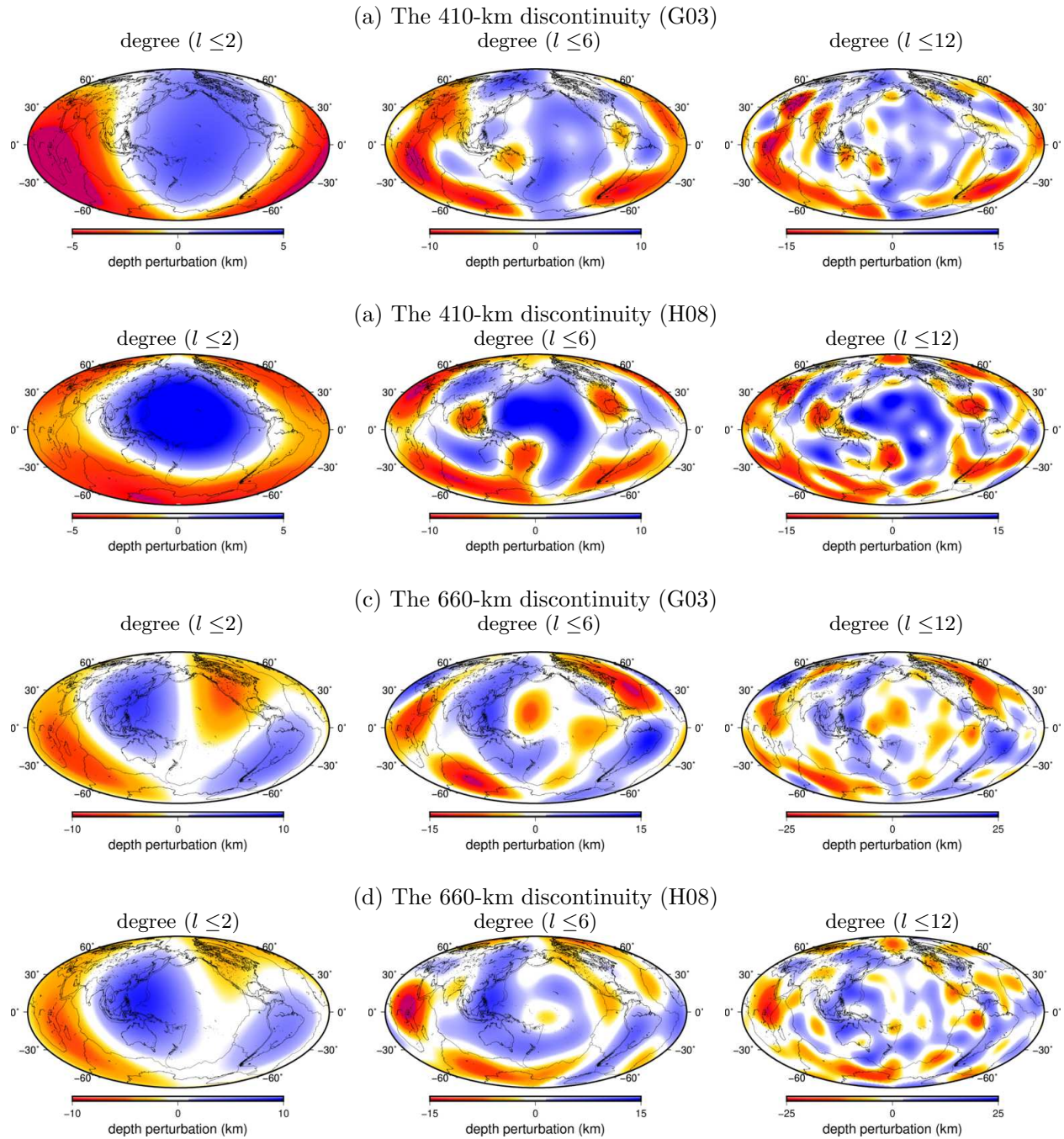


Figure 2.17: Same as Fig. 2.16 but for models from Gu et al. (2003) and Houser et al. (2008).

Chapter 3

Global Return Flow above Stagnant Slabs from Mantle Transition Zone Tomography

(An edited version of this chapter was reviewed by Science Advances and a revision is in submission.)

3.1 Introduction

The movement of surface tectonic plates is generally considered to be driven by the pulling force associated with slab subduction (Forsyth & Uyeda, 1975). Upwellings at mid-ocean ridges are passive return flows in the shallow mantle in response to subduction at convergent plate boundaries. For example, seismic anomalies beneath the East Pacific Rise spreading centers are mostly confined in the uppermost 250 km (Webb & Forsyth, 1998). Subduction-driven convection is well understood in the upper mantle but convective mass exchange in the mid mantle remains unclear. The mantle transition zone (MTZ) between the upper mantle

and the lower mantle is bounded by two seismic discontinuities associated with pressure-induced mineral phase transitions, one from olivine to wadsleyite at about 410 km depth and a second one from ringwoodite to perovskite at about 660 km depth (Anderson, 1967; Ringwood, 1969). The 660-km discontinuity is generally considered a possible barrier for whole mantle convection due to its negative Clapeyron slope (Christensen, 1995). In contrast, the Clapeyron slope of the 410-km discontinuity is positive. This predicts an anti-correlation between depth perturbations of the 410-km and the 660-km discontinuities for purely thermal anomalies in the mantle transition zone.

In seismic tomography, both penetrating and stagnant slabs have been imaged in the mantle transition zone (Fukao, 2013). However, structures in the mantle transition zone are often not as well constrained as those in the upper or lower mantle. This is mainly because teleseismic body waves have turning depths in the lower mantle and fundamental-mode surface waves are only sensitive to structure in the shallow mantle. SS waves and their precursors S410S and S660S are waves reflected off the underside of the surface and the 410-km and the 660-km seismic interfaces, respectively. They provide constraints on depth perturbations of the two discontinuities and have been used to study the structure of the mantle transition zone (Shearer, 1991; Gu et al., 2003; Lawrence & Shearer, 2008; Houser et al., 2008). As secondary reflected waves, S410S and S660S waves (or SdS waves hereafter) are weak signals on recorded seismograms, and a common practice in global studies has been to stack their waveforms in a large circular area near their bounce points to improve signal-to-noise ratio (Shearer, 1991; Gu et al., 2003; Schmerr & Garnero, 2006). While the effects of using different bin sizes in stacking have been investigated (Houser et al., 2008; Flanagan & Shearer, 1998), it is understood that discontinuity structures may not be well resolved because of large Fresnel zones associated with SS waves and their precursors (Lawrence & Shearer, 2008). When the length scale of discontinuity topography is comparable to the characteristic seismic wavelength, finite frequency effects become important.

In this study, we build a global dataset of arrival time measurements of SS, S410S and S660S waves recorded at the Global Seismographic Network (GSN) to image depth perturba-

tions of the 410-km and 660-km discontinuities at a global scale. We calculate finite-frequency sensitivities of arrival time measurements in the framework of traveling-wave mode coupling, which take into account complete wave interactions in every measurement window. In addition to accounting for wave diffractive effects in seismic tomography, the finite-frequency sensitivities allow us to identify measurements that are significantly contaminated by multiples of a shallower interface or other seismic phases, in which case those measurements are excluded from imaging. This global dataset allow us to obtain high resolution depth perturbations of the two discontinuities based on finite-frequency tomography of differential travel times between SS waves and their precursors.

3.2 Data and Methods

We use broadband seismograms recorded at GSN stations for earthquakes occurred between January 2003 and September 2014. Instrument responses are removed and horizontal-component seismograms are rotated to obtain the radial- and transverse-component displacement seismograms. The transverse (SH) component seismograms are then band pass filtered between 0.01 and 0.1 Hz as SdS phases show best signal-to-noise ratio in this frequency range. To minimize possible interference between SdS waves and earthquake depth phases, we use earthquakes with focal depths shallower than 100 km. The moment magnitudes of the earthquakes range from 6.0 to 8.5 and the epicentral distances are between 90 and 160 degrees. This raw dataset contains about 150,000 traces.

To measure finite-frequency SS, S410S and S660S travel times, we carefully select seismograms with high-quality signals through visual inspection of each processed SH-component seismogram. We compare observed seismograms with synthetic seismograms calculated in a 1-D reference earth model IASP91 (Kennett & Engdahl, 1991) using traveling wave mode summation (Liu & Zhou, 2016). Traces with highly deformed SS waveforms are not used in this study. Travel time measurements are made with respect to IASP91 synthetic seismo-

grams and measurement time windows are determined based the synthetic and observed SS waves and their precursors. We choose time windows manually to ensure that the dominant energy of the measured phase is centered in the window. The length of the measurement window varies from 70 to 120 seconds. To obtain frequency-dependent travel time measurements, a cosine taper is applied in spectral estimates following the work of Deng & Zhou (2015). Finite-frequency effects in this dataset and comparisons with ray-theoretical tomography have been documented in **Chapter 2**. In this study, we focus on tomographic results based on measurements at 20 seconds period. Finally, we take advantage of calculated finite-frequency sensitivities in examining each measurement to identify possible complex wave interactions due to multiple phases arriving within a measurement window. This leaves a total of about 6400 seismograms for 1110 earthquakes, which provide good coverage in the oceans as well as in major subduction zones, except for in South America and its adjacent southern Pacific Ocean.

Lateral variations in crustal structure as well as wave speed variations in the bulk mantle may introduce travel time shifts on SS and SdS waves. We calculate crustal corrections based upon traveltimes differences between IASP91 models with and without a global crustal structure, CRUST 1.0 (Laske et al., 2013). The crust is 20 km thick in the reference model IASP91 and maximum crustal corrections using model CRUST1.0 are about 5 seconds for SS waves reflected off the Tibetan Plateau where the thickness of the crust reaches about 80 km. Overall, the SdS-SS differential measurements at 20 seconds period with and without crustal corrections show minor differences. We calculate 3-D mantle wavespeed corrections using two existing global models, S40RTS (Ritsema et al., 2011) and S362ANI+M (Moulik & Ekström, 2014). The choice of mantle model in wavespeed corrections does not affect major structures in discontinuity. We focus on mantle wave speed corrections based on model S40RTS in this chapter.

3.2.1 Finite-frequency sensitivity kernels

We calculate finite-frequency sensitivities of SS and SdS traveltimes to boundary depth perturbations based on Born (single-scattering) approximation in the frame work of travelling-wave mode coupling (Deng & Zhou, 2015; Zhou, 2009). The boundary sensitivity kernels fully account for source radiation patterns, phase interactions as well as time-domain windowing and tapering applied in making frequency-dependent measurements. Travel time differences between observed and synthetic SdS waves ($\delta t|_{SdS}$) can be expressed as a two-dimensional integration over the global surface of the corresponding seismic discontinuity Σ

$$\delta t|_{SdS}(\omega) = \iint_{\Sigma} K_{\Sigma}^{SdS}(\mathbf{x}, \omega) \delta d(\mathbf{x}) d\Sigma, \quad (3.1)$$

where $K_{\Sigma}^{SdS}(\mathbf{x}, \omega)$ is the sensitivity of an *SdS* traveltime measurement at angular frequency ω to depth perturbations $\delta d(\mathbf{x})$ on the corresponding seismic discontinuity.

For SS waves, the relation can be written as

$$\delta t|_{SS}(\omega) = \iint_{\Sigma} K_{\Sigma}^{SS}(\mathbf{x}, \omega) \delta d(\mathbf{x}) d\Sigma. \quad (3.2)$$

The linear relation between measurements and discontinuity depth perturbations in eqs (3.1) and (3.2) guarantees

$$\delta t|_{SdS}(\omega) - \delta t|_{SS}(\omega) = \iint_{\Sigma} [K_{\Sigma}^{SdS}(\mathbf{x}, \omega) - K_{\Sigma}^{SS}(\mathbf{x}, \omega)] \delta d(\mathbf{x}) d\Sigma. \quad (3.3)$$

3.2.2 The inverse problem

We parametrize the surface of the Earth using a set of spherical triangular grid points with a lateral spacing of about 4° . The tomographic problems are ill-posed and exact solutions do not exist, we solve a regularized least-square inverse problem

$$\|\mathbf{G}\mathbf{m} - \mathbf{d}\|^2 + \alpha^2 \|\mathbf{m}\|^2 = \text{minimum} \quad (3.4)$$

where \mathbf{G} is the kernel matrix, \mathbf{m} is the model vector, \mathbf{d} is the data vector and α is the Tikhonov regularization parameter. The minimization leads to

$$(\mathbf{G}^T \mathbf{G} \mathbf{m} - \mathbf{G}^T \mathbf{d}) + \alpha^2 \mathbf{m} = 0. \quad (3.5)$$

We solve the above inverse problem based on singular value decomposition of matrix \mathbf{G} ,

$$\mathbf{G} = \mathbf{U} \mathbf{\Lambda} \mathbf{V}^T. \quad (3.6)$$

Where $\mathbf{\Lambda}$ is a rectangular diagonal matrix containing singular values λ_i , and \mathbf{U} and \mathbf{V} contain left and right singular vectors, \mathbf{u}_i and \mathbf{v}_i , respectively.

The Tikhonov solution of the inverse problem can be written as

$$\mathbf{m} = \sum_{j=1}^p \left(\frac{\lambda_j^2}{\lambda_j^2 + \alpha^2} \right) \frac{\mathbf{u}_j^T \mathbf{d}}{\lambda_j} \mathbf{v}_j, \quad (3.7)$$

where p is the rank of the singular value matrix.

The corresponding resolution matrix is

$$\mathbf{R} = \mathbf{V} \mathbf{F} \mathbf{V}^T, \quad (3.8)$$

where \mathbf{F} is diagonal matrix with elements $\lambda_j^2 / (\lambda_j^2 + \alpha^2)$. The tradeoff between data misfit and model norm for different regularization parameter α as well as resolutions of the optimal models are plotted in Figs 3.1 & 3.2.

3.3 The Global Subduction Zones

The most striking feature in the discontinuity maps is large-scale depressions in both the 410-km and 660-km discontinuities around the Pacific subduction zones Fig. 3.3. The circum-Pacific distribution of the positive correlation is best illustrated in Fig. 3.4 where positive correlation (in blue) is represented by the sum of the 410-km and 660-km discontinuity perturbations in regions where both discontinuities experience significant depressions (>5

km). Travel time corrections made using existing crust and bulk mantle models do not affect the general positive correlation along the circum-Pacific subduction zones (Fig. 3.3). The global data distribution is not uniform but show reduced coverage in Africa, South Asia and Northwest Australia and minimum data sampling in South America and adjacent oceans (Fig. 3.2). In Fig. 3.5, resolution tests on the 410-km and 660-km discontinuity models using spherical harmonic “checkerboard” at two different length scales ($l = 12$ and $l = 20$) show that structures are well resolved in Eurasia, North America, the Pacific Ocean and the Indian Ocean, consistent with sensitivity density and diagonal elements of the resolution matrix (Fig. 3.2).

The strong positive correlation in the Pacific subduction zones is somewhat counter-intuitive, because thermal variations due to a cold slab in the mantle transition zone would predict an “anti-correlation” between the two discontinuities. This positive correlation is largely absent in previous global models (Fig. 3.6) but in good agreement with several regional scale studies based on SS precursors and receiver functions (Shen et al., 2008; Heit et al., 2010). However, interpretations in regional studies have been difficult as this positive correlation is not expected in the general context of subduction. The global distribution of the MTZ discontinuity anomalies indicates a general subduction origin associated with stagnant slabs, possibly warm return flows from the lower mantle replacing the gradually sinking stagnant slabs.

In other subduction zones, the correlation between the 410-km and 660-km discontinuity depth perturbations is much weaker (Fig. 3.4). The lack of positive correlation between the 410 and the 660 in the Alpine-Tethys region is consistent with recent regional studies where most of the Tethyan lithosphere probably has sunk down to the lower mantle (Hafkenscheid et al., 2006). The 660-km discontinuity anomalies show similar structure to wave speed anomalies in the lower MTZ along the Tethyan suture zone (Fig. 3.3), extending from the Mediterranean through the northern Middle East into the Tibetan Plateau (Schaeffer & Lebedev, 2013). The 410-km discontinuity anomalies are much weaker and smaller in lateral extent (Fig. 3.3), indicating the absence of large-scale return flows warming up the shallower

mantle. In the Philippine trench and the Sunda trench, discontinuity anomalies are narrow features in the close proximity to current trench, consistent with steep penetration of subducted slabs across the mantle transition zone without much flattening above the 660-km discontinuity (Hall & Spakman, 2015). The spatial resolution of the discontinuity structures is limited as grid spacing in this study is about 4° , which is larger than the typical thickness of a subducted oceanic lithosphere.

3.4 Global Return Flow above Stagnant Slabs

In the western United States, the unprecedented deployment of EarthScope USArray allows us to synthesize wave speed tomographic models in this region with MTZ discontinuities to investigate the thermal structure in the mantle transition zone. The overall depressed 410-km and the 660-km discontinuities are in general agreement with recent regional studies using USArray receiver functions (Gao & Liu, 2014; Wang & Pavlis, 2016; Zhou, 2018). In seismic wave speed tomography, fast slab anomalies have been imaged in the lower MTZ from Idaho and Western Montana down to Utah and Colorado (Tian et al., 2011; Sigloch et al., 2008). In the upper MTZ, this region is dominated by seismic slow (warm) anomalies (Fig. 3.7). The overall anti-correlation in wave speed perturbations between the upper and lower MTZ supports a thermal origin of the discontinuity perturbations. Non-thermal origins such as water content have been proposed to explain low seismic wavespeed anomalies at the top of the MTZ, however, the positive correlation between the 410 and the 660 in this region can not be explained by slab hydration because increased water content would lead to a shallower 410-km discontinuity (Smyth & Jacobsen, 2006). We point out that wavespeed and discontinuity anomalies at those depths do not show exact correspondence in their locations, as due to the 3-D nature of the slab geometry as well as differences in model parametrization and resolution.

The stagnation of the subducted Farallon plate at the 660-km discontinuity and a warm

mantle above the slab is better illustrated in the 3-D wavespeed image in Fig. 3.8. To balance the sinking of a stagnant slab into the lower mantle, it requires an ascending return flow from the lower mantle. In both laboratory experiments and deep mantle subduction simulations, near-field poloidal convection cell have been observed (Kincaid & Griffiths, 2003; Schellart, 2008), and the poloidal component flows can become more significant with increasing viscosity (Piromallo et al., 2006). The overall much warmer upper MTZ indicates the poloidal mode of mass exchange occurs in the close proximity of the descending slab. To the east (ahead) of the subduction front, wavespeed and radial anisotropy indicate the presence of local upwellings from the lower mantle (Fig. 3.7 & 3.8). The upwellings are confined in the mantle transition zone and “feed” the broad slow anomalies above the stagnant slab. We interpret the upwellings as return flows in a superadiabatic mantle, driven by the sinking of the stagnant slab as well as “trench” retreat in the mantle transition zone (Fig. 3.8). In reality, subduction can be much more complicated than the simplified cartoon illustration in Fig. 3.8 due to complex processes such as slab fragmentation and the evolution of multiple subduction systems through time. In the Western US, it has been suggested that the mode switch from stagnant to penetration is associated with reversed polarity subduction of a section of slab between preexisting fracture zones on the Farallon plate, which generates a return flow through the slab gap, producing the Yellowstone volcanoes (Zhou, 2018).

In Eastern Asia, this strong positive correlation extends about 3000 kilometers westward inland from the present-day Ryukyu trench, with a gap roughly beneath the North China Craton (Fig. 3.9). This positive correlation between the 410-km and 660-km discontinuity topography largely agrees with wavespeed anomalies in the mid mantle (Schaeffer & Lebedev, 2013), where slow wavespeed dominates this region in the upper MTZ (~ 400 km) while fast anomalies are imaged in the lower MTZ (~ 650 km). Regional observations made on SS precursors also suggest the existence of reduced seismic wavespeed in the upper MTZ and depressions on the 410-km and 660-km discontinuities (Heit et al., 2010). The overall agreement indicates that the dominant mechanism associated with depth perturbations of the two discontinuities is also thermal. Radial anisotropy in the mantle transition zone is

consistent with local upwellings at the leading side (west) of subduction, and the anomalies are also largely confined in the mantle transition zone (Chang et al., 2014). The global wave speed model shown in Fig. 3.9 was obtained using multimode surface waves, which provide optimal sensitivities down to the mantle transition zone. While stagnant slab anomalies are a common feature in this region in wave speed tomographic models (Schaeffer & Lebedev, 2013; Moulik & Ekström, 2014), we point out that the geometry of wavespeed anomalies vary considerably at those depths among those models.

The large-scale MTZ discontinuity anomalies show two structures separated by a gap in the North China Craton. The gap is oriented in northeast direction, roughly parallel to the present-day Ryukyu trench. We interpret this structure as a result of stagnant slabs from two subduction systems, the current subduction of the Philippine sea plate which deposited slab materials east of the gap, and an earlier subduction of the Pacific plate beneath the Eurasia plate which deposited slab materials west of the North China Craton. The subduction of the Pacific plate in this region ceased about 40 million years ago as the growing Philippine sea plate moved northward into the place (Seno & Maruyama, 1984; Hall, 2012).

3.5 Structures in Global Oceanic Regions

In Fig. 3.4, the plume-like structures in the Pacific Ocean are characterized by an anti-correlation between the 410 and the 660, and they show significant differences in models with and without mantle wave speed corrections. For example, the correlation at the South Pacific Superswell changes polarity after wavespeed corrections. A plume-like anomaly west of the island of Hawaii becomes much weaker after wave speed corrections (Fig. 3.10). The only significant plume-like signature in the discontinuity models regardless of wave speed corrections is located south of Hess Rise. In examining published models, we noticed the anomaly was also present in an earlier finite-frequency model (Lawrence & Shearer, 2008). While the size of the anomaly is close to the resolution limit in our model (Fig. 3.5), the

general agreement among those models suggests that this anomaly south of Hess Rise is reasonably well resolved. The Geoid anomalies in the Pacific at intermediate wavelength indicates a possible mid-mantle origin in this region (Wessel et al., 1994). The geoid to topography ratio at Hess Rise is intermediate, lower than the Hawaii swell but higher than Shatsky Rise and Ontong-Java Plateau, suggesting possible deep compensation of a thermal swell (Sandwell & Renkin, 1988).

In oceanic regions, there was an age-dependent signature with both the 410 and the 660 becoming shallower as the seafloor gets older (Fig. 3.11). This pattern was introduced by slower S-wave speed in the upper mantle beneath younger seafloors in response to seafloor spreading, and, the age-dependence is removed after mantle wave speed corrections are applied (Figs 3.11 & 3.12). The average depths of the 410-km and 660-km discontinuities are about 411 km and 658 km, respectively. Overall, the oceanic mantle transition zone is about 2-3 km thinner than the global average and it does not show significant variations with seafloor age. The overall thinner mantle transition zone and slower seismic wave speed at those depths in global models (Schaeffer & Lebedev, 2013; Ritsema et al., 2011; Moulik & Ekström, 2014) suggests the existence of far-field return flows in the global oceanic mid mantle. The convection process is probably complex as the discontinuity structures in oceanic regions also show strong small-scale variations (Fig. 3.3).

3.6 Comparison with Previous Global Models

While large-scale correlations between surface tectonics and structures in the mantle transition zone have been suggested in global seismic discontinuity studies, global transition-zone models proposed by different research groups differ significantly from each other (Fig. 3.6). In analyzing previous global models, we discovered that the circum-Pacific distribution of the positive correlation becomes recognizable in the finite-frequency model LS08 (Lawrence & Shearer, 2008) but largely absent in other ray-theory based models constructed using SS

precursors (Houser et al., 2008; Gu et al., 2003) (Fig. 3.6). The most distinct difference between this study and LS08 is that positive anomalies at the 660-km discontinuity are much stronger in LS08 which also have a significantly different geographic distribution from this study. The finite-frequency sensitivities used to construct model LS08 were calculated based on ray tracing, which is computationally efficient but the sensitivity kernels do not account for phase interactions and windowing (tapering) applied in seismograms. In addition, stacking was applied to the waveforms of SS waves (and their precursors) as well as traveltime sensitivity kernels in Lawrence & Shearer (2008), which is not necessary a linear process.

3.7 Conclusions

The classic textbook anti-correlation between the 410-km and 660-km discontinuities is not observed in global subduction zones. While counter-intuitive, major subduction zones are characterized by strong positive correlations between the 410-km and 660-km discontinuity, with both discontinuities occurring at greater depths. Wavespeed and anisotropy models support vertical variations in thermal structure in the mid mantle. We interpret this circum-Pacific positive correlation as a result of cold, stagnant slab in the lower mantle transition zone and an overall warmer mid mantle due to return flows associated with the sinking of stagnant slabs into the lower mantle. Mass exchange between the upper and lower mantle occurs in the close proximity of the (sinking) stagnant slabs, mostly confined in the mantle transition zone and vicinity, forming a possibly semi-closed convection cell. This convection mode in the mid mantle is decoupled from surface plate movement as subduction in the upper mantle is mainly accommodated by horizontal movement of stagnant slabs.

We point out that the tradeoff between resolution and model uncertainty depends on noise levels in the measurements as well as the sensitivities of travel times to depth perturbations, which are different for S410S and S660S waves. Regularization parameters applied in inversion affect the amplitudes of the recovered depth perturbations, however, the polar-

ity (uplift or depression) is well resolved in both models. For example, the thinner mantle transition zone in oceanic regions is well constrained but the magnitude of thinning might have been underestimated. The same applies to the positive correlation between the two discontinuities beneath major subduction zones.

Bibliography

- Anderson, D. L., 1967. Phase changes in the upper mantle, *Science*, **157**, 1165–1173.
- Chang, S.-J., Ferreira, A. M. G., Ritsema, J., van Heijst, H. J., & Woodhouse, J. H., 2014. Global radially anisotropic mantle structure from multiple datasets: A review, current challenges, and outlook, *Tectonophysics*, **617**, 1–19.
- Christensen, U., 1995. Effects of phase transitions on mantle convection, *Review of Earth and Planetary Sciences*, **23**, 65–88.
- Deng, K. & Zhou, Y., 2015. Wave diffraction and resolution of mantle transition zone discontinuities in receiver function imaging, *Geophysical Journal International*, **201**, 2008–2025.
- Flanagan, M. P. & Shearer, P. M., 1998. Global mapping of topography on transition zone velocity discontinuities by stacking SS precursors, *Journal of Geophysical Research*, **103**, 2673–2692.
- Forsyth, D. & Uyeda, S., 1975. On the relative importance of the driving forces of plate motion, *Journal of Geophysical Research*, **43**, 163–200.
- Fukao, Y. Obayashi, M., 2013. Subducted slabs stagnant above, penetrating through, and trapped below the 660 km discontinuity, *Journal of Geophysical Research: Solid Earth*, **118**, 5920–5938.

- Gao, S. S. & Liu, K. H., 2014. Mantle transition zone discontinuities beneath the contiguous United States, *J. Geophys. Res.*, **119**, 6452–6468.
- Gu, Y. J., Dziewonski, A. M., & Ekström, G., 2003. Simultaneous inversion for mantle shear velocity and topography of transition zone discontinuities, *Geophysical Journal International*, **154**, 559–583.
- Hafkenscheid, E., Wortel, M. J. R., & Spakman, W., 2006. Subduction history of the tethyan region derived from seismic tomography and tectonic reconstructions, *Journal of Geophysical Research*, **111**, doi:10.1029/2005JB003791.
- Hall, R., 2012. Late jurassic-cenozoic reconstructions of the Indonesian region and the Indian Ocean, *Tectonophysics*, **570-571**, 1–41.
- Hall, R. & Spakman, W., 2015. Mantle structure and tectonic history of SE Asia, *Tectonophysics*, **658**, 14–45.
- Heit, B., Yuan, X., Bianchi, M., Kind, R., & Gossler, J., 2010. Study of the lithospheric and upper-mantle discontinuities beneath eastern Asia by SS precursors, *Geophysical Journal International*, **183**, 252–266.
- Houser, G., Masters, G., Flanagan, M., & Shearer, P., 2008. Determination and analysis of long-wavelength transition zone structure using SS precursors, *Geophysical Journal International*, **174**, 178–194.
- Kennett, B. L. N. & Engdahl, E. R., 1991. Traveltimes for global earthquake location and phase identification, *Geophysical Journal International*, **105**, 429–465.
- Kincaid, C. & Griffiths, R. W., 2003. Laboratory models of the thermal evolution of the mantle during rollback subduction, *Nature*, **425**, 58–62.
- Laske, G., Masters, G., Ma, Z., & Pasyanos, M., 2013. Update on CRUST1.0—a 1-degree global model of earth’s crust, *EGU General Assembly Conference Abstracts*, **15**, 2658.

- Lawrence, J. F. & Shearer, P. M., 2008. Imaging mantle transition zone thickness with SdS-SS finite-frequency sensitivity kernels, *Geophysical Journal International*, **174**, 143–158.
- Liu, K. & Zhou, Y., 2016. Travelling-wave green tensor and near-field rayleigh-wave sensitivity, *Geophysical Journal International*, **2015**, 134–145.
- Moulik, P. & Ekström, G., 2014. An anisotropic shear velocity model of the earth’s mantle using normal modes, body waves, surface waves and long-period waveforms, *Geophysical Journal International*, **199**, 1713–1738.
- Piromallo, C., Becker, T. W., Funicello, F., & Faccenna, C., 2006. Three-dimensional instantaneous mantle flow induced by subduction, *Geophysical Research Letters*, **33**, doi:10.1029/2005GL025390.
- Ringwood, A. E., 1969. Phase transformation in the mantle, *Earth and Planetary Science Letters*, **5**, 401–412.
- Ritsema, J., Deuss, A., van Heijst, H. J., & Woodhouse, J. H., 2011. S40RTS: a degree-40 shear-velocity model for the mantle from new rayleigh wave dispersion, teleseismic traveltimes and normal-mode splitting function measurements, *Geophysical Journal International*, **184**, 1223–1236.
- Sandwell, D. T. & Renkin, M., 1988. Compensation of swells and plateaus in the North Pacific: No direct evidence for mantle convection, *Journal of Geophysical Research*, **93**, 2775–2783.
- Schaeffer, A. J. & Lebedev, S., 2013. Global shear speed structure of the upper mantle and transition zone, *Geophysical Journal International*, **194**, 417–449.
- Schellart, W. P., 2008. Kinematics and flow patterns in deep mantle and upper mantle subduction models: Influence of the mantle depth and slab to mantle viscosity ratio, *Geochemistry, Geophysics, Geosystems*, **9**, doi:10.1029/2007GC001656.

- Schmerr, N. & Garnero, E., 2006. Investigation of upper mantle discontinuity structure beneath the central Pacific using SS precursors, *Journal of Geophysical Research*, **111**, doi:10.1029/2005JB004197.
- Seno, T. & Maruyama, S., 1984. Paleogeographic reconstruction and origin of the Philippine Sea, *Tectonophysics*, **102**, 53–84.
- Shearer, P. M., 1991. Constraints on upper mantle discontinuities from observations of long-period reflected and converted phases, *Journal of Geophysical Research*, **96**, 18147–18182.
- Shen, X., Zhou, H., & Kawakatsu, H., 2008. Mapping the upper mantle discontinuities beneath china with teleseismic receiver functions, *Earth Planets Space*, **60**, 713–719.
- Sigloch, K., McQuarrie, N., & Nolet, G., 2008. Two-stage subduction history under North America inferred from finite-frequency tomography, *Nature Geoscience*, **1**, 458–462.
- Smyth, J. R. & Jacobsen, S. D., 2006. Nominally anhydrous minerals and Earth’s deep water cycle, *Earth’s Deep Water Cycle*, **1**, 1–11.
- Tian, Y., Zhou, Y., Sigloch, K., Nolet, G., & Laske, G., 2011. Structure of North American mantle constrained by simultaneous inversion of multiple-frequency SH, SS and Love waves, *Journal of Geophysical Research*, **116**, doi:10.1029/2010JB007704.
- Wang, Y. & Pavlis, G. L., 2016. Roughness of the mantle transition zone discontinuities revealed by highresolution wavefield imaging, *Journal of Geophysical Research*, **121**, doi:10.1002/2016JB013205.
- Webb, S. C. & Forsyth, D. W., 1998. Structure of the upper mantle under the EPR from waveform inversion of regional events, *Nature*, **280**, 1227–1229.
- Wessel, P., Bercovici, D., & Kroenke, L., 1994. The possible reflection of mantle discontinuities in Pacific geoid and bathymetry, *Geophysical Research Letter*, **21**, 1943–1946.

Zhou, Y., 2009. Multi-mode 3-D surface-wave sensitivity kernels in radially anisotropic media, *Geophysical Journal International*, **176**, 865–888.

Zhou, Y., 2018. Anomalous mantle transition zone beneath the Yellowstone hotspot track, *Nature Geoscience*, **11**, 449–453.

Zhu, H., Komatitsch, D., & Tromp, J., 2017. Radial anisotropy of the North American upper mantle based on adjoint tomography with usarray, *Geophysical Journal International*, **211**, 349–377.

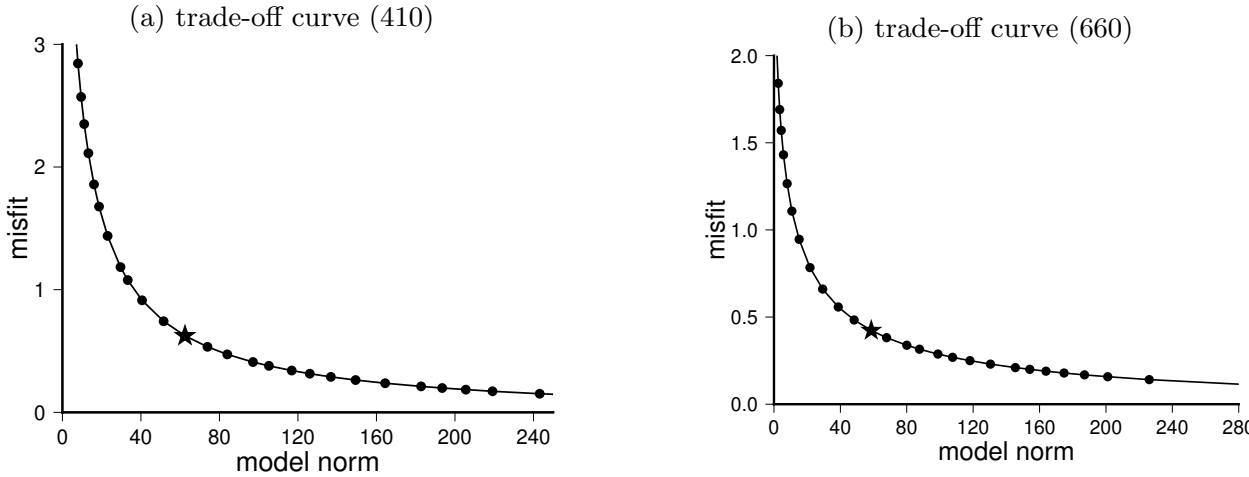


Figure 3.1: Tradeoff curves of the inverse problem $(\mathbf{G}^T \mathbf{G} \mathbf{m} - \mathbf{G}^T \mathbf{d}) + \alpha^2 \mathbf{m} = 0$ with a varying Tikhonov regularization parameter α . The horizontal axis is $\|\mathbf{m}\|$ and vertical axis is $\|\mathbf{G}^T \mathbf{G} \mathbf{m} - \mathbf{G}^T \mathbf{d}\|$. The optimal models plotted in Fig. 3.3 are indicated by stars.

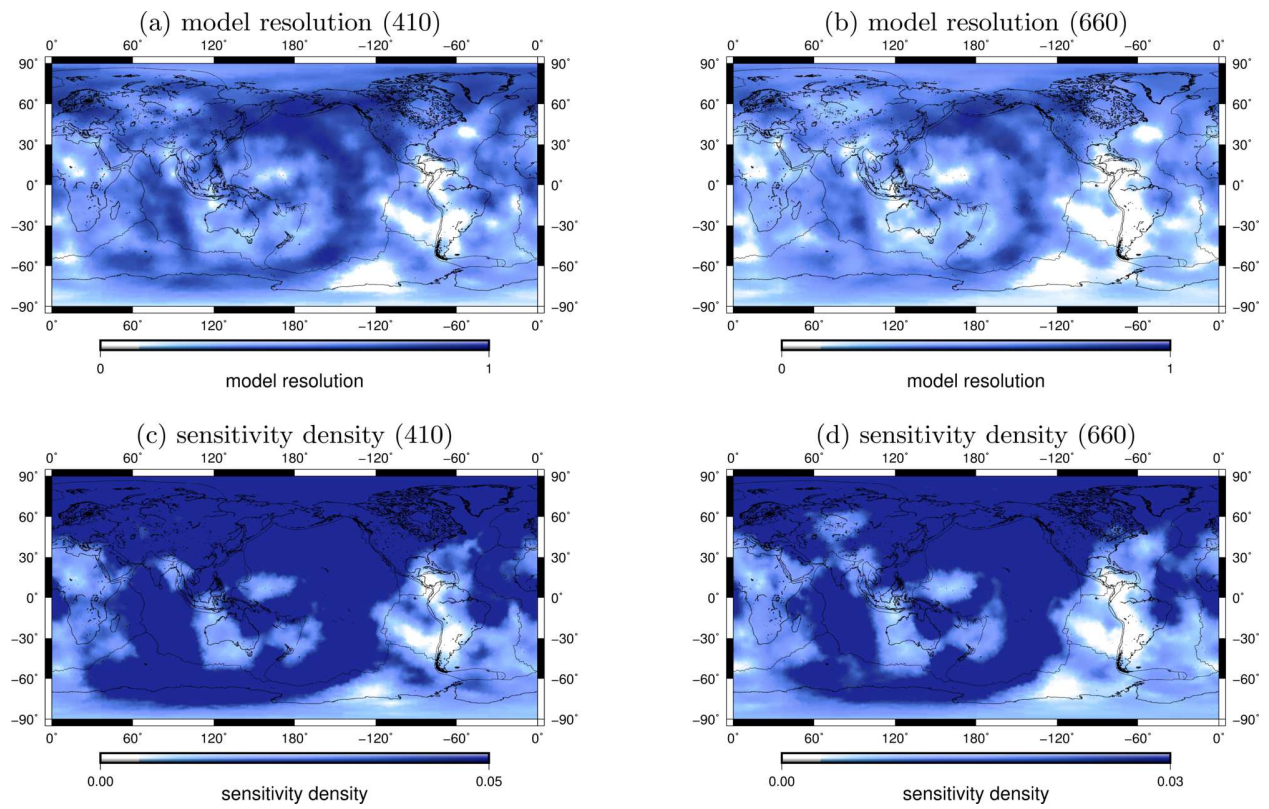


Figure 3.2: (a) and (b) are resolutions of the 410-km and 660-km discontinuity models in Fig. 3.3, plotted in every $4^\circ \times 4^\circ$ grid cell based on diagonal elements of the resolution matrix \mathbf{R} . (c) and (d) are the corresponding sensitivity density (diagonal elements of the matrix $\mathbf{G}^T \mathbf{G}$).

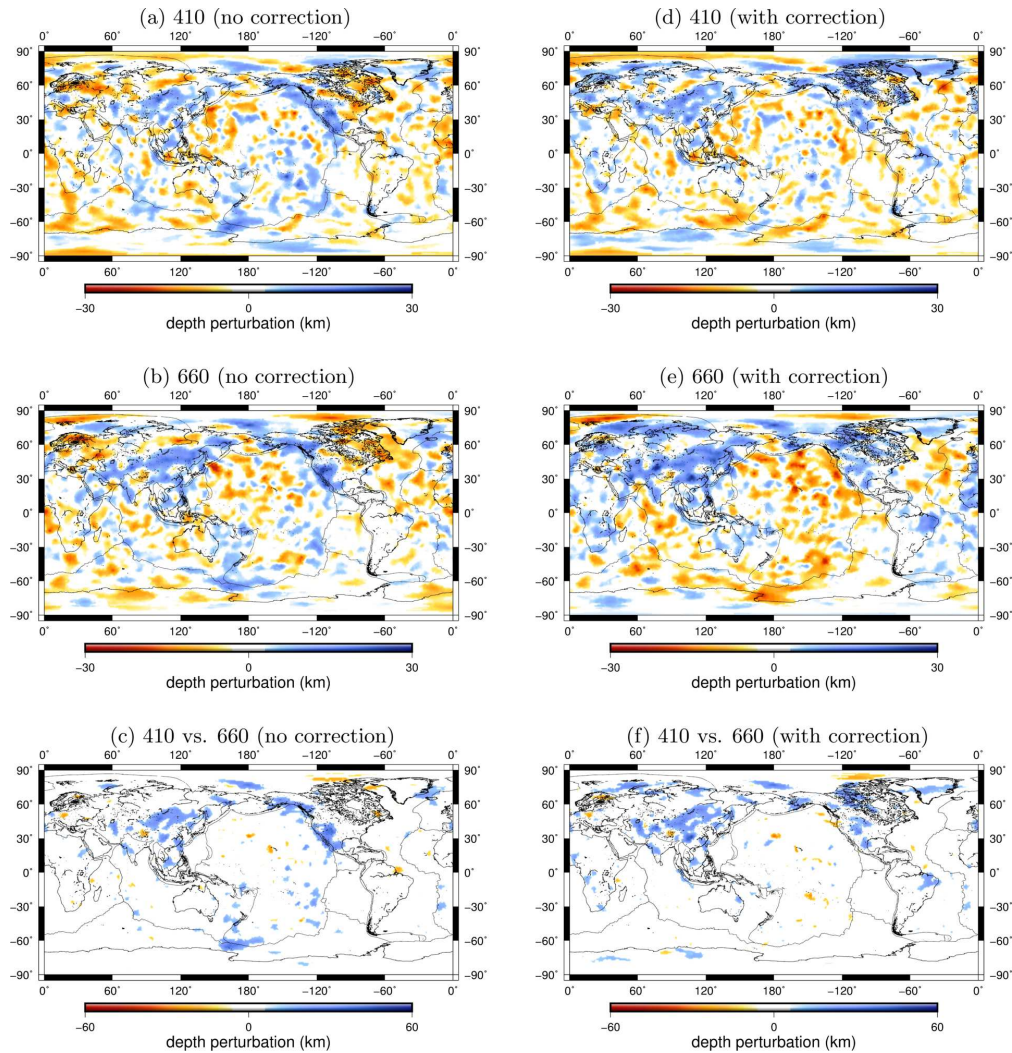


Figure 3.3: (a) and (b) are global depth perturbations of the 410-km and 660-km discontinuities imaged from finite-frequency tomography of S410S-SS and S660S-SS differential traveltimes measurements. (c) correlation between the 410-km and 660-km discontinuity depth perturbations represented by the sum of the absolute perturbations at the two discontinuities. The correlation is positive (in blue) in regions where both the 410-km and 660-km discontinuities occur at depths greater than the global average; and is negative (in red) in region where the 410-km discontinuity is deeper while the 660-km discontinuity is shallower (typical anti-correlation signature for mantle plumes). Only regions with both discontinuity depth perturbations larger than uncertainties (5 km) are plotted. (d)–(f) are the same as (a)–(c) but models obtained using traveltimes measurements corrected for 3-D seismic structure in the crust (CRUST1.0) as well as wavespeed variations in the mantle (S40RTS).

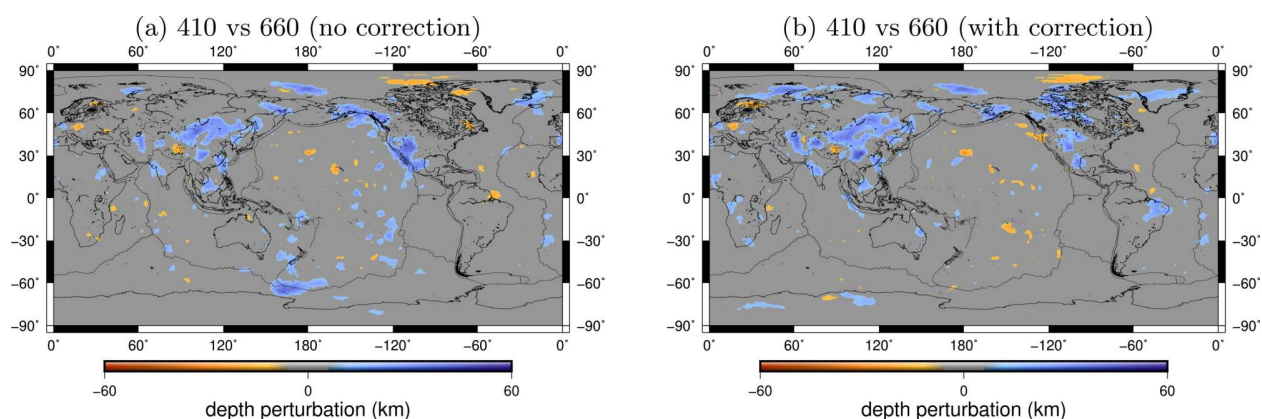


Figure 3.4: **Circum-Pacific positive correlation between the 410 and the 660.** (a) correlation between the 410 and the 660 depth perturbations represented by the sum of their absolute perturbations. The correlation is positive (in blue) in regions where both discontinuities occur at depths greater than the global average; and is negative (in red) in region where the 410 is deeper while the 660 is shallower (typical anti-correlation signature for mantle plumes). Only regions with both perturbations larger than uncertainties (5 km) are plotted. (b) the same as (a) but obtained using traveltimes corrected for 3-D wavespeed structure in the crust (CRUST1.0) and mantle (S40RTS).

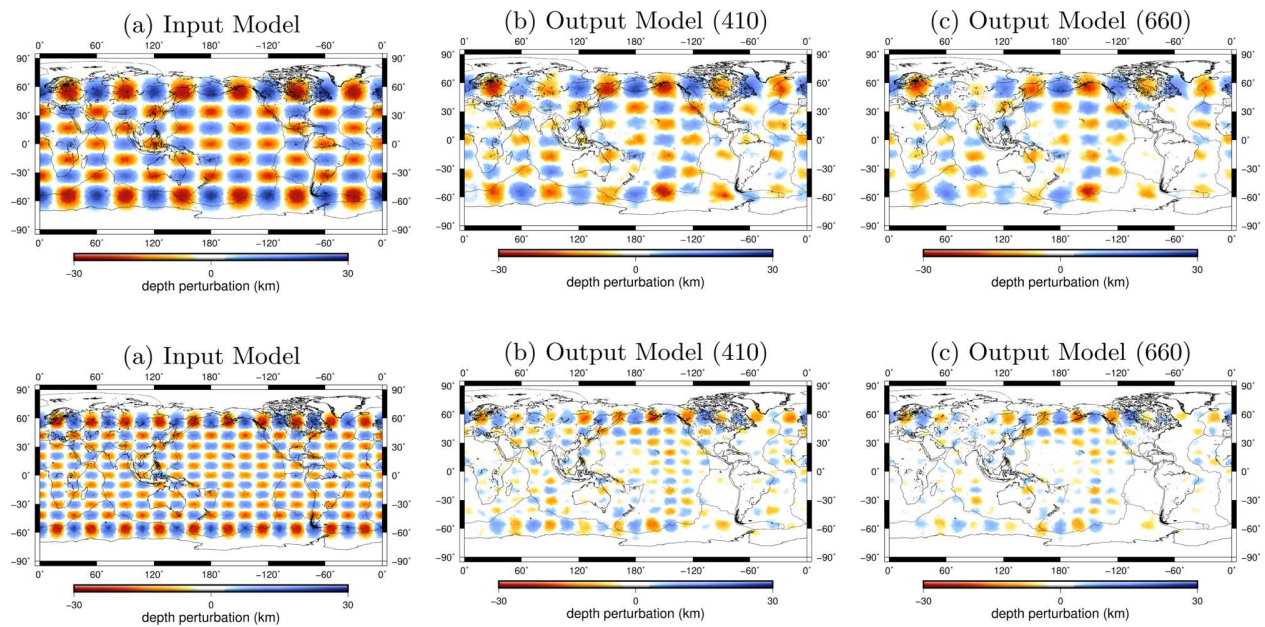


Figure 3.5: Tomographic resolution tests for the 410-km and 660-km discontinuity models in Fig. 3.3. The input models have a spherical harmonic structure, with degree $l = 12$ (top) and $l = 20$ (bottom), respectively. We generate synthetic data using the input models and finite-frequency sensitivity kernels for the same earthquake-station configuration, and the output models are obtained with the same inversion regularization parameters as used for the real data. We have added 20% of random noise in all synthetic data in the resolution tests.

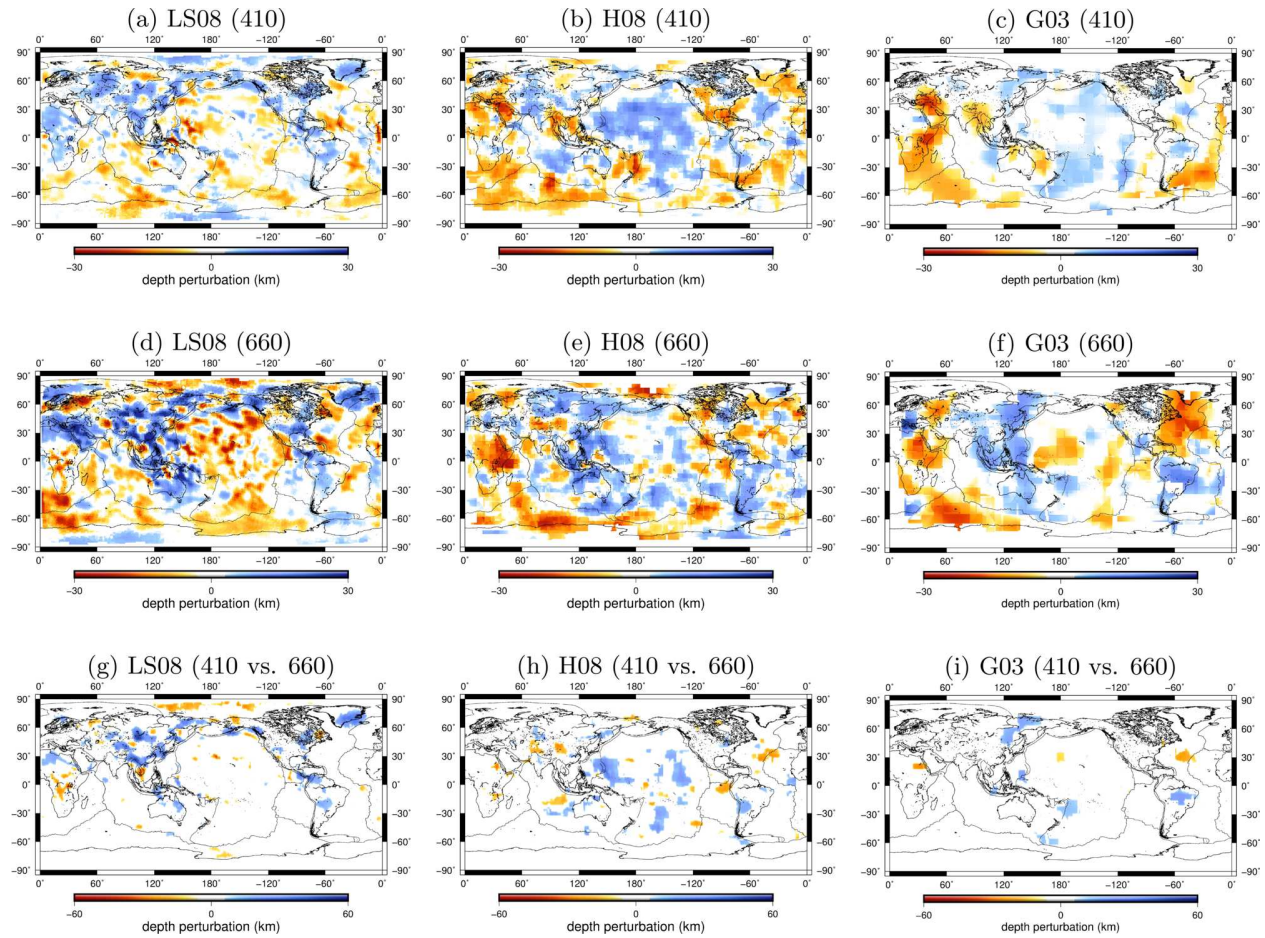


Figure 3.6: (a)–(f) are global models of the 410 km and 660-km discontinuities LS08 (Lawrence & Shearer, 2008), H08 (Houser et al., 2008) and G03 (Gu et al., 2003). (g)–(i) are correlations maps calculated as in Fig. 3.4.

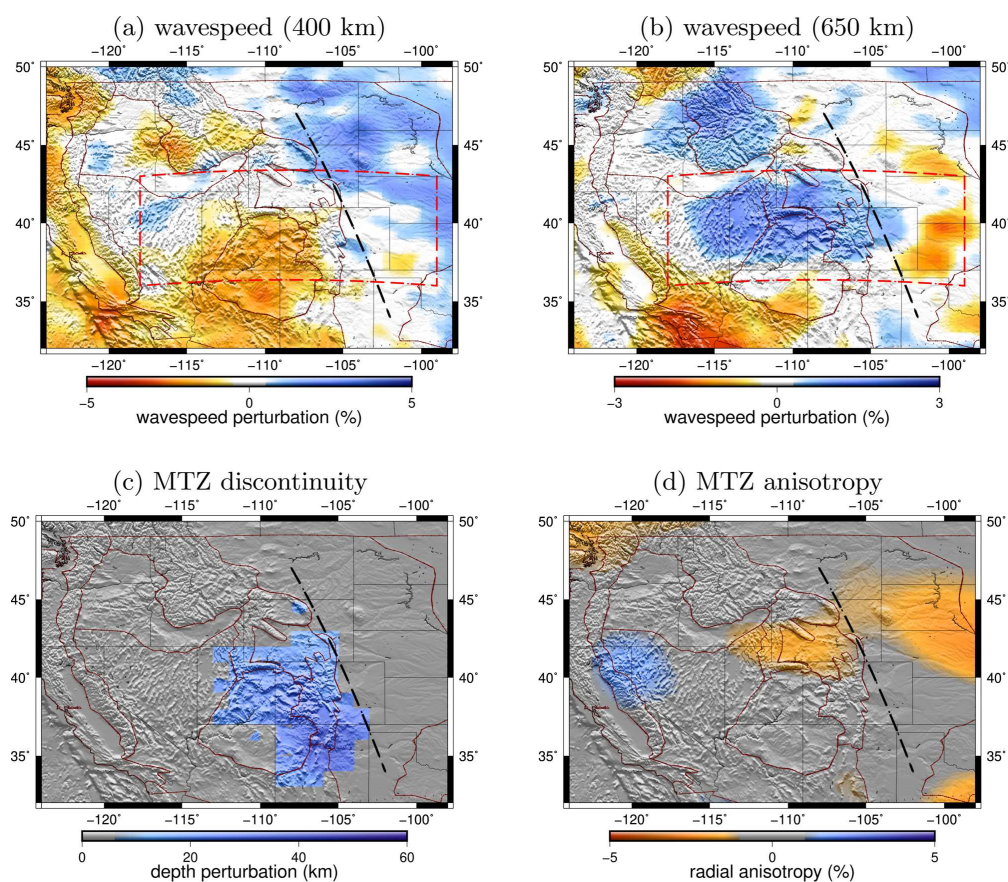


Figure 3.7: **Warm mantle above stagnant slab in the Western US.** (a) and (b) are S-wave velocity perturbations at depths of 400 km and 650 km, respectively (Tian et al., 2011). (c) correlation between the 410 and the 660 in the Western US, only regions with consistent anomalies in Fig. 3.4(a) and (b) are plotted. (d) average radial anisotropy in the MTZ in model US22 (Zhu et al., 2017) where negative ($V_{SH} < V_{SV}$) radial anisotropy indicates dominant vertical mantle flow. Dark red lines are major geological boundaries; black dashed line indicates subduction front in the MTZ. 3-D wavespeed model in the red box red in (a) and (b) is plotted in Fig. 3.8.

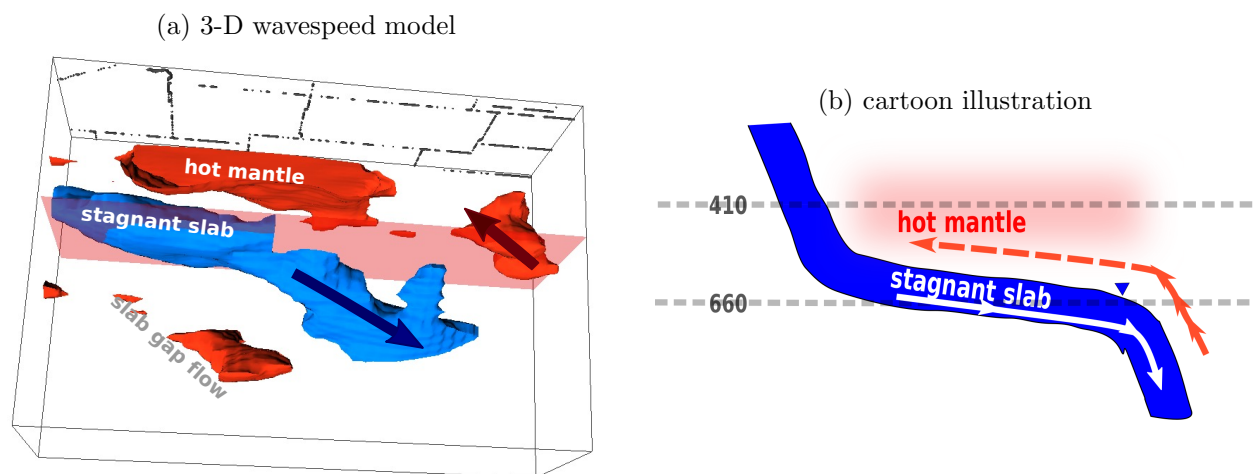


Figure 3.8: **3-D wavespeed structure in the Western US and Cartoon illustration of subduction with stagnant slab** (a) 3-D rendering of S-wave slab anomalies in the Western US. The isosurface represents 1% fast and slow seismic wavespeed anomalies at depths from 50 km to 1600 km US State boundaries are plotted at the surface for geographic reference. Fast anomalies in the upper mantle beneath the craton have been removed for better illustration of the slab. (b) Cartoon (not to scale) illustrating the sinking of a stagnant slab from the mantle transition zone into the lower mantle. The blue triangle indicates the *trench* in the MTZ. The 660-km discontinuity occurs deeper (not illustrated) due to the cold stagnant slab in the lower MTZ and the 410-km discontinuity also occurs at greater depths (not illustrated) due to warm return flows in a super adiabatic mantle and possible *trench retreat* in the MTZ.

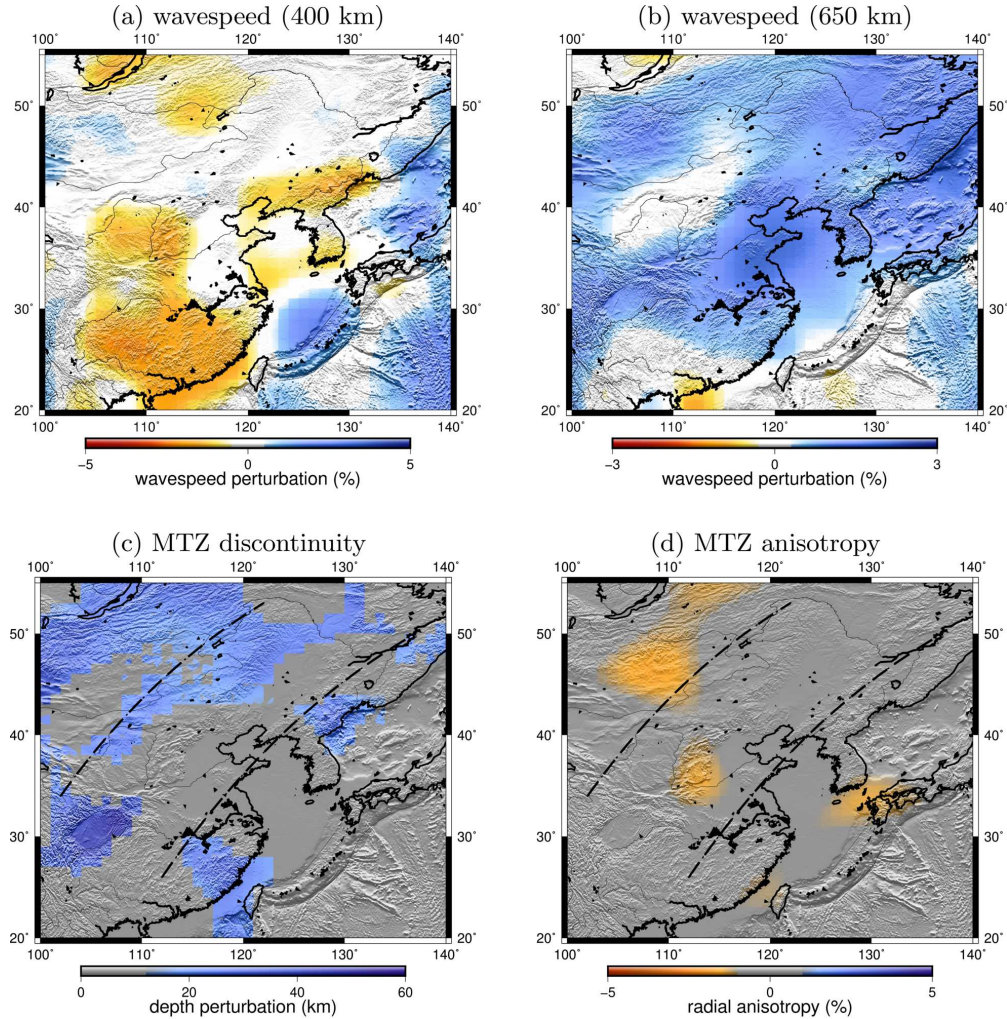


Figure 3.9: **Warm mantle above stagnant slab in Eastern Asia.** (a) and (b) are S-wave velocity perturbations at depths of 400 km and 650 km from Schaeffer and Lebedev (2013). (c) correlation between the 410 and the 660 in Eastern Asia, only regions with consistent anomalies in Fig. 3.4 (a) and (b) are plotted. (d) average radial anisotropy in the MTZ in model SGLOBE-rani (Chang et al., 2014), where negative radial anisotropy ($V_{SH} < V_{SV}$) indicates dominant vertical mantle flow. Two dashed lines indicate subduction systems in the MTZ, roughly parallel to the present-day Ryukyu trench.

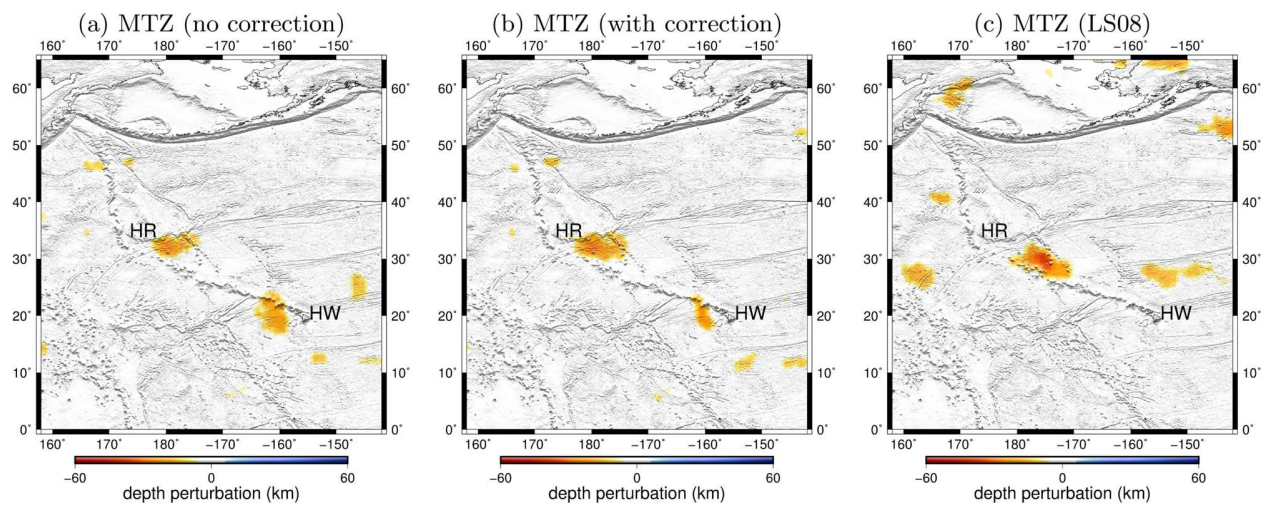


Figure 3.10: **The Hess Rise (HR) anomaly.** (a) and (b) are correlations between the 410-km and 660-km discontinuity depth perturbations in the Pacific (same as Fig. 3.4a and b); (c) the same correlation calculated using discontinuity models published by Lawrence and Shearer (2008). The anomaly west of the island of Hawaii (HW) becomes much weaker after wave speed corrections. The *plume-like* structure south of Hess Rise (HR) is a consistent feature in all three models.

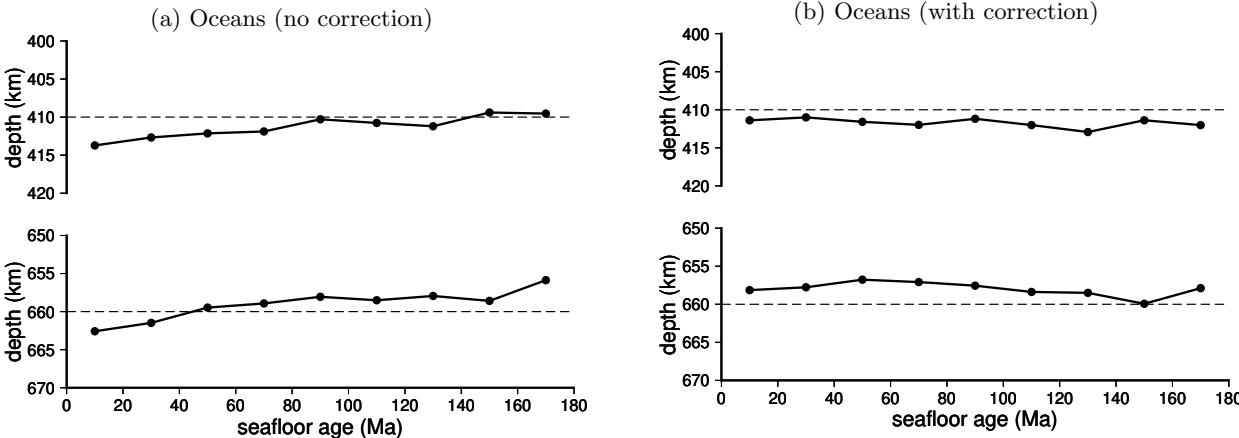


Figure 3.11: **The 410 and the 660 in oceanic regions.** (a) depth perturbations of the 410 and the 660 in global oceanic regions, averaged over every 20-million year age band; (b) the same as (a) but for models inverted using traveltimes corrected using model CRUST1.0 and S40RTS

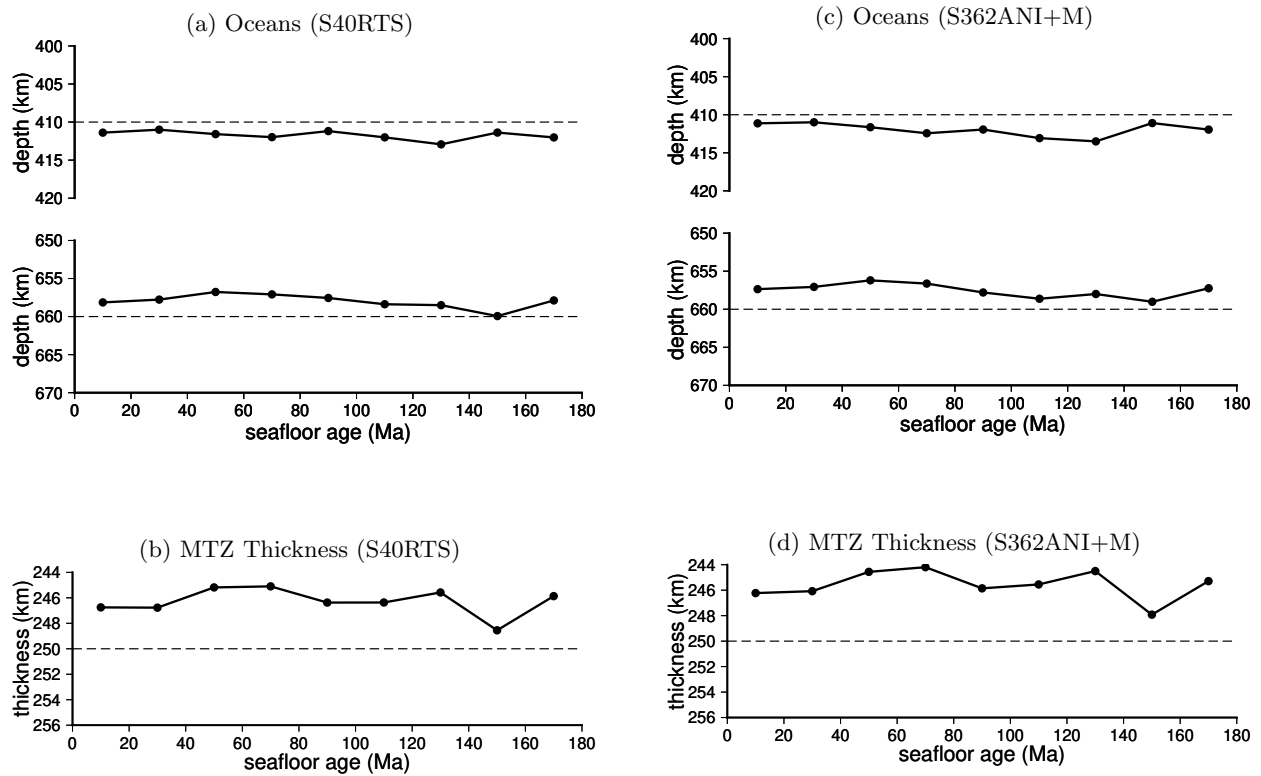


Figure 3.12: (a) depth perturbations of the 410-km and 660-km discontinuities in global oceanic regions, averaged over every 20-million year age band in models inverted using traveltime data corrected for 3-D crust and mantle wavespeed structures (S40RTS). (b) thickness of the MTZ as a function of seafloor age in global oceanic regions. (c) and (d) are the same as (a) and (b) but for models inverted with traveltime measurements corrected using model S362ANI+M.

Chapter 4

Using Spectral Ratios to Examine Amplification and Attenuation Effects in the Atlantic and Gulf Coastal Plain

(An edited version of this chapter has been accepted in The Bulletin of the Seismological Society of America (BSSA).)

4.1 Introduction

We explored some of the differences in ground motion propagation for sites located within, versus outside, the Atlantic and Gulf Coastal Plain. Currently, ground motion prediction models are lacking for the Coastal Plain regions of the central and eastern United States. This study was a first step toward developing such a model. We found that the Coastal Plain sediments amplify low-frequency ground motions and attenuate high-frequency ground

motions relative to sites outside the Coastal Plain. This has important implications for seismic hazard assessment.

Until recently, the relatively low levels of seismic activity and a lack of long-term operating seismic stations outside the New Madrid seismic zone have limited wave propagation studies in most parts of the Atlantic and Gulf Coastal Plain. Previous studies documented high-frequency attenuation in the Gulf Coastal Plain. Gupta et al. (1989) found lower Lg Q in the Gulf region than elsewhere in eastern North America. The operation of the Earthscope USArray Transportable Array (TA network) in the central United States during 2010-2012 when a series of moderate earthquakes occurred in Oklahoma, Arkansas and Texas resulted in an important data set. More recently, a few earthquakes have been recorded in the Atlantic Coastal Plain by the currently operational Central and Eastern United States Network (N4 network), the United States National Seismic Network (US network) and some other stations, including temporary array deployments. Pasyanos (2013), using Q tomography, found lower Q for crustal S waves in the Gulf coastal region than in regions to the north.

Chapman & Conn (2016) observed geographic variation of the attenuation parameter kappa, κ (Anderson & Hough, 1984) in the Gulf Coastal Plain, noting a clear positive correlation of κ and the thickness of post-Jurassic sediments in the region. Incorporating a thickness-dependent Lg kappa model in stochastic ground motion simulations resulted in improved high-frequency ground motion prediction (Chapman & Conn, 2016). Figure 10 of Chapman & Conn (2016) shows that the area with largest kappa (and thickest Coastal Plain sediment) largely corresponds with the low Q Gulf Coastal Plain area resolved by Cramer (2018) using USArray (TA network) data. It also corresponds with the area that has experienced continental crustal thinning (Salvador, 1991a; Sawyer et al., 1991; Thomas, 2010). Lg propagation is known to be sensitive to changes in crustal structure (Kennett, 1986). Both Lg blockage due to crustal thinning, and absorption due to the increase in thickness of sediments may operate to increase attenuation in parts of the Gulf Coastal Plain.

Chapman & Conn (2016) jointly estimated shear wave crustal Q associated with distance dependent attenuation and site terms for Lg wave Fourier amplitude spectra. They used the site terms to estimate κ in the Gulf Region. They found $Q = 365f^{0.62}$, where f is frequency in Hz. Chapman and Conn concluded that the bulk of the attenuation in the Gulf Coastal Plain is not strongly related to crustal waveguide Q , but instead is dominated by near-receiver attenuation reflected by κ values that are correlated with local sediment thickness. Recently, Cramer (2018) estimated $Q = 259f^{0.72}$ for the Gulf coastal region. Relative to the results of Chapman & Conn (2016) and Cramer (2018), representative estimates of Q outside the Coastal Plain in eastern North America show higher values at 1 Hz by a factor of approximately 1.4 – 2.0, but significantly less frequency dependence. For example, Atkinson & Boore (2014) found $Q = 525f^{0.45}$ for rock sites in eastern North America. These models predict lower Q in the Coastal Plain at frequencies less than approximately 8-14 Hz, but higher Q at higher frequencies. Purely on the basis of these crustal Q estimates, one might expect lower amplitudes in the Gulf at low frequencies, and similar or larger amplitudes at frequencies of approximately 12 Hz, relative to the average of sites outside the Coastal Plain. In this study we observed that Coastal Plain sites exhibit smaller high frequency amplitudes and larger low-frequency amplitudes than average site conditions outside the Coastal Plain. The origin of the strong frequency dependence of the reported estimates of crustal $Q(f)$ for the Gulf Coastal Plain may represent complex trade-offs between site terms, source terms and distance dependent attenuation parameters in the regression models used to invert for crustal Q . It is our view that ground motion prediction models for Coastal Plain sites will require information in addition to the estimated value of Q for the crustal waveguide. The higher frequency (greater than 1 or 2 Hz) attenuation as well as the amplitude and frequency range of low frequency amplification we observe in the Coastal Plain is geographically variable and is dependent on the thickness of sediments (Chapman & Conn, 2016).

The motivation for this study was simple. We attempted to quantify, in a straightforward way, the relative difference between site response in the Coastal Plain (Atlantic and Gulf) and the region outside the Coastal Plain in terms of the Fourier amplitude spectra. We

focused on spectral ratios because we wanted to establish a basis for modifying existing or future ground motion prediction models established for rock-like conditions for application in the Coastal Plain. The existing ground motion prediction models are to a large degree founded on results derived from the stochastic method of ground motion simulation, and our approach here is amenable to the development of target spectra for stochastic simulation.

We expanded the dataset used by Chapman & Conn (2016) by adding broadband stations in addition to the TA network and data from a few more recent earthquakes including some occurring in the Appalachian region. Selecting reference sites is an important step in the spectral ratio method (Borcherdt, 1970). Our study is handicapped by a lack of information on shallow geologic conditions and near-surface velocity at the great majority of recording locations. Most of the stations outside the Coastal Plain are not sited on hard rock outcrop, but instead have site conditions ranging from thin residual soil over hard crystalline rock (many sites in the Appalachian Piedmont), to sites on thick sequences of Paleozoic sedimentary rock (e.g., stations in the Appalachian Valley and Ridge, and many stations in the mid-continent area). We used mean coda and Lg spectra derived from large numbers of stations outside the Coastal Plain as the reference condition. This approach is simple, but it lacks rigor and introduces some ambiguity.

Most of our data are from recent (post-2009) shocks occurring outside the Coastal Plain region. However, we find evidence that shocks occurring within the Coastal Plain produce motions outside the Coastal Plain that have reduced amplitudes at high frequency, an observation that suggests that Lg waves experience appreciable high-frequency attenuation near the source if in the Coastal Plain.

Geologic Background

The Atlantic and Gulf Coastal Plain in the eastern, southeastern and southern United States (Figure 4.1) is characterized by a series of sedimentary formations ranging in age from Early Cretaceous to Holocene (Salvador, 1991a; Thomas et al., 1989; Thomas, 1989). In the southeast and Mid-Atlantic region of the U.S., the Paleozoic rocks of the exposed

Appalachian orogen include the sedimentary rocks of the fold-thrust belt (Valley and Ridge province) and metamorphic belts (Blue Ridge and Piedmont provinces) which locally contain Precambrian basement rocks. These rocks can be traced beneath the post-orogenic Atlantic Coastal Plain sediments. Early Mesozoic volcanic and sedimentary rocks are found in several extensional basins throughout the Piedmont and also beneath the Coastal Plain. Those basins were the result of rifting associated with the opening of the Atlantic Ocean. The landward limit of the Atlantic Coastal Plain sedimentary units approximately parallels the northeasterly structural strike of the orogen, and lies within the Piedmont province. This northwestern limit of Atlantic Coastal Plain sediments in the Piedmont is known as the Fall Line. Over most of the region from southern Georgia to New Jersey the Atlantic Coastal Plain sediments form a generally seaward thickening wedge with maximum thickness less than 3 km. Marine Coastal Plain sediments in parts of western Florida, southern Georgia, and southern South Carolina are unconformably underlain by Triassic and early Jurassic volcanic and sedimentary rocks of the South Georgia Basin (McBride et al., 1989; McBride, 1991), one of the larger buried Mesozoic extensional basins in the Appalachian orogen. Paleozoic rocks beneath the Coastal Plain sediments of southern Alabama, Georgia and Florida differ from those in the Appalachian Piedmont and are referred to as the Suwannee terrane. The boundary between the different terranes has been interpreted as a major Alleghanian collision zone, named the Suwannee-Wiggins suture (McBride & Nelson, 1988; Thomas et al., 1989; Parker et al., 2013). In Alabama, the landward limit of Gulf Coastal Plain sediments changes trend to the west and northwest, oblique to the strike of Appalachian Paleozoic sedimentary rocks buried beneath the sediments. The sediments dip toward the Gulf of Mexico, forming a wedge that thickens toward the coast. Further to the northwest, in the Mississippi Embayment of the Gulf Coastal Plain, the sediments cross and bury rocks of the Paleozoic Appalachian-Ouachita orogenic belt and portions of interior cratonic arches (Thomas et al., 1989; Thomas, 1989).

The Gulf of Mexico is a roughly circular basin, with the center containing approximately 15 km of Triassic to Holocene sedimentary rocks (Salvador, 1991a). The basement rocks

beneath the Gulf Coastal Plain sediments were involved in the Mesozoic tectonic development of the Gulf of Mexico (Sawyer et al., 1991). Whereas the offshore central part of the Gulf of Mexico is underlain by oceanic crust, the onshore Gulf Coastal Plain in the southern U.S. is underlain largely by transitional continental crust that has experienced Early Mesozoic extension and post-Jurassic sediment accumulation (Salvador, 1991a; Sawyer et al., 1991; Galloway, 2008). The area of transition between thick North American crust and oceanic crust coincides with a thickening of post-Jurassic sediments. Near the coasts of Texas, Louisiana and Mississippi, the sediments reach a thickness in excess of 10 km (Salvador, 1991b; Sawyer et al., 1991; Galloway, 2008; Chapman & Conn, 2016). The great thickness of sediments in the Gulf Coastal Plain of Texas, Louisiana and Mississippi distinguishes that area from the Atlantic Coastal Plain. The sediment thickness is greatest along the axis of the Mississippi embayment.

The Coastal Plain sediments have varying degrees of consolidation and overlie a high-velocity basement. These conditions have significant effects on earthquake ground motions. An examination of Modified Mercalli Intensity reported for the 1886 Charleston, South Carolina earthquake combined with ground motion modeling by Chapman et al. (1990) found evidence for significant wave propagation effects due to the Atlantic Coastal Plain sediments. The modeling suggested that thicker sediments (approximately 1km) near the South Carolina coast amplified lower frequencies (less than approximately 1 Hz) but may have significantly attenuated higher frequency motion, whereas near the Fall Line an increase of intensities appears to be the result of high-frequency (greater than 1 Hz) amplification due to the relatively thin sediments. This is consistent with observations of amplification in the 0.7 to 4 Hz frequency range for Coastal Plain sites in the Washington, DC area, based on seismic data from a temporary seismic network deployment (Pratt et al., 2017).

4.2 Data and Analysis

Figure 4.2 shows the locations of the 17 earthquakes used in this study, with the hypocenter locations, dates, moment magnitudes and depths (derived by Robert Herrmann) of the earthquakes listed in Table 4.1. Twelve of these earthquakes were located in Oklahoma, Arkansas and Texas, with five occurring in the Appalachian region. The stations that provided seismic data include the USArray (TA) stations, United States National Seismic Network (US) stations, Central and Eastern US Network (N4) stations, the Lamont-Doherty Cooperative Seismographic Network (LD) stations and the Southeastern Suture of the Appalachian Margin Experiment (SESAME; Z9 network). The stations are plotted in Figure 1 with different symbols to distinguish the networks. Most of the TA stations were deployed in the study region during 2010-2012 and each operated for about 2 years. The Z9 network operated between 2010 and 2014 as three profiles extending from Georgia to northern Florida (Parker et al., 2013). The N4 network stations are a subset of the TA network and currently remain operational. Table 4.2 lists instrument type, sample rates and number of stations for the various networks.

Broadband seismograms recorded within 1000 km of the earthquakes in Table 4.1 were downloaded from the Incorporated Research Institutions for Seismology (IRIS) Data Management Center. Each seismogram begins 600 seconds prior to the earthquake origin time and lasts for 3600 seconds. We converted the recordings to ground acceleration using the instrument transfer functions, applied a high-pass filter with corner frequency 0.01 Hz, and rotated the horizontal components to radial and transverse directions.

Further data processing involved computing the Fourier amplitude spectra of coda and Lg waves, which required determination of coda and Lg time windows. Coda waves are scattered waves that have taken a variety of paths between source and receiver. The coda spectra are insensitive to the source radiation pattern, rupture complexities and hypocentral distance at sufficiently large lapse time (Frankel et al., 1990; Frankel, 2015; Wu et al., 2016). For each individual earthquake, we defined the beginning of a common coda window at lapse

time $T_0 + 1.5T_s$, where T_0 is the origin time and T_s is the S-wave travel time to the most distant station chosen for analysis. The choice of the largest hypocentral distance used for analysis was a compromise between the size of the dataset and the signal-to-noise levels of the distant recordings. The entire coda window length was chosen to be 20 s for all earthquakes. The Lg arrival time as a function of hypocentral distance r (km) is

$$T_{Lg} = T_0 + \frac{r}{3.53}. \quad (4.1)$$

This model was developed by Chapman & Conn (2016) using data from the 28 February 2011 Arkansas earthquake, which is also included in our dataset. The following equation was used to define the duration of the Lg window t_d ,

$$\int_{T_{Lg}}^{T_{Lg}+t_d} a^2 dt = 0.7 \int_{T_{Lg}}^{T_{Lg}+800} a^2 dt, \quad (4.2)$$

where a is the ground acceleration. The window contains the maximum amplitudes of the Lg waves.

We applied a cosine taper to the initial and final 15 Noise spectra were computed simultaneously using tapered windows starting at the beginning of the seismograms with the same durations as the corresponding coda and Lg windows. Then the geometric mean of the two horizontal-component spectra was calculated for subsequent analysis. We carefully selected seismograms with good signal-to-noise ratios over relatively wide frequency bands by visual inspection. Traces with strong modulations in the spectra were discarded. Only Fourier spectral amplitudes within frequency bands where the signal-to-noise ratio is larger than five were used for analysis, to minimize the effects of noise. Table 4.3 lists the total number of recordings, number of recordings in the Coastal Plain, as well as the distance range for each earthquake in the final dataset. Table 4.7 lists the station name, location and depth to basement, (i.e., sediment thickness) for stations in the Coastal Plain. Most of the sediment thickness values beneath stations in the Gulf Coastal Plain are adapted from Chapman & Conn (2016), which were determined from Salvador (1991b). Sediment thickness at stations further to the east in the Appalachian region were estimated from depth-to-basement con-

tour maps by Herrick & Vorhis (1963); Wait & Davis (1986); Salvador (1991b); Lawrence & Hoffman (1993) and Powars et al. (2015).

Some examples of the data are shown in Figure 4.3 which shows radial and transverse acceleration seismograms from the 06 November 2011 Prague, Oklahoma earthquake, recorded at station N35A and station 440A at similar distances of ~ 590 km. Station N35A is in eastern Nebraska and is underlain by residual soils and weathered Paleozoic sedimentary rocks, while station 440A in the Gulf Coastal Plain is located on ~ 8 km of Mesozoic and Cenozoic sediments. The acceleration amplitudes at station 440A are smaller compared to station N35A. Comparison of the corresponding coda and Lg Fourier spectra in Figure 4.3 shows that ground motions recorded at Coastal Plain station 440A are larger at low frequencies (< 0.6 Hz) and smaller at high frequencies (> 1 Hz) relative to station N35A. Acceleration recordings and Fourier amplitude spectra at Coastal Plain stations from the 15 Feb 2014 South Carolina earthquake and the 13 Oct 2010 Oklahoma earthquake exhibit similar behavior relative to sites outside the Coastal Plain (Figure 4.3).

Coda Analysis

According to the single-scattering model for coda waves proposed by Aki & Chouet (1975), the spectral amplitude $Y_{ij}^c(f, t)$ of coda waves recorded at the j th station in the Coastal Plain at some lapse time t after the origin time of the i th earthquake can be expressed as

$$Y_{ij}^c(f, t) = S_i(f)G_j^c(f)E(f, t), \quad (4.3)$$

where $S_i(f)$ is the source spectrum and $G_j^c(f)$ represents the site response for coda waves at the j th station, $j=1,2,3..n$. $E(f, t)$ combines the coda scattering intensity and subsequent decay of the coda as a function of frequency and lapse time, which is assumed independent of source and station when the lapse time t is larger than ~ 1.5 -2 times the S wave arrival time (Frankel, 2015; Wu & Chapman, 2017). Our major assumption is that $E(f, t)$ is a property of the crust, shared by all earthquakes and stations, both within and outside of the Coastal Plain. This requires that the crustal waveguide be at least approximately the same

for the region encompassing all the earthquakes and stations. As noted in the Introduction Section, previous studies of crustal Q have reported regional differences in the central and eastern United States, most significantly between the Gulf Coastal Plain on the one hand, and the Cratonic Platform - Appalachian region (outside the Atlantic Coastal Plain) on the other. Our hypothesis here (that we test using residual analysis) is that the lower Q values reported for the Gulf Coastal region at frequencies below approximately 10 Hz are due, at least in part, to trade-offs in the regression models between distance dependent crustal attenuation (parameterized by a frequency-dependent quality factor Q) and strong geographically variable local attenuation, which can be parameterized by κ_0 and is reflected in the site terms of the regression models. We recognize that differences in crustal structure (e.g., crustal thickness) exist throughout the central and eastern United States. We assume that differences between the response of stations at a fixed lapse time for a given earthquake are due to path differences arising near the receiver station (i.e., site response), and involve $G_j^c(f)$, in the case of stations in the Coastal Plain, as well as site response at stations outside the Coastal Plain.

We distinguish the coda spectral amplitude at the k th station outside the Coastal Plain, at lapse time t for the i th earthquake, as

$$\hat{Y}_{ik}^c(f, t) = S_i(f)\hat{G}_k^c(f)E(f, t), \quad (4.4)$$

where $\hat{G}_k^c(f)$ represents the site response of a station outside the Coastal Plain.

Our approach is to define a reference spectrum for each earthquake, based on the coda spectra at a fixed lapse time and recorded by stations outside the Coastal Plain. Site conditions outside the Coastal Plain, like conditions within it, are variable. Many non-Coastal Plain sites are on soil and alluvium, overlying weathered rock. The conditions may result in modulated amplification of the Fourier amplitude spectra at frequencies that depend on the thickness and velocity of the near-surface materials. These site response effects are contained in the $\hat{G}_k^c(f)$ term for the k th station. Visual inspection of all these spectra indicates that in most cases the modulations (if present) occur at frequencies greater than

1-3 Hz. Spectra exhibiting strong peaks were discarded. Stacking (averaging) the remaining spectra from different stations recording the same earthquake for a fixed lapse time reduces the amplitude of the modulations in the mean and the result is a “smooth” spectrum, given a sufficient number of individual spectra. Our reference spectrum for the i th earthquake is the mean of the coda spectra from the stations located outside the Coastal Plain,

$$\bar{Y}_i^c(f, t) = \frac{1}{m} \sum_{k=1}^m S_i(f) \hat{G}_k^c(f) E(f, t) = \frac{S_i(f) E(f, t)}{m} \sum_{k=1}^m \hat{G}_k^c(f), \quad (4.5)$$

where m is the number of stations involved in calculating the mean reference spectrum.

The coda spectral ratio for the j th station recording the i th earthquake is obtained by dividing equation (4.3) by the reference spectrum given by equation (4.5),

$$R_j^c(f) = \frac{Y_{ij}^c(f, t)}{\bar{Y}_i^c(f, t)} = \frac{G_j^c(f)}{\frac{1}{m} \sum_{k=1}^m \hat{G}_k^c(f)}. \quad (4.6)$$

In equation (4.6), taking the ratio of the coda spectrum at the Coastal Plain station to the reference spectrum removes the source and path effects by cancellation. The result represents the response effects of the Coastal Plain site relative to the reference condition. The reference condition is the mean site response of all stations outside the Coastal Plain recording the i th earthquake.

At high frequencies, the site response term for the j th Coastal Plain recording, which represents the numerator term in equation (4.6), exhibits exponential decay with frequency that we model as

$$G_j^c(f) = A_j \exp(-\pi k_j f), \quad (4.7)$$

where A_j is a constant. Here, k_j (kappa) is analogous to κ_0 of Anderson & Hough (1984). It is a site-specific parameter that accounts for the near-receiver attenuation effects and describes the spectral decay at high frequencies (Anderson & Hough, 1984; Atkinson & Boore, 2014). Likewise, we model the denominator term in equation (4.6) (the reference spectrum) at high frequencies as

$$\frac{1}{m} \sum_{k=1}^m \hat{G}_k^c(f) = \bar{A}_r \exp(-\pi \bar{k}_r f), \quad (4.8)$$

where \bar{k}_r represents the "average" kappa for the reference condition.

Substituting equations (4.7) and (4.8) into equation (4.6) leads to the following model for the logarithm of the coda spectral ratio at high frequencies

$$\ln(R_j^c) = \ln\left(\frac{A_j}{A_r}\right) - \pi(k_j - \bar{k}_r)f = C_j - \pi(\delta k_j)f, \quad (4.9)$$

where C_j is a constant and $\delta k_j = (k_j - \bar{k}_r)$ is the difference between the kappa value (k_j) at the j th Coastal Plain station and the average kappa (\bar{k}_r) at the reference sites. A linear regression of the natural logarithms of the coda spectral ratio in the frequency range between approximately 3 Hz and the high frequency signal limit imposed by noise provides an estimate of C_j as the zero-frequency intercept and $-\pi(\delta k_j)$ as the slope value. The measured slopes of equation (4.9) depend on sediment thickness at the station, whereas the intercept values are generally close to zero (e.g., Figure 4.4). The mean intercept (from 266 measurements) is 0.266 with a standard deviation of 0.412.

Figure 4.4 shows some examples of the coda spectra and spectral ratios recorded at Coastal Plain stations on different thicknesses of sediment. In Figure 4.4 (a), we show the coda acceleration spectra recorded at Coastal Plain stations 440A and Z41A, as well as the reference spectrum from the 06 November 2011 Prague, Oklahoma earthquake. Sediment thickness is ~ 8.0 km at 440A and ~ 2.5 km at Z41A. Relative to the mean reference spectrum, both Coastal Plain spectra are amplified at low frequencies (< 1 Hz) and attenuated at high frequencies. The corresponding natural logarithms of the coda spectral ratios (logarithm of equation 4.6), are also shown in Figure 4.4 (b). We note the high frequency (greater than ~ 2 -3 Hz) spectral trends at station 440A show a steeper slope than at Z41A. The estimated difference in kappa, relative to the reference condition, from linear regression fits according to equation (4.9), is 161 ms and 62 ms for 440A and Z41A, respectively. The frequency range over which equation (4.9) holds depends on the degree and bandwidth of low-frequency amplification, and the signal-to-noise ratios at high frequency. For the example shown in Figure 4.4, this range, where the log spectral ratio versus frequency plot is linear, is from 2.5-11 Hz for 440A, and from 1-7 Hz for Z41A. This was determined from visual inspection

of the coda spectra and the spectra of pre-signal noise. Also shown in Figure 4.4 are two additional examples involving different stations and earthquakes.

Kappa Model

Figure 4.5 shows the δk values determined in this study from the coda spectral ratios and the Lg kappa values determined by Chapman & Conn (2016) at Coastal Plain stations plotted versus the sediment thickness. The estimates of δk values from coda spectral ratios agree well with the Lg kappa estimates, and both sets of values show correlation with the thickness of Coastal Plain sediments. The Lg kappa measurements by Chapman & Conn (2016) are from sites in the Gulf Coastal Plain with only 12 measurements on sediments less than 1 km thick. In contrast, 69 δk values were derived from stations on less than 1 km of sediment, and approximately 30% of those were from stations in the Atlantic Coastal Plain (east of 85° W longitude). The agreement between δk and Lg kappa implies that kappa for the reference condition is small, essentially negligible in comparison to kappa at the Coastal Plain stations examined here.

The δk values are the difference between kappa at the Coastal Plain sites and the reference model (equation 4.9). The thinnest sediment site in the Coastal Plain used to estimate δk in this study has sediments 90 meters thick. Under our assumptions, δk should be near zero for zero sediment thickness. In order to match this constraint, we use a log δk versus log thickness regression model to fit the data. This type of model is supported by some simple theoretical 1-D wave propagation models we examined (Figure 4.6). We calculated theoretical kappa values from models for Coastal Plain sites with different sediment thickness, assuming a plane-layered velocity structure and vertical S-wave incidence. We approximated a gradient model for shear wave velocity and Q by using a large number of horizontal layers. Figure 4.6 shows an example shear wave velocity and Q model for sites with sediment thickness of 5 km and 12 km respectively. The model is crude, constrained by the compressional wave velocity profile near the Gulf coast by Avendonk et al. (2015), with very little information about S-wave Q as a function of depth in the Coastal Plain (Chapman et al., 2008). We assume that

velocity and Q increase rapidly at shallow depth (less than 0.5 km), and that the increase with depth becomes more gradual at greater depths (Figure 4.6). The theoretical kappa values reflect this gradient behavior, increasing rapidly from zero at zero sediment thickness, and transitioning to a more linear increase for thickness greater than 0.5 km (Figure 4.6). Note that the purpose of the modeling shown in Figure 4.6 was simply to identify the form of the regression model to use for fitting the actual observations, shown in Figure 4.5.

The final δk model was derived by combining the measures from the coda and Lg kappa values Chapman & Conn (2016) as a function of sediment thickness Z . This was done because there appears to be no significant systematic difference in the two sets of measures, given the scatter in the observations. The result is

$$\ln(\delta k) = (-2.932 \pm 0.029) + (0.339 \pm 0.020)\ln(Z), \quad (4.10)$$

or

$$\delta k = 0.0533Z^{0.339}, \quad (4.11)$$

where δk is in seconds and Z is in kilometers.

The model above (equation 4.11) is plotted as a thick line in Figure 4.5. The dashed lines are the 84 percentile and 16 percentile levels, calculated by adding and subtracting the regression standard error estimate to the log-log data fit (Equation 4.10). The derivative of equation (4.11) is a decreasing function of Z , predicting a large change of δk values with changes of thickness on thin sediment sections, which becomes less dramatic for thick sequences. This is consistent with our modeling (Figure 4.6) and may be due to the effects of sediment compaction under increasing confining pressure with depth. The model predicts a δk value of ~ 0.053 s at 1 km thickness and a value of ~ 0.124 s for sediment thickness of 12 km.

Lg Analysis

At low frequencies, the coda spectral ratios contain surface wave energy and may not be a good estimate of the relative site response for the higher amplitude parts of the seismogram

that are associated with the Lg phase. Therefore, we calculated the spectral ratios of Lg waves which arrive earlier in the seismograms. We modeled the Lg spectral amplitude recorded at the j th Coastal Plain station from the i th earthquake as

$$Y_{ij}^{Lg}(f) = S_i(f)G_j^{Lg}(f)P(r_{ij})exp(\frac{-\pi r_{ij}f}{Q(f)v}), \quad (4.12)$$

where r_{ij} is hypocentral distance and $P(r_{ij})$ is the geometrical spreading term independent of frequency and $G_j^{Lg}(f)$ is Lg wave site response at Coastal Plain station j . $Q(f)$ is the average quality factor for the crustal wave guide, which is assumed common to all stations and sources, and v is the average velocity of the Lg waves along the propagation path in the crust.

We define the reference condition for the Lg phase in a manner similar to the approach used for the coda, by using a mean of Lg spectra from stations outside the Coastal Plain. However, the Lg spectra depends on the station distance r , and different stations experience different degrees of geometrical spreading and anelastic absorption. This is in contrast to the situation with the coda, where all the spectra are measured at the same lapse time. For the j th station in the Coastal Plain, we compute a corresponding mean reference spectrum using stations outside the Coastal Plain at distances that differ only slightly from r_{ij} , given by

$$\bar{Y}_{ij}^{Lg}(f) = \frac{S_i(f)}{m} \sum_{q=1}^m \hat{G}_q^{Lg}(f)P(r_{iq})exp(\frac{-\pi r_{iq}f}{Q(f)v}), \quad (4.13)$$

for $0.95 r_{ij} \leq r_{iq} \leq 1.05r_{ij}$ and $q = 1,2,3..m$, where m is the total number of non-Coastal Plain stations satisfying the $\pm 5\%$ distance requirement and $\hat{G}_q^{Lg}(f)$ is the site response for Lg waves at non-Coastal Plain station q . The Lg spectral ratio for the j th Coastal Plain station recording the i th earthquake is obtained by dividing equation (4.12) by the reference spectrum given by equation (4.13),

$$R_j^{Lg}(f) = \frac{Y_{ij}^{Lg}(f)}{\bar{Y}_{ij}^{Lg}(f)} = \frac{G_j^{Lg}(f)P(r_{ij})exp(\frac{-\pi r_{ij}f}{Q(f)v})}{\frac{1}{m} \sum_{q=1}^m \hat{G}_q^{Lg}(f)P(r_{iq})exp(\frac{-\pi r_{iq}f}{Q(f)v})} \approx \frac{G_j^{Lg}(f)}{\frac{1}{m} \sum_{q=1}^m \hat{G}_q^{Lg}(f)}. \quad (4.14)$$

Equation 4.14 assumes that the source radiation pattern is constant, for all stations. The Lg wave is comprised of multipath S waves that leave the source over a range of take-off

angles, which tend to average out the radiation pattern at the higher frequencies. However this does not occur to the same degree as with the coda. We expect increased scatter in the Lg ratios due to radiation pattern effects.

4.3 Quantifying Site Response as a Function of Sediment Thickness

As shown by example in Figure 4.4, the response of the Coastal Plain stations relative to the reference condition involves amplification at lower frequencies (less than 1-3 Hz) and attenuation at higher frequencies. These frequency-dependent effects appear to depend on the thickness of Coastal Plain sediments. Figure 4.5 shows that kappa (and the magnitude of attenuation) is correlated with sediment thickness. It turns out that the degree of amplification and the frequencies at which the amplification occurs also depends on sediment thickness.

We examined the behaviors of Lg spectral amplitude ratios with respect to sediment thickness at different frequencies. We combined spectral ratio measurements from all earthquake-Coastal Plain station pairs (equation 4.14). We assume that source radiation pattern effects are negligible, and that the observed spectral ratio of equation (4.14) is a good approximation of the ratio of the site response at a given Coastal Plain station relative to the reference condition. At a given station, for a given earthquake, we binned the spectral ratios according to frequency, using 12 successive frequency intervals (bins), 0.06-0.14, 0.14-0.46, 0.46-0.66, 0.66-0.86, 0.86-1.26, 1.26-1.66, 1.66-2.46, 2.46-3.26, 3.26-4.86, 4.86-6.46, 6.46-8.06, 8.06-11.26 Hz. The center frequencies of the intervals are 0.1, 0.3, 0.56, 0.76, 1.06, 1.46, 2.06, 2.86, 4.06, 5.66, 7.06 and 9.66 Hz, respectively. The binned value is the geometric mean of the spectral amplitudes in each frequency interval.

Figure 4.7 plots the natural logarithms of the frequency-binned Lg spectral ratios as a

function of sediment thickness at the recording station, for bin center frequencies ranging from 0.1 to 2.86 Hz. The scatter is large, but some trends can be discerned. At the lowest frequencies (0.1 and 0.3 Hz), the values are mostly positive and exhibit an increasing trend throughout the range of sediment thickness. At frequencies 0.56-0.76 Hz, the natural logarithms show overall positive values but exhibit a very slight linearly decreasing trend for thickness larger than ~ 1 km. As frequency increases (>1.06 Hz), the logarithms of the Lg spectral ratios become negative at large thickness (>3 km) with a linearly decreasing trend, indicating that attenuation effects of the sediments dominate at high frequencies and become stronger as thickness increases.

The behaviors of the Lg spectral ratios are more complicated in the thickness range 0-3 km, as shown in the lower panels with a zoomed-in view in Figure 4.7. For insight as to how the relation between the Lg spectral ratios and the sediment thickness might behave, we simulated theoretical transfer functions for sites on sediments of different thickness ranging from 100 m to 12 km. We used 1-D plane-layered velocity and Q models (Figure 4.6) assuming vertical S-wave incidence and the quarter-wavelength approximation (Joyner et al., 1981; Boore & Joyner, 1991). We calculated theoretical spectral ratios by dividing the transfer functions for sediments by the transfer function of a model reference site (thin soil layer over basement rock). We found that the natural logarithms of the theoretical spectral ratios can be roughly approximated by bi-linear functions of sediment thickness with different transition thicknesses in a frequency range of 0.1-2.86 Hz. For a given frequency, these piecewise linear functions show a zero value of the natural logarithms of the spectral ratios at zero thickness and can be described as

$$\ln(R) = a_1 + b_1Z, \quad 0 \leq Z \leq Z_0, \quad (4.15)$$

$$\ln(R) = a_2 + b_2Z, \quad Z \geq Z_0, \quad (4.16)$$

where R is the spectral amplitude ratio, Z is the sediment thickness in km and Z_0 is the transition thickness from one linear segment to the other. The coefficients a_1 , b_1 , a_2 and b_2

are constrained by the following conditions:

$$a_1 = 0, \quad (4.17)$$

$$a_1 + b_1 Z_0 = a_2 + b_2 Z_0. \quad (4.18)$$

The observed Lg spectra amplitude ratios in Figure 4.7 are modeled using equations (4.15) and (4.16) with constraints according to equations (4.17) and (4.18) using linear regression with the transition thickness Z_0 at each frequency determined from the theoretical modeling. Figure 4.7 plots the resulting functions, representing site response effects of sediments in the frequency range of 0.1-2.86 Hz, with the transition thickness indicated by triangles. Table 4.4 lists the parameters in equations (4.15 through 4.18) for different frequencies. The corresponding 84 percentile and 4.16 percentile levels were calculated by adding and subtracting the regression standard error of estimate to the means, and are indicated by the dashed lines in Figure 4.7. The regression parameters for different frequencies are listed in Tables 4.5 and 4.6 respectively.

Figure 4.8 plots the logarithms of the Lg spectral ratios at some specific frequencies from 4.06 to 9.66 Hz, versus recording site sediment thickness. The logarithms of the spectral ratios at these higher frequencies become increasingly negative (as frequency increases), indicating a transition from low frequency amplification to high-frequency attenuation which is most obvious for sites with thicker sediments. At frequencies higher than 2.86 Hz, (Figure 8), attenuation effects of the sediments dominate the site response. We modeled the general trends of the spectral ratios at high frequency successfully (Figure 4.8) using equation (4.9) and the sediment thickness-dependent δk model given by equation (4.11). Figure 4.8 shows the predicted values of the Lg spectral ratio. The values were computed using the mean value of 0.266 determined from 266 measurements of the zero-frequency intercept term C_j in equation (4.9). Lg spectral ratio data at frequencies greater than 9.66 Hz are sparse, and show increasing scatter with frequency, largely due to lower signal/noise ratios at the higher frequencies. This is particularly the case for stations on thick sediment in the Gulf Coastal Plain. We estimated the Lg spectral ratio versus sediment thickness function at frequencies

greater than 2.86Hz using equation (4.9) and the thickness-dependent δk model (equation 4.11).

4.4 Target Spectra for the Stochastic Method and Evaluation of the Site Response Model Using Residual Analysis

We used the stochastic method of ground motion simulation to examine the potential use of our spectral ratio model for ground motion prediction in the Coastal Plain. The approach we used follows Chapman & Conn (2016). It involves calculation of a simulated Fourier amplitude spectrum (or “target” spectrum in the context of the stochastic method) using the spectral ratios defined in the previous sections. The residuals are the difference between the logarithms of the observed spectral amplitudes and the simulated target amplitudes.

The stochastic ground-motion simulation method has been frequently used to model high frequency ground motion (Hanks & McGuire, 1981; Boore, 1983; Atkinson & Boore, 2006). The target Fourier amplitude spectrum used in the stochastic method, $T(f)$, is often represented as

$$T(f) = Source(f)Path(f)Site(f), \quad (4.19)$$

where $Source(f)$ is the earthquake source spectrum, $Path(f)$ represents the path effect of S-wave or Lg-wave propagation through the crust, and $Site(f)$ is the site response effect in the vicinity of the recording site. The source spectra were modeled according to Brune (1970, 1971) as

$$Source(f) = B \frac{M_0(2\pi f)^2}{1 + (\frac{f}{f_c})^2} \left(\frac{1}{4\pi\rho\beta^3} \right), \quad (4.20)$$

where M_0 is the earthquake seismic moment, f_c is the corner frequency, β (assumed to be 3.53×10^5 cm/s) is the shear wave velocity at the source, and ρ (assumed to be 2.7 g/cm³)

is the density at the source. The corner frequency f_c is given by

$$f_c = 0.491\beta\left(\frac{\Delta\sigma}{M_0}\right)^{\frac{1}{3}}, \quad (4.21)$$

where $\Delta\sigma$ is the earthquake stress drop in units of dyn/cm^2 , M_0 is in units of $\text{dyn}\cdot\text{cm}$ and the shear wave velocity is expressed in units of cm/s . The constant $B = R_{\theta\phi}F_sV$, where $R_{\theta\phi}$ is the radiation pattern (assumed to be 0.55), F_s is the free-surface effect for Lg (assumed here to be a factor of 2) and V represents the effect of partition of motion onto two horizontal-components (0.71).

The path term for Lg propagation can be expressed as

$$Path(f) = P(r)\exp\left(\frac{-\pi fr}{Q(f)v}\right). \quad (4.22)$$

$P(r)$ in equation (4.22) represents geometrical spreading. At distances beyond approximately 120 km, the Lg-phase exhibits surface wave (cylindrical) geometrical spreading (Wang & Herrmann, 1980; Herrmann & Kijko, 1983; Kennett, 1986). Near the source, where the S-wave field is dominated by direct arrivals, approximate body wave (spherical) spreading is expected, although both theoretical calculations for layered Earth models and empirical observations indicate that geometrical attenuation may differ somewhat from the theoretical $\frac{1}{r}$ far-field spreading for an isotropic source in a homogenous Earth. The apparent spreading may involve source radiation pattern, directivity, focal depth, and different behavior for the vertical and horizontal components (Ou & Herrmann, 1990; Chapman & Godbee, 2012; Atkinson & Boore, 2014; Frankel, 2015). In the distance range from approximately 60 to 120 km, post-critical reflections from the lower crust and the Moho are important, and the S-Lg wave packet amplitude tends to be approximately constant (Burger et al., 1987; Atkinson & Mereu, 1992; Atkinson, 2004). Chapman & Conn (2016) examined two geometrical spreading models in the Gulf Coastal Plain. The models differ only in the nature of spreading at hypocenter distances less than 60 km. We tested both models with our expanded data set for this study. We settled on the following model as being most consistent with the data from all stations (both inside and outside the Coastal Plain region):

$$P(r) = r^{-1.0}, \quad r \leq 60\text{km}, \quad (4.23)$$

$$P(r) = 60^{-1.0}, \quad 60 \leq r \leq 120km, \quad (4.24)$$

$$P(r) = 60^{-1.0} \left(\frac{r}{120}\right)^{-0.5}, \quad r \geq 120km. \quad (4.25)$$

The quality factor $Q(f)$ for the crustal waveguide is assumed to be

$$Q(f) = 600f^{0.42}. \quad (4.26)$$

The quality factor model was arrived at from analysis of residuals using many trials with different models. We looked at high Q models for paths in the Appalachians and central platform and low Q models in the Gulf region. The final model is similar to that of Atkinson & Boore (2014), for rock sites in northeastern North America.

$Site(f)$ in equation (4.19) is the site response term, dependent on the velocity structure and attenuation properties of materials beneath the recording site. As demonstrated in the previous sections, $Site(f)$ for sites in the Coastal Plain differ substantially from the mean condition of sites outside the Coastal Plain. Here we assume the following model for the reference condition (average condition outside the Coastal Plain):

$$Site_{ref}(f) = Fexp(-\pi k_0 f). \quad (4.27)$$

The amplification factor F is the crustal amplification factor of Boore & Thompson (2015) for stable continental regions and $Vs30 = 2.0$ km/s. Following Boore and Thompson, we adopted $k_0 = 0.006$ s recommended by Hashash et al. (2014) for reference sites in Central and Eastern North America. For sites in the Coastal Plain, the site response term is

$$Site_{cp}(f) = Site_{ref}(f)Ratio(f, Z). \quad (4.28)$$

For frequencies in the range $f = 0.1 - 2.86$ Hz, $Ratio(f, Z) = R$, where R is given by equations (4.15) and (4.16) with parameters listed in Table 4.4. For frequencies greater than 2.86 Hz,

$$Ratio(f, Z) = Ratio(2.86Hz, Z)e^{-\pi\delta k(f-2.86)}, \quad (4.29)$$

where δk is given by equation (4.11). Figure 4.9 shows the Lg spectral ratios $Ratio(f, Z)$ plotted as functions of frequency for sediment thickness ranging from zero to 10.5 km.

Examination of Residuals

The residuals are the difference between the logarithms of the observed Lg-wave Fourier amplitude spectra and the target spectra. We calculated three sets of residuals. Reference station residuals were calculated using equation (4.27) to define the site response. We calculated Coastal Plain residuals also using equation (4.27) to define the site response. We refer to the second set of residuals as the “uncorrected” Coastal Plain residuals. We calculated a third set of residuals for the Coastal Plain sites with the target spectrum defined using the Coastal Plain site response given by equation (4.28). We refer to this third set of residuals as the “corrected” Coastal Plain residuals.

Figure 4.10 shows the three sets of residuals for the 8 November 2011 Oklahoma earthquake at 5 frequencies, plotted versus hypocenter distance and sediment thickness. For reference, Figure 4.10 also shows the mean and mean \pm one standard deviation residual values for the reference stations. The residuals for the reference stations are well behaved, with mean values near zero at all frequencies and no apparent distance dependence. In contrast, the uncorrected Coastal Plain residuals show a strong frequency dependence, with a dependence on distance and sediment thickness at frequencies greater than 1 Hz. Relative to the residuals for the reference stations, the uncorrected Coastal Plain residuals tend to be positive at low frequencies (less than 1 Hz) and negative at higher frequencies. The corrected Coastal Plain residuals match the behavior of the reference residuals in terms of amplitude and lack of distance and sediment thickness dependence. Note that the plots of residuals versus sediment thickness show much less scatter at high frequency, compared to the residuals plotted versus distance. We consider this convincing evidence that sediment thickness plays the dominant role in explaining the variability of attenuation in the Coastal Plain. The apparent distance dependent behavior of the high-frequency uncorrected residuals in the left column of Figure 4.10 exists because many of the more distant stations from this earthquake lie near the Gulf coast, on extremely thick sediment (Chapman & Conn, 2016).

Figures 4.11 and 4.12 show residuals for the 8 April 2011 Arkansas and 10 November

2012 Kentucky earthquakes, respectively. Although these earthquakes are widely separated in location, in both cases the patterns of the residuals are similar to those observed for the Oklahoma earthquake (Figure 4.10). The residuals for the reference stations are near zero at all frequencies and show no obvious distance dependence. Likewise, the uncorrected Coastal Plain residuals are mostly positive relative to the mean of the reference residuals at frequencies less than 1 Hz, whereas they are negative at higher frequencies, becoming systematically more negative as sediment thickness increases. The corrected Coastal Plain residuals match the reference residuals well, implying that our model for the ratio of the site response of the Coastal Plain to that of the reference condition ($Ratio(f, Z)$) in equation (4.28) works well for these events.

The residual patterns shown in Figures 4.10-4.12 hold for most of the earthquakes in our data set. In Figures 4.15-4.17, we have condensed the information for all events by plotting the mean residuals for the reference stations, uncorrected Coastal Plain stations and corrected Coastal Plain stations as functions of frequency. In most cases, the mean uncorrected Coastal Plain residuals equal or exceed those of the reference stations at lower frequencies (less than 1 or at most, 5 Hz), and are less (more negative) than the mean residual of the reference stations at higher frequency. In most cases, the corrected mean residuals are closer to the values of the mean reference residuals, particularly at higher frequencies (> 1-5 Hz). Exceptions to this behavior involve the 30 November 2017 Delaware event at high frequency, the 20 November 2010 Arkansas event at low frequency, the 12 December 2018 Tennessee event at high frequency and two earthquakes that occurred in the Coastal Plain of Texas. The data sets for the Delaware, Arkansas and Tennessee events are small. The two Texas events represent important exceptional cases. They were the only two well-recorded events with epicenters within the Gulf Coastal Plain available for this study.

Figure 4.13 shows the residuals for the 20 October 2011 earthquake in southern Texas. The residuals behave in similar fashion to those shown in Figures 4.10-4.12 at frequencies less than 1 Hz: the reference residuals are near zero and uncorrected Coastal Plain residuals exceed the mean value of the reference residuals. The corrected Coastal Plain residuals

show good agreement with the reference residuals at frequencies less than 1 Hz. However, the reference residuals are very significantly negative at higher frequencies, showing little difference with the uncorrected Coastal Plain residuals. All sites experience significant high frequency attenuation, regardless of where they are located, relative to the prediction of our reference site model. On the other hand, the corrected Coastal Plain residuals are much closer to zero value, suggesting that the model expressed by equation (4.28) is at least somewhat effective in predicting the actual ground motion for sites in the Coastal Plain from shocks located within it.

The negative values of the high frequency reference residuals for the two earthquakes in the Texas Coastal Plain suggest that stations outside the Coastal Plain experience substantial Lg-wave attenuation on the source end of the path. Reciprocity suggests that it should be possible to account approximately for this behavior by using the Coastal Plain site response term (equation 4.28) to calculate the target spectrum for the reference stations at high frequency, assuming that the earthquake focal depths are within the sedimentary section or at least not significantly below the top of the basement. The focal depth of the 20 October, 2011 event was estimated at 3 km (Table 4.1), and the thickness of the Coastal Plain section is approximately 5.5 km at the epicenter. The May 17, 2012 eastern Texas event had an estimated depth of 5 km and the sediment thickness at the epicenter is approximately 4 km. We believe that these induced events probably occurred at or near the top of the basement, in which case a correction based on the thickness of the sediments at the epicenter (Z) would be appropriate. Figure 4.14 shows the result of correcting both the Coastal Plain residuals and the reference stations residuals, for the 20 October 2011 southern Texas earthquake, at frequencies greater than 1.0 Hz. The corrected Coastal Plain residuals and the corrected reference residuals are near zero and in good agreement. We found similar results for the 5 May 2011 eastern Texas earthquake (Figure 4.18).

4.5 Conclusions

We used both coda and Lg-wave spectral ratios to study Lg-wave propagation in the Atlantic and Gulf Coastal Plain, relative to a reference site condition. The results of the study are in the form of bi-linear equations (equations 4.15 and 4.16, with coefficients listed in Tables 4.4, 4.5 and 4.6) that relate the Lg wave Fourier amplitude spectral ratios of the Coastal Plain sites to the reference condition as functions of sediment thickness at frequencies of 0.1, 0.3, 0.56, 0.76, 1.06, 1.46, 2.06 and 2.86 Hz. The spectral ratios at frequencies greater than 2.86 Hz are given by equation (4.29), which involves our model for differential kappa (δk) that is a function of sediment thickness (equation 4.11). Equation (4.29) and the δk model can be used to account for high-frequency attenuation that occurs for receiver locations outside the Coastal Plain for shocks located within the Coastal Plain. We observed apparent near-source, high-frequency attenuation at distant stations outside the Coastal Plain from shocks in southern and eastern Texas.

The reference condition is not a “rock” site, but rather is the mean site condition of many stations located outside the Atlantic and Gulf Coastal Plain. This should be kept in mind if these results are applied in site-specific ground motion prediction. We find that significant accumulations of Coastal Plain sediment amplify the low frequencies (less than approximately 1 Hz) and attenuate high frequencies (e.g., greater than approximately 3 Hz), relative to the reference condition, with thickness of the Coastal Plain sediment being the key variable controlling geographic variability of response. The frequencies at which amplification occurs and the magnitude of the attenuation are functions of Coastal Plain sediment thickness.

The results of the study may be used to develop target Fourier amplitude spectra for the stochastic method of ground motion simulation. Such simulations could be used to develop engineering response spectral ratios, (Coastal Plain/reference) as functions of earthquake magnitude, hypocenter distance and sediment thickness, provided that appropriate duration models are available.

Bibliography

- Aki, K. & Chouet, B., 1975. Origin of coda waves: Source, attenuation, and scattering effects, *J. Geophys. Res.*, **80**, 3322–3342.
- Anderson, J. & Hough, S., 1984. A model for the shape of the Fourier amplitude spectrum of acceleration at high frequencies, *Bull. Seismol. Soc. Am.*, **74**, 1969–1993.
- Atkinson, G. M., 2004. Empirical attenuation of ground-motion spectral amplitudes in southeastern Canada and the northeastern United States, *Bull. Seismol. Soc. Am.*, **94**, 1079–1095.
- Atkinson, G. M. & Boore, D. M., 2006. Earthquake ground-motion prediction equations for eastern north america, *Bull. Seismol. Soc. Am.*, **96**, 2181–2205.
- Atkinson, G. M. & Boore, D. M., 2014. The attenuation of fourier amplitudes for rock sites in eastern North America, *Bull. Seismol. Soc. Am.*, **104**, 513–528.
- Atkinson, G. M. & Mereu, R., 1992. The shape of ground motion attenuation curves in southeastern Canada, *Bull. Seismol. Soc. Am.*, **82**, 2014–2031.
- Avendonk, V., Harm, J. A., Christeson, G. L., Norton, I. O., & Eddy, D. R., 2015. Continental rifting and sediment infill in the northwestern Gulf of Mexico, *Geology*, **43**, 631–634.
- Boore, D. M., 1983. Stochastic simulation of high-frequency ground motions based on seismological models of the radiated spectra, *Bull. Seismol. Soc. Am.*, **73**, 1865–1894.

- Boore, D. M. & Joyner, W. B., 1991. Estimation of ground motion at deep-soil sites in eastern North America, *Bull. Seismol. Soc. Am.*, **81**, 2167–2185.
- Boore, D. M. & Thompson, E. M., 2015. Revisions to some parameters used in stochastic-method simulations of ground motion, *Bull. Seismol. Soc. Am.*, **105**, 1029–1041.
- Borcherdt, R. D., 1970. Effects of local geology on ground motion near San Francisco Bay, *Bull. Seismol. Soc. Am.*, **60**, 29–61.
- Brune, J., 1970. Tectonic stress and the spectra of seismic shear waves from earthquakes, *J. Geophys. Res.*, **75**, 4997–5009.
- Brune, J., 1971. Correction, *J. Geophys. Res.*, **76**, 5002.
- Burger, R. W., Somerville, P. G., Barker, J. S., Herrmann, R. B., & V., H. D., 1987. The effects of crustal structure on strong ground motion attenuation relations in eastern North America, *Bull. Seismol. Soc. Am.*, **77**, 420–439.
- Chapman, M. & Conn, A., 2016. A model for Lg propagation in the Gulf Coastal Plain of the southern United States, *Bull. Seismol. Soc. Am.*, **106**, 349–363.
- Chapman, M. C. & Godbee, R. W., 2012. Modeling geometrical spreading and the relative amplitudes of vertical and horizontal high-frequency ground motions in eastern North America, *Bull. Seismol. Soc. Am.*, **102**, 1957–1975.
- Chapman, M. C., Bollinger, G. A., Sibol, M. S., & Stephenson, D. E., 1990. The influence of the Coastal Plain sedimentary wedge on strong ground motions from the 1886 Charleston, South Carolina, earthquake, *Earthquake Spectra*, **6**, 617–640.
- Chapman, M. C., Beale, J. N., & Catchings, R. D., 2008. Q for P-waves in the sediments of the Virginia Coastal Plain, *Bull. Seismol. Soc. Am.*, **98**, 2022–2032.
- Cramer, C. H., 2018. Gulf Coast regional Q boundaries from USArray data, *Bull. Seismol. Soc. Am.*, **108**, 427–449.

- Frankel, A., 2015. Decay of S-wave amplitude with distance from earthquakes in the Charlevoix, Quebec area: Effects of radiation pattern and directivity, *Bull. Seismol. Soc. Am.*, **105**, 850–857.
- Frankel, A., McGarr, A., Bicknell, J., Mori, J., Seeber, L., & Cranswick, E., 1990. Attenuation of high-frequency shear waves in the crust: Measurements from New York state, South Africa, and southern California, *J. Geophys. Res.*, **95**, 17441–17457.
- Galloway, W. E., 2008. Depositional evolution of the gulf of mexico sedimentary basin, in *Sedimentary Basins of the United States and Canada*, pp. 505–548, ed. Miall, A., Sedimentary Basins of the World, Elsevier, Amsterdam, The Netherlands.
- Garrity, C. P. & Soller, D. R., 2009. Database of the geologic map of North America-Adapted from the map by J.C. Reed, Jr. and others (2005), Tech. rep., U.S. Geological Survey Data Series 424, <http://pubs.usgs.gov/ds/424/> (last accessed February 2019).
- Gupta, I., McLaughlin, K. L., Wagner, R. A., Jih, R. S., & McElfresh, T. W., 1989. Seismic wave attenuation in eastern North America, Tech. Rep. EPRI Rept. NP-6304, Electric Power Research Institute, Palo Alto, California.
- Hanks, T. C. & McGuire, R. K., 1981. The character of high-frequency strong ground motion, *Bull. Seismol. Soc. Am.*, **71**, 2071–2095.
- Hashash, Y. M. A., Kottke, A. R., Stewart, J. P., Campbell, K. W., Kin, B., Moss, C., Nikolaou, S., Rathje, E. M., & Silva, W. J., 2014. Reference rock site condition for Central and Eastern North America, *Bull. Seismol. Soc. Am.*, **104**, 684–701.
- Herrick, S. M. & Vorhis, R. C., 1963. Subsurface geology of the georgia coastal plain, georgia state division of conservation, Tech. Rep. 25, Dept. of Mines, Mining and Geology, Information Circular.
- Herrmann, R. B. & Kijko, A., 1983. Modeling some empirical Lg relations, *Bull. Seismol. Soc. Am.*, **73**, 157–171.

- Joyner, W. B., Warrick, R. E., & Fumal, T. E., 1981. The effect of Quaternary alluvium on strong ground motion in the Coyote Lake, California earthquake of 1979, *Bull. Seismol. Soc. Am.*, **71**, 1333–1349.
- Kennett, B. L. N., 1986. Lg waves and structural boundaries, *Bull. Seismol. Soc. Am.*, **76**, 1133–1141.
- Lawrence, D. P. & Hoffman, C. W., 1993. Geology of basement rocks beneath the north carolina coastal plain, Tech. Rep. 95, North Carolina Geological Survey, Division of Land Resources, Department of Environment, Health and Natural Resources, Bulletin.
- Mcbride, J. H., 1991. Constraints on the structure and tectonic development of the Early Mesozoic South Georgia Rift, southeastern United States; Seismic reflection data processing and interpretation, *Tectonics*, **10**, 1065–1083.
- McBride, J. H. & Nelson, K. D., 1988. Integration of COCORP deep reflection and magnetic anomaly analysis in the southeastern United States: implications for origin of the Brunswick and East Coast magnetic anomalies, *Geological Society of America Bulletin*, **100**, 436–445.
- McBride, J. H., Nelson, K. D., & Brown, L. D., 1989. Evidence and implications of an extensive early Mesozoic rift basin and basalt/diabase sequence beneath the southeast Coastal Plain, *Geological Society of America Bulletin*, **101**, 512–520.
- Ou, G. B. & Herrmann, R. B., 1990. A statistical model for ground motion produced by earthquakes at local and regional distances, *Bull. Seismol. Soc. Am.*, **80**, 1397–1417.
- Parker, E. H., Hawman, R. B., Fischer, K. M., & Wagner, L. S., 2013. Crustal evolution across the southern Appalachians: Initial results from the SESAME broadband array, *Geophys. Res. Lett.*, **40**, 3853–3857.
- Pasyanos, M. E., 2013. A lithospheric attenuation model for North America, *Bull. Seismol. Soc. Am.*, **103**, 3321–3333.

- Powars, D. S., Edwards, L., Kidwell, S. M., & Schindler, J. S., 2015. Cenozoic stratigraphy and structure of the Chesapeake Bay region, in *Tripping from the Fall Line: Field Excursions for the GSA Annual Meeting, Baltimore, 2015*, vol. 40, pp. 171–229, eds Brezinski, D. K., Halka, J. P., & Ortt Jr., R. A., Geological Society of America Field Guide.
- Pratt, T. L., Horton, J. W., Munoz, J., Hough, S. E., Chapman, M. C., & Olgun, C. G., 2017. Amplification of earthquake ground motions in Washington, DC, and implications for hazard assessments in central and eastern North America, *Geophys. Res. Lett.*, **44**, 12150–12160.
- Salvador, A., 1991a. The gulf of Mexico basin, chapter 1 introduction, in *The Gulf of Mexico Basin*, vol. J, pp. 1–12, ed. Salvador, A., The Geology of North America, Geological Society of America, Boulder, Colorado.
- Salvador, A., 1991b. Structure at the base and subcrop below Mesozoic marine section, Gulf of Mexico basin, in *The Gulf of Mexico Basin*, vol. J, pp. 1–12, ed. Salvador, A., The Geology of North America, Geological Society of America, Boulder, Colorado.
- Sawyer, D. S., Buffler, R. T., & Pilger Jr., A., 1991. The crust under the Gulf of Mexico basin, in *The Gulf of Mexico Basin*, vol. J, pp. 53–72, ed. Salvador, A., The Geology of North America, Geological Society of America, Boulder, Colorado, 1-12.
- Thomas, W. A., 1989. The appalachian-ouachita orogen beneath the gulf coastal plain between the outcrops in the appalachian and ouachita mountains, in *he Appalachian-Ouachita Orogen in the United States*, vol. F-2, pp. 537–554, eds Hatcher, R. D., Thomas, W. A., & Viele, G. W., The Geology of North America, Geological Society of America, Boulder, Colorado.
- Thomas, W. A., 2010. Interactions between the southern Appalachian-Ouachita orogenic belt and basement faults in the orogenic footwall and foreland, in *From Rodinia to Pangea: The Lithotectonic Record of the Appalachian Region*, vol. 206, pp. 897–916, eds Tollo, R. P., Bartholomew, M. J., Hibbard, J. P., & Karabinos, P. M., Geological Society of America.

- Thomas, W. A., Chowns, T. M., Daniels, D. L., Neathery, T. L., & Glover III, L., 1989. The subsurface Appalachians beneath the Atlantic and Gulf Coastal Plains, in *the Appalachian-Ouachita Orogen in the United States*, vol. F-2, pp. 445–458, eds Hatcher, R. D., Thomas, W. A., & Viele, G. W., The Geology of North America, Geological Society of America, Boulder, Colorado.
- Wait, R. L. & Davis, M. E., 1986. Configuration and hydrology of the pre-cretaceous rocks underlying the southeastern coastal plain aquifer system, Tech. Rep. 86-4010, U.S. Geological Survey, Water-Resources Investigations.
- Wang, C. Y. & Herrmann, R. B., 1980. A numerical study of P-, SV- and SH-wave generation in a plane layered medium, *Bull. Seismol. Soc. Am.*, **70**, 1015–1036.
- Wu, Q. & Chapman, M., 2017. Stress-drop estimates and Source Scaling of the 2011 Mineral, Virginia, mainshock and aftershocks, *Bull. Seismol. Soc. Am.*, **107**, 2703–2720.
- Wu, Q., Chapman, M. C., Beale, J. N., & Shamsalsadati, S., 2016. Near-source geometrical spreading in the central Virginia seismic zone determined from the aftershocks of the 2011 Mineral, Virginia, earthquake, *Bull. Seismol. Soc. Am.*, **106**, 943–955.

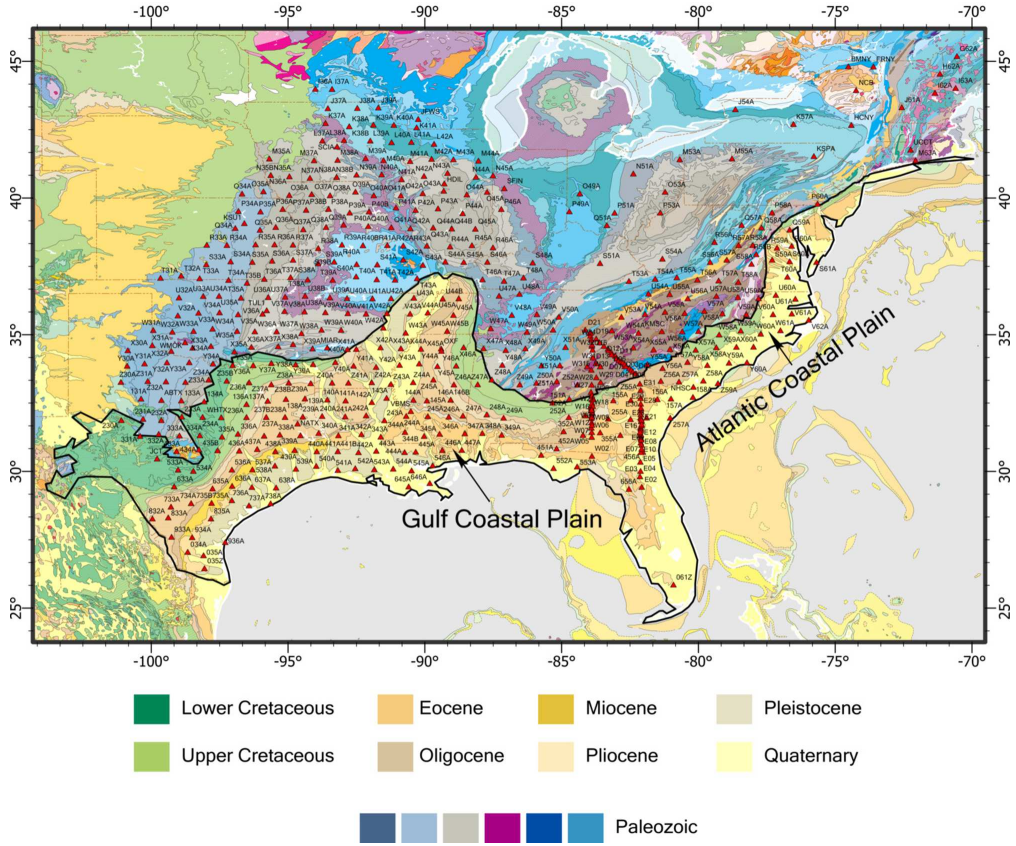


Figure 4.1: Geologic map of the central and eastern United States. Locations and station codes of the Earthscope Transportable Array (TA) stations (triangles), the United States National Seismic Network (US) stations (hexagons), the Central and Eastern US Network (N4) stations (circles), the Lamont-Doherty Cooperative Seismographic Network (LD) stations (stars) and the Southeastern Suture of the Appalachian Margin Experiment (Z9) stations (diamonds) used in this study are indicated. The thick solid curve shows the boundary of the Atlantic and Gulf Coastal Plain. Adapted from Garrity & Soller (2009).

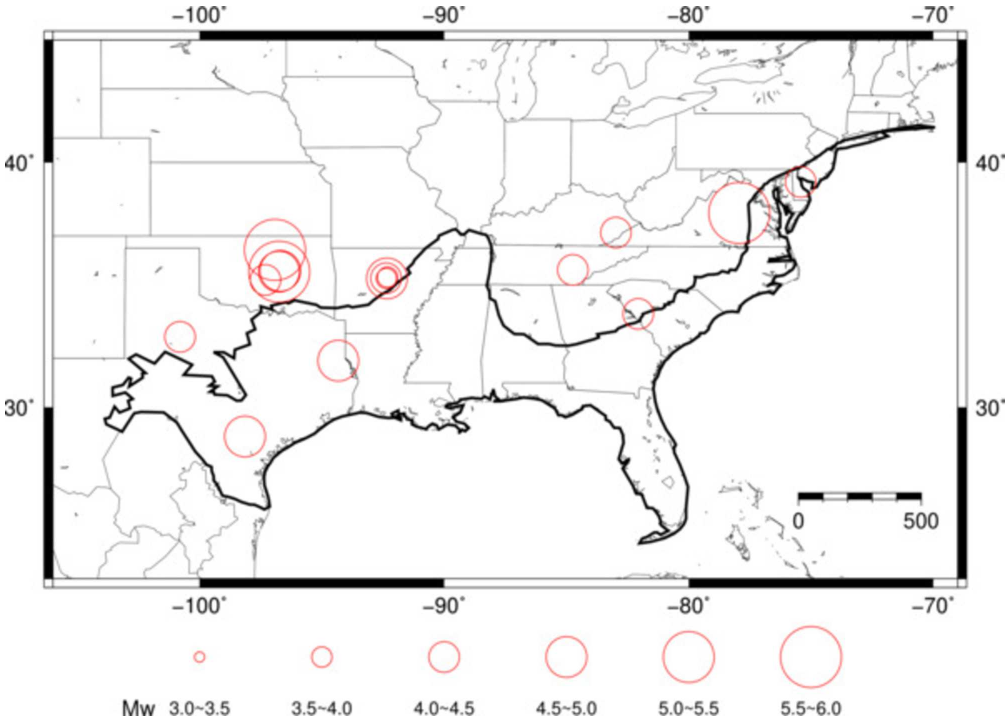


Figure 4.2: Epicenters of earthquakes (circles) used in this study. Sizes of the circles are scaled to the moment magnitude listed in Table 4.1.

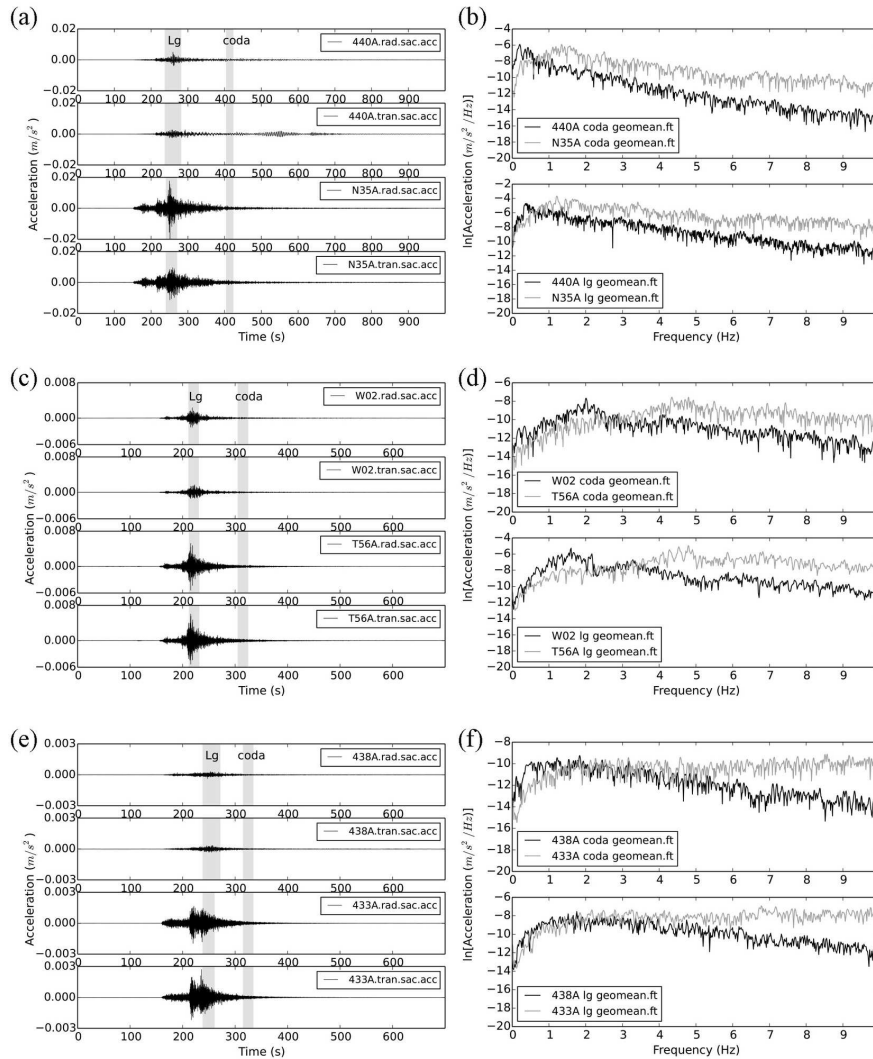


Figure 4.3: (a) Horizontal-component acceleration seismograms recorded at station 440A in eastern Texas and station N35A in eastern Nebraska, from the Mw 5.65 06 November 2011 earthquake in Oklahoma. The stations are at a distance of ~ 590 km. The shaded areas from left to right denote the windows used for calculating Lg and coda spectra respectively. (b) Corresponding geometric mean of coda and Lg spectra from the two horizontal recordings at station 440A and station N35A using the windows defined in (a). (c) and (d) are the same as (a) and (b) but recorded at station W02 in northern Florida and station T56A in western Virginia, from the Mw 4.11 15 February 2014 earthquake in South Carolina, with epicentral distance of ~ 390 km. (e) and (f) are the same as (a) and (b) but recorded at station 438A in southeastern Texas and station 433A in the Llano uplift of central Texas, from the Mw 4.33 13 October 2010 earthquake in Oklahoma, with epicentral distance of ~ 500 km.

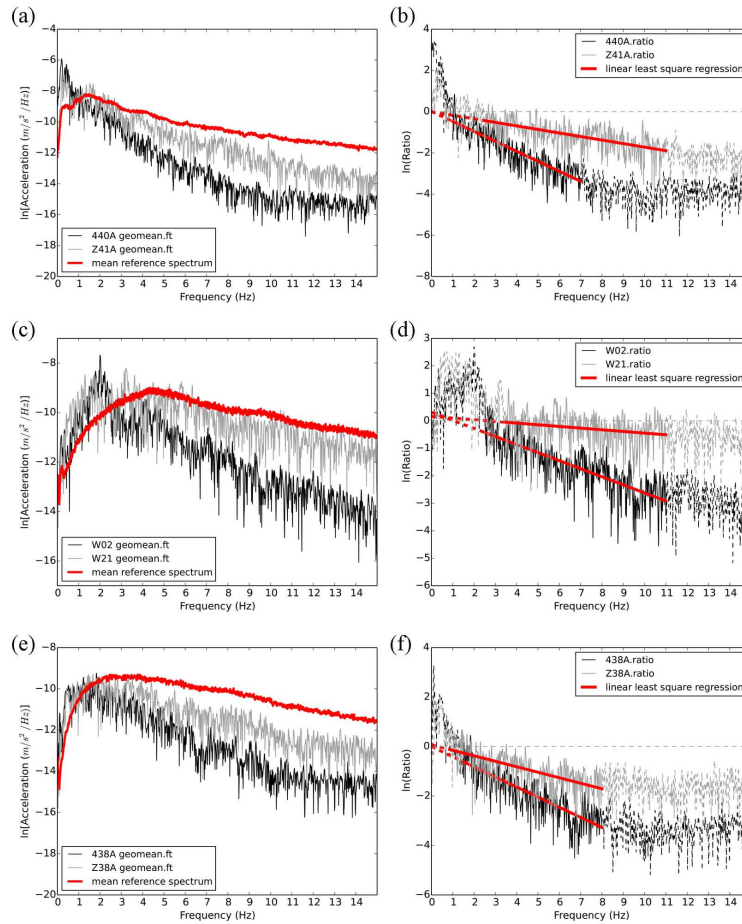


Figure 4.4: In the top panel, (a) shows the geometric mean of Fourier acceleration amplitude spectra for horizontal-component coda waves, computed from a 20 s window at a lapse time of 334 s after the origin time of the 06 November 2011 Prague earthquake in Oklahoma. The black line and gray line are computed from coda waves recorded at Coastal Plain stations 440A and Z41A, underlain by sediments of thickness ~ 8 km and ~ 2.5 km respectively. The thicker line is the mean coda reference spectrum computed for non-Coastal Plain stations. (b) Ratios of coda spectra at station 440A (black) and station Z41A (gray) shown in (a), to the mean reference spectrum (thicker line in (a)). The solid line segments indicate the frequency ranges of spectral ratios used for linear regression (thicker lines). (c) and (d) are the same as (a) and (b) but for coda waves from the 15 February 2014 South Carolina earthquake recorded at station W02 with sediment thickness ~ 2.5 km and station W21 with ~ 0.5 km of sediment. Coda spectra are calculated at a lapse time of 280 s after the event origin time. (e) and (f) are the same as (a), (b) but for coda waves from the 13 October 2010 Oklahoma earthquake recorded at station 438A with sediment thickness ~ 8.0 km and station Z38A with ~ 3.0 km of sediment. Coda spectra are calculated at a lapse time of 225 s after the event origin time.

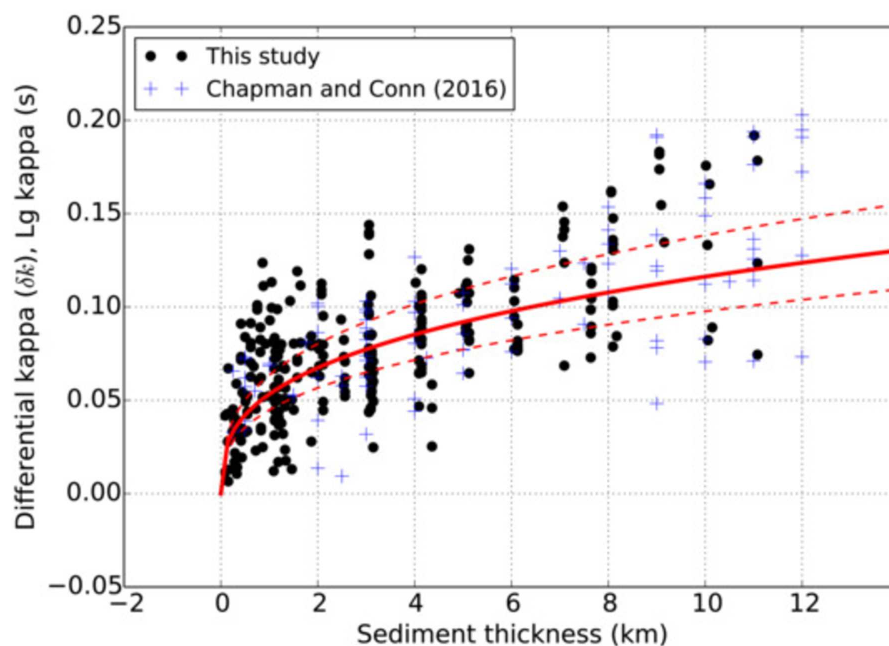


Figure 4.5: Differential kappa (δk) from linear least square regression of coda spectral ratios in this study (dots) and Lg kappa from Chapman and Conn (2016) (crosses) versus thickness of the post-Jurassic marine sedimentary section. Outliers at the 5% and 95% level from an initial regression were removed for the final regression results shown here. Solid line shows the least-square regression fit to both data sets, $\delta k = e^{-2.932} Z^{0.339}$ (regression model: $\ln(\delta k) = (-2.932 \pm 0.029) + (0.339 \pm 0.020)\ln(Z)$), where Z is the thickness of Coastal Plain marine sediment in km. The dashed lines are the 84 percentile and 16 percentile levels, calculated by adding and subtracting the regression standard error of estimate to the log-log data fit.

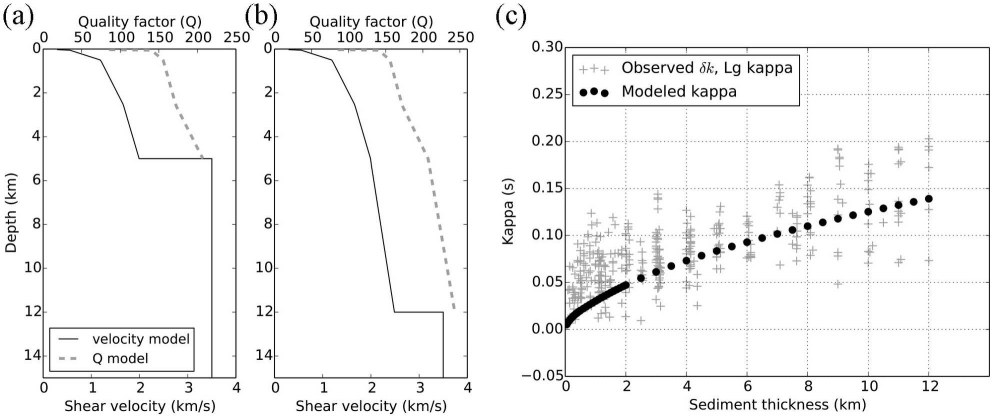


Figure 4.6: (a) Shear wave velocity and Q versus depth assumed for the Coastal Plain (5 km sediment thickness). (b) Same as (a) for 12 km sediment thickness. (c) Differential kappa (δk) values for the assumed model (dots), compared to observed δk and Lg kappa values (crosses).

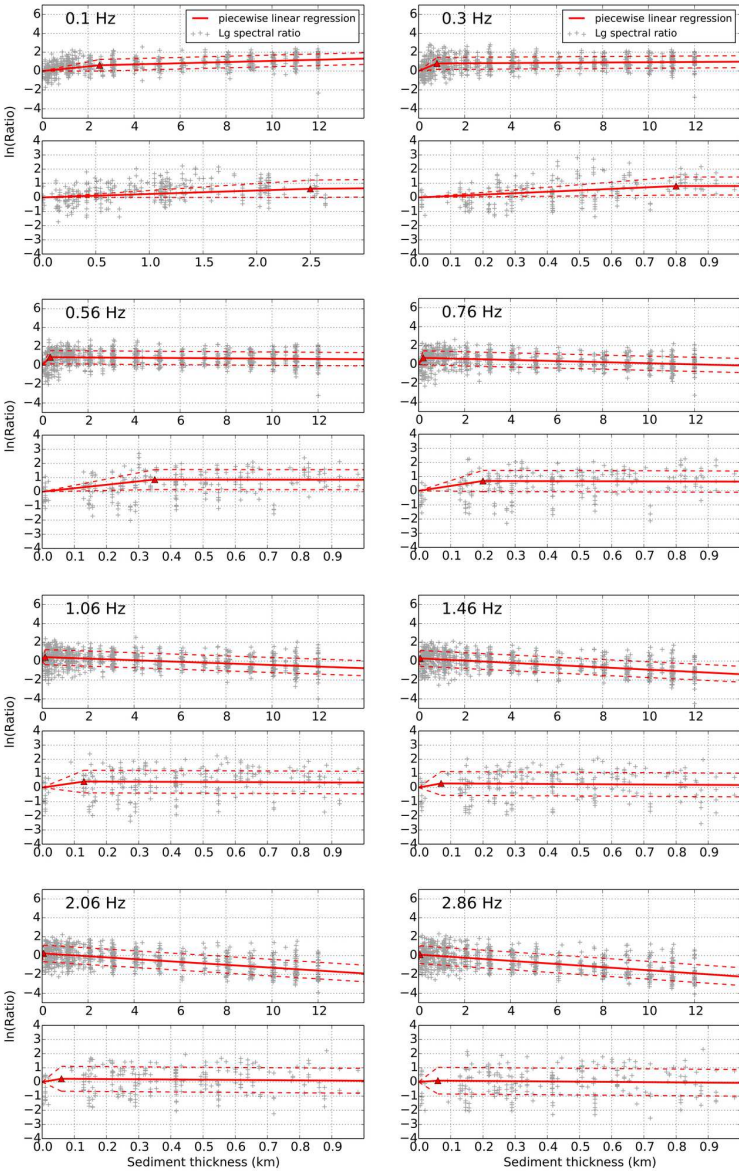


Figure 4.7: Natural logarithms of Lg spectra amplitude ratios versus sediment thickness, averaged over 8 frequency bands. The thick solid lines indicate the piecewise linear regression model fit to the data. The corresponding 84 percentile and 16 percentile levels were calculated by adding and subtracting the regression standard error of estimate to the means, and are indicated by the dashed lines. The lower figure is zoomed into a smaller thickness range for a better view of the transition thickness (triangle).

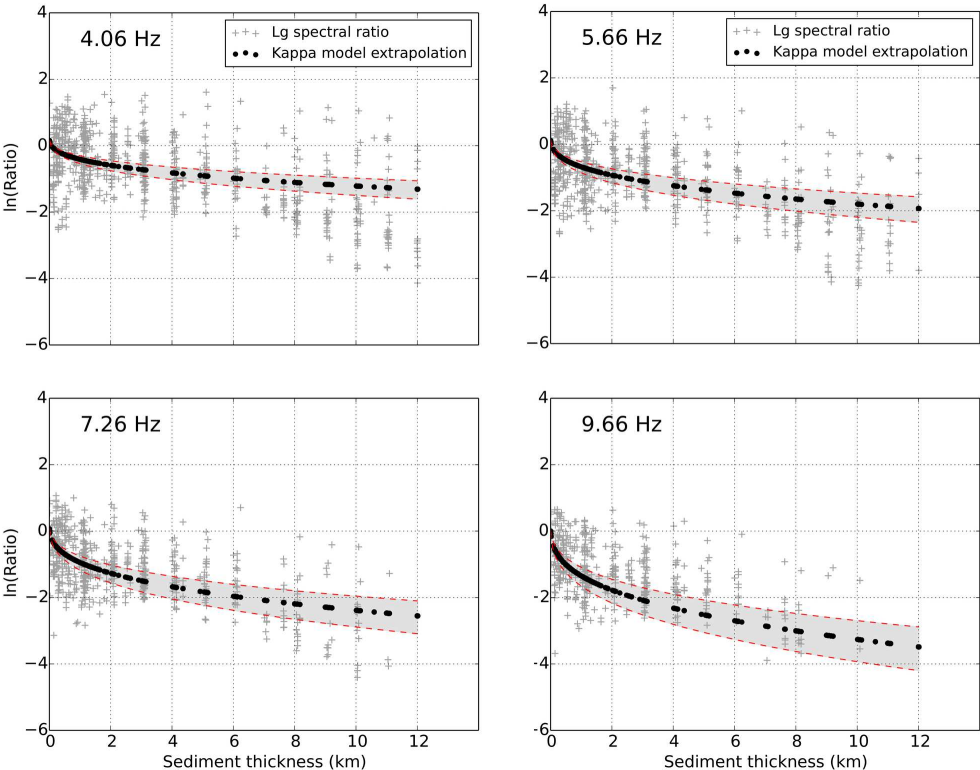


Figure 4.8: Natural logarithms of Lg spectra amplitude ratios (crosses) averaged in 4 successive frequency bins versus sediment thickness, compared to predicted amplitude ratios (dots) based on equation (4.9) with the δk model in equation (4.11). The shaded area shows the 84 percentile and 16 percentile range of the predicted amplitude ratios, based on the 16–84 percentile range of the δk model calculated by adding and subtracting the regression standard error of estimate to the log-log data fit (Equation 4.10).

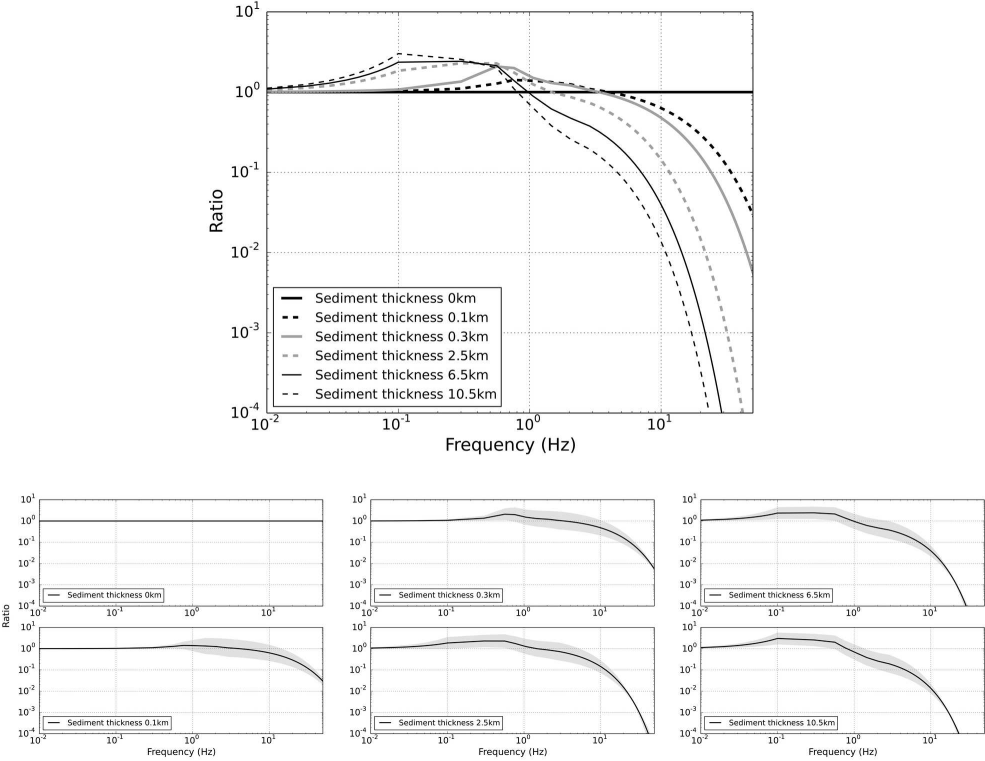


Figure 4.9: L_g spectral ratios $Ratio(f, Z)$ from equations (4.15) and (4.16) with parameters listed in Table 4.4 for frequencies less than 2.86 Hz. Higher frequency values are from equations (4.29) and (4.11). At the bottom, the shaded region indicates the area bounded by the 16 percentile and 84 percentile levels for the ratio function with different sediment thickness.

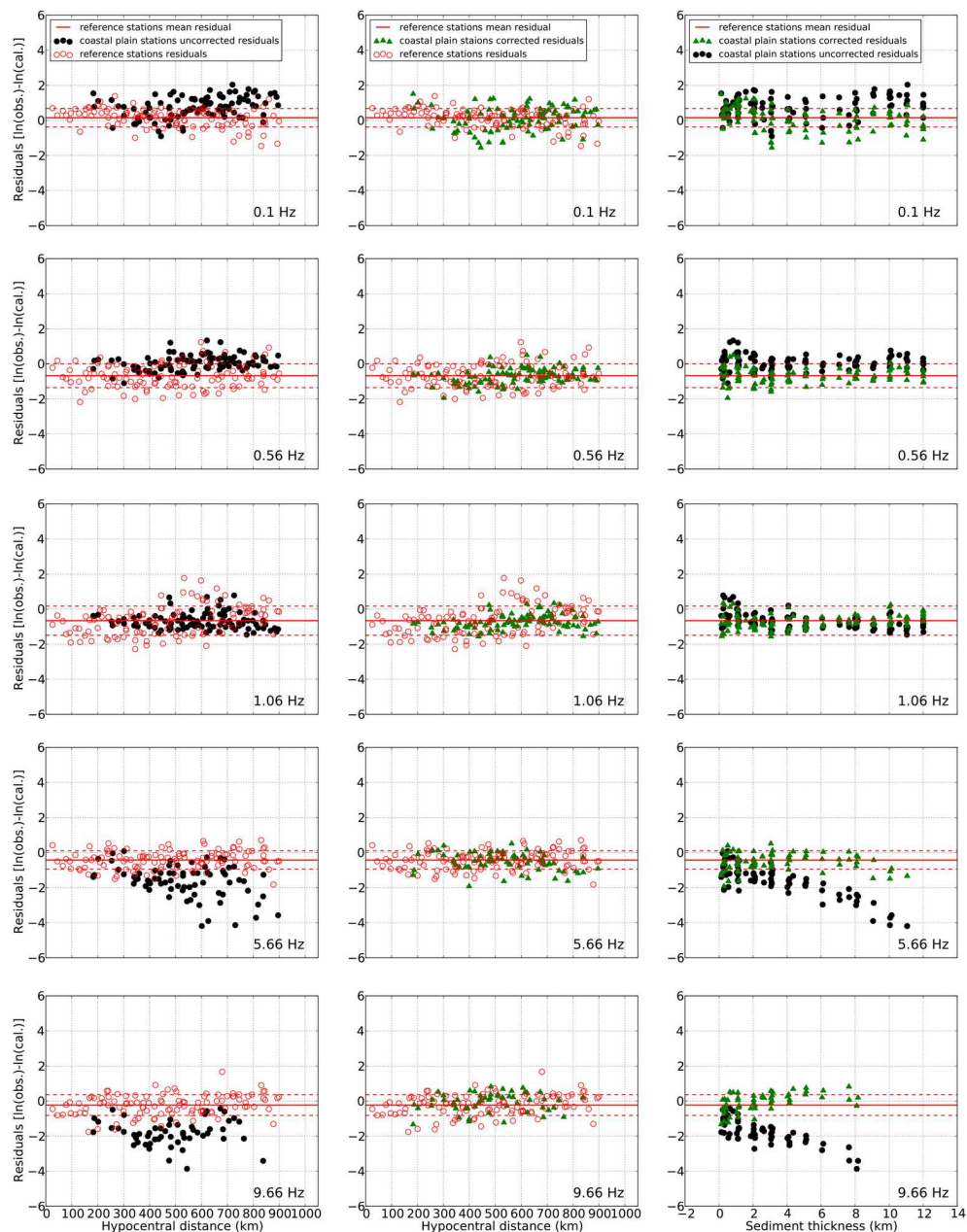


Figure 4.10: Uncorrected and corrected Coastal Plain station residuals and reference station residuals at different frequencies plotted versus distance and Coastal Plain sediment thickness for the 08 November 2011 earthquake in central Oklahoma.

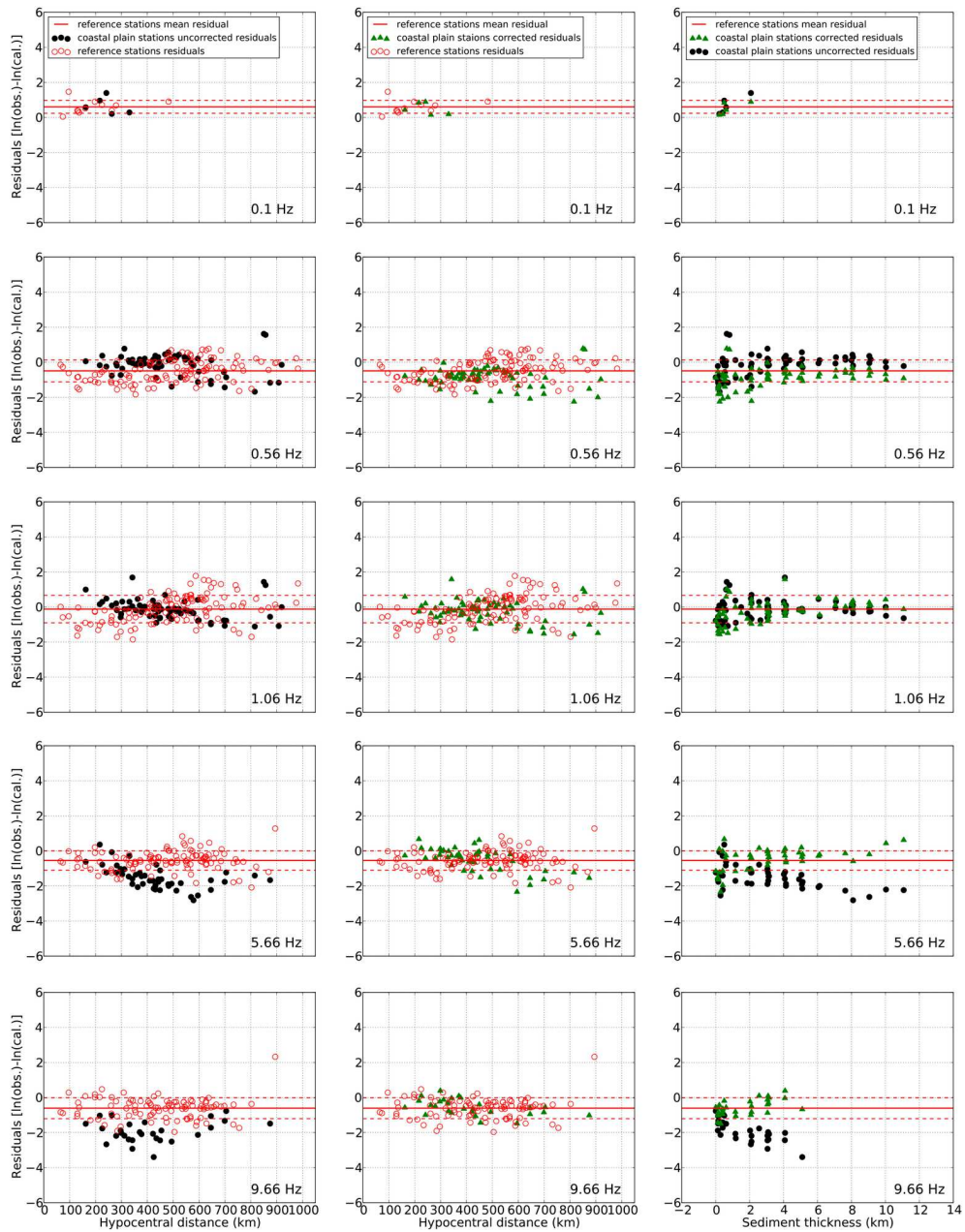


Figure 4.11: Same as Figure 4.10 but for the 08 April 2011 Arkansas earthquake.

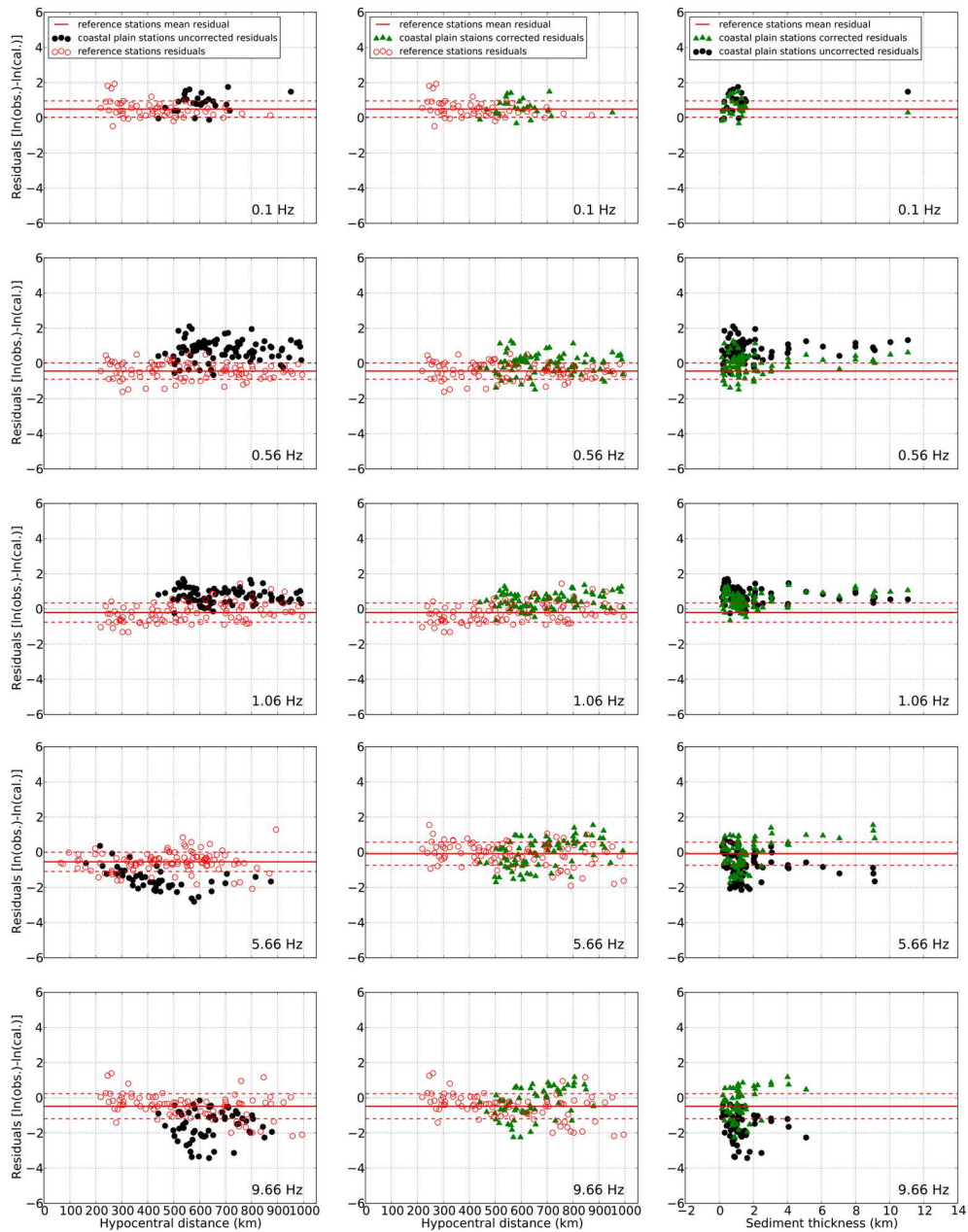


Figure 4.12: Same as Figure 4.10 but for the 10 November 2012 Kentucky earthquake.

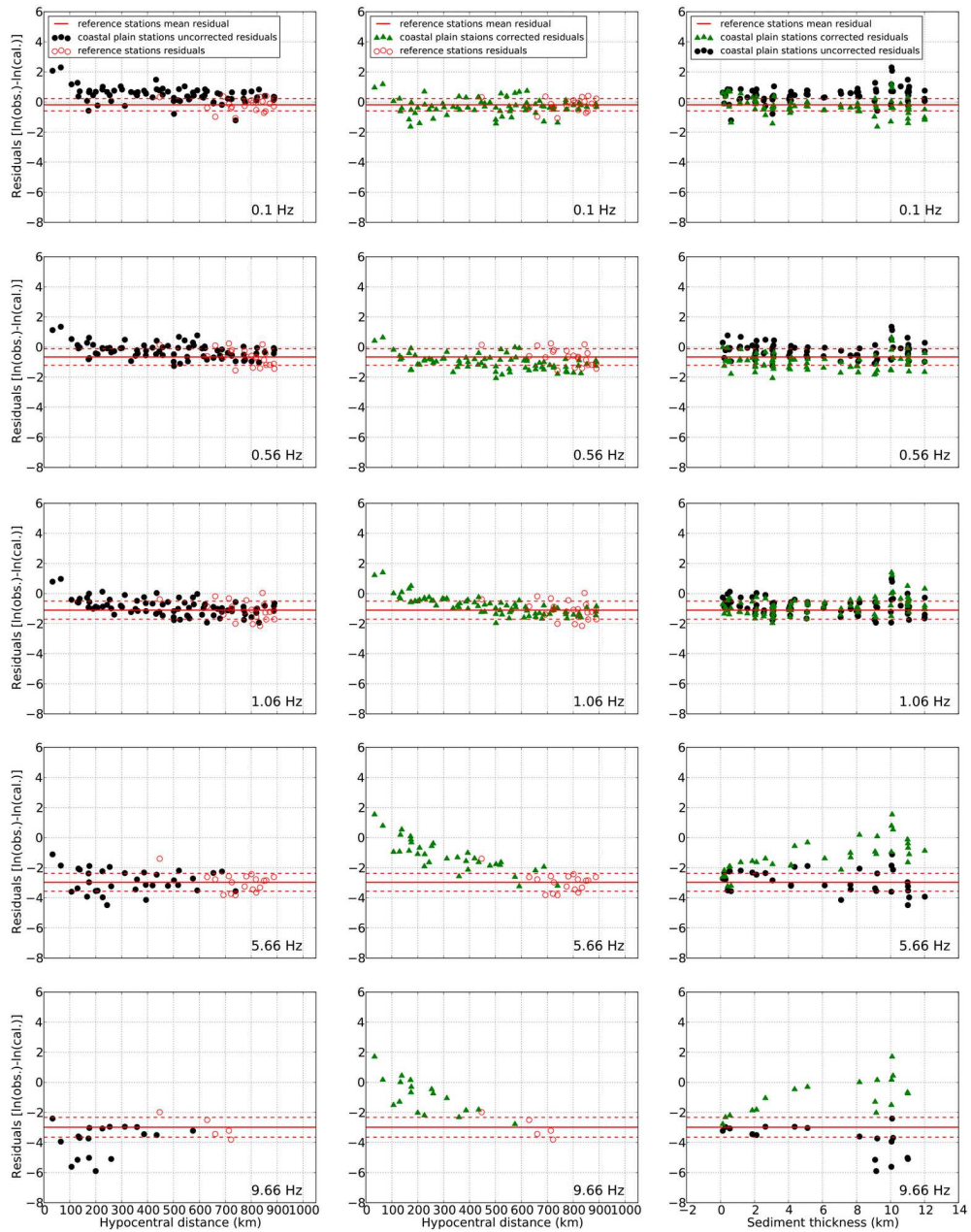


Figure 4.13: Same as Figure 4.10 but for the 20 October 2011 Texas earthquake.

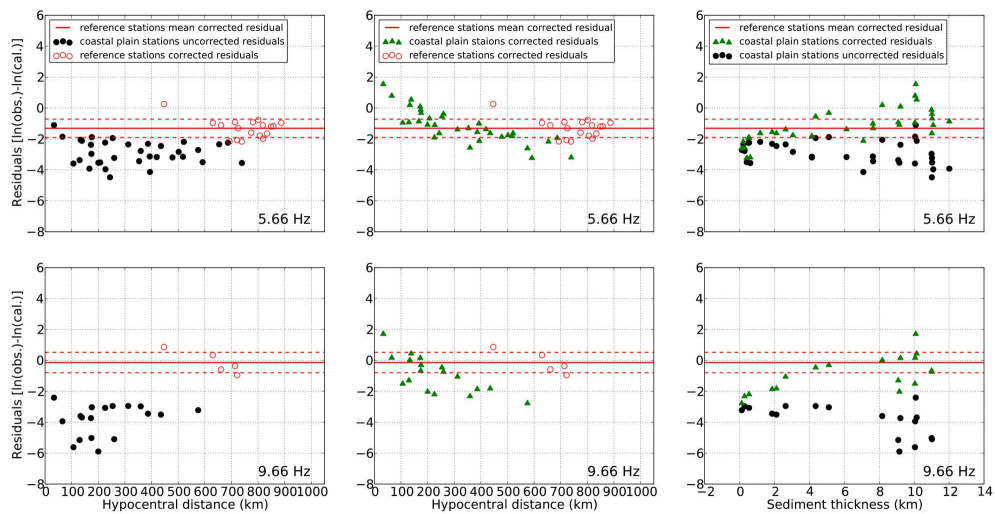


Figure 4.14: Same as the last two rows in Figure 4.13 except that the residuals at reference stations (open circles) have been corrected for the attenuation effects of the sediments near the earthquake source. The sediment thickness at the epicenter is 5.5 km.

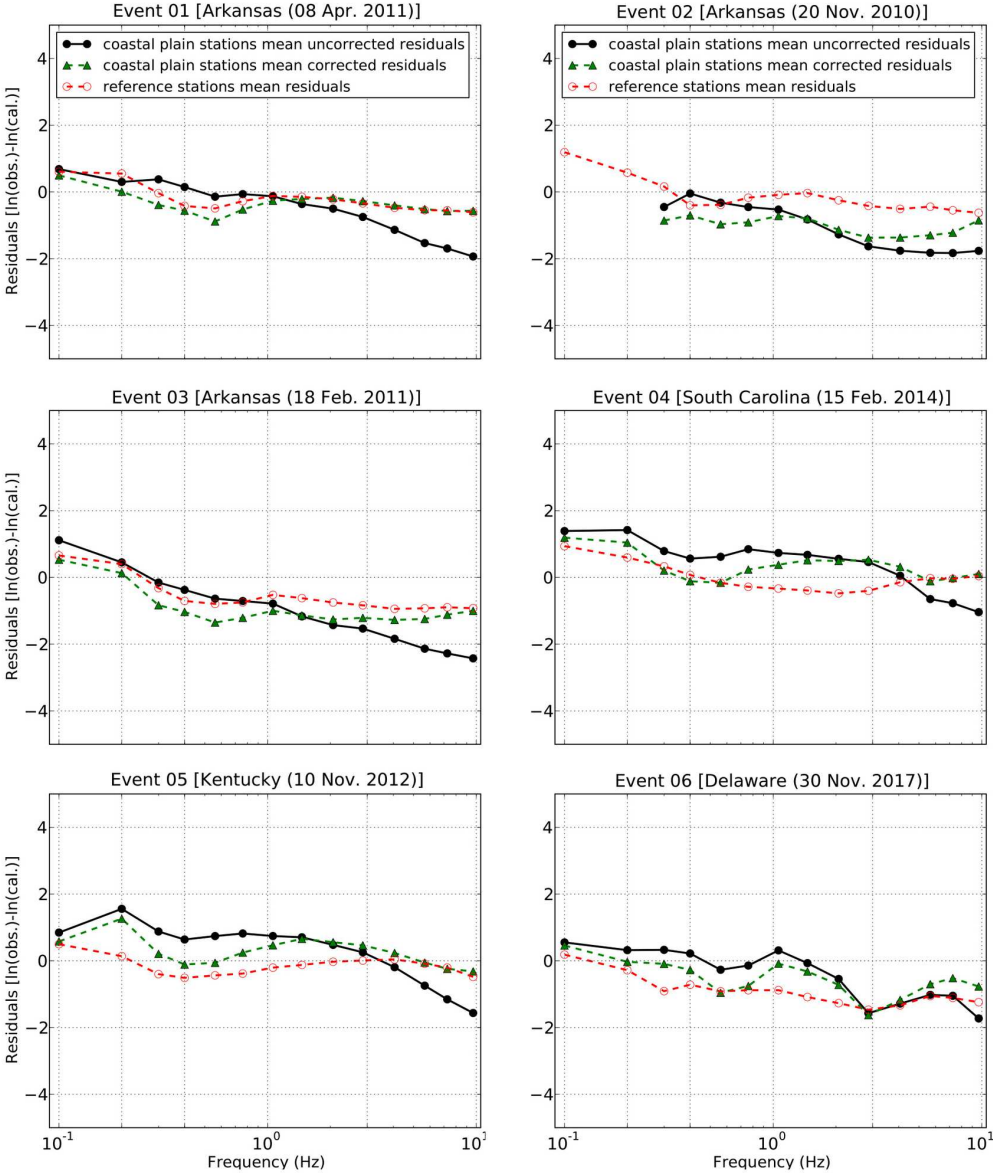


Figure 4.15: Mean residuals as a function of frequency for earthquake numbers 01-06 in Table 4.1. At each frequency, the mean residual is obtained by averaging all the residuals at the Coastal Plain stations or at the reference stations respectively.

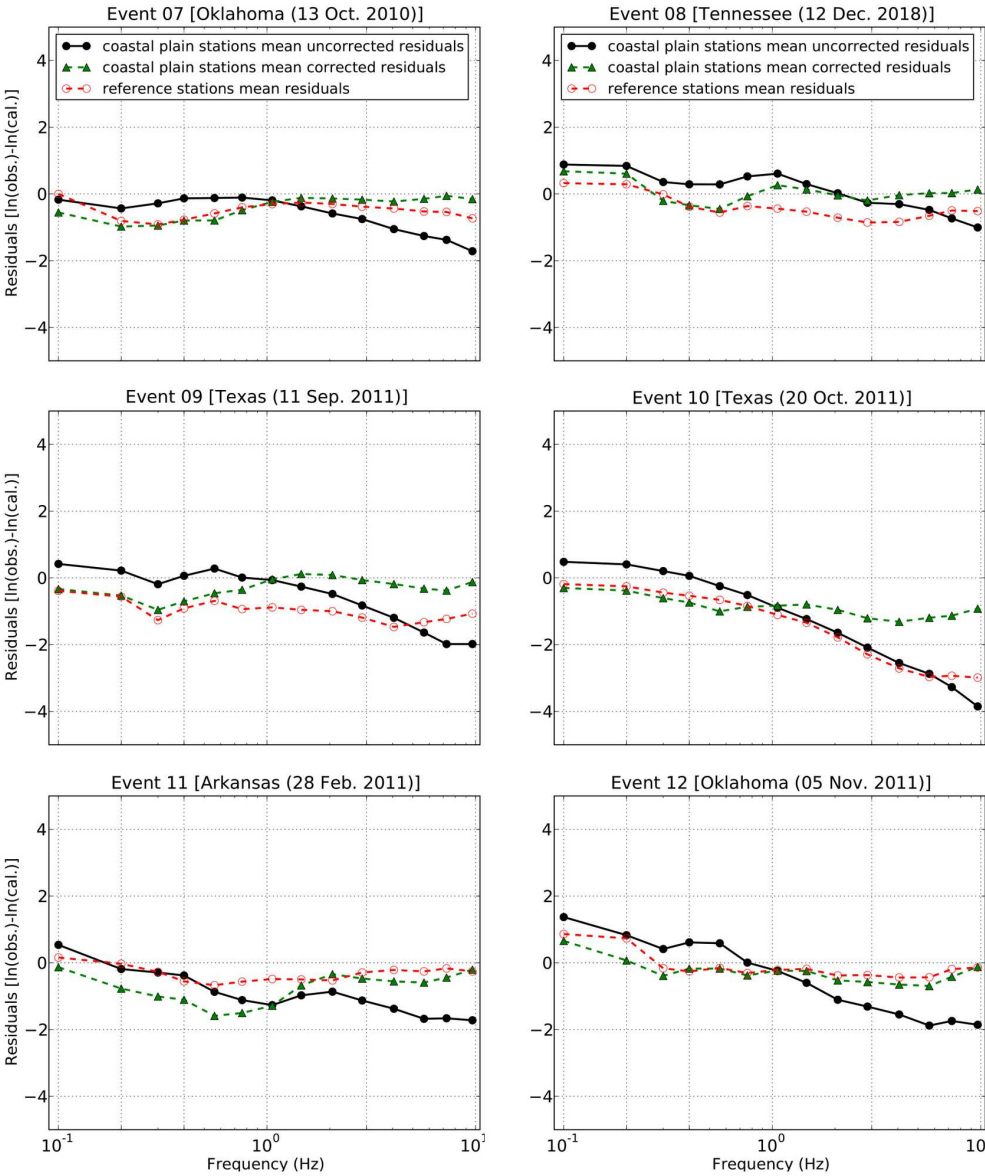


Figure 4.16: Same as Figure 4.15 but for earthquake numbers 07-12 in Table 4.1.

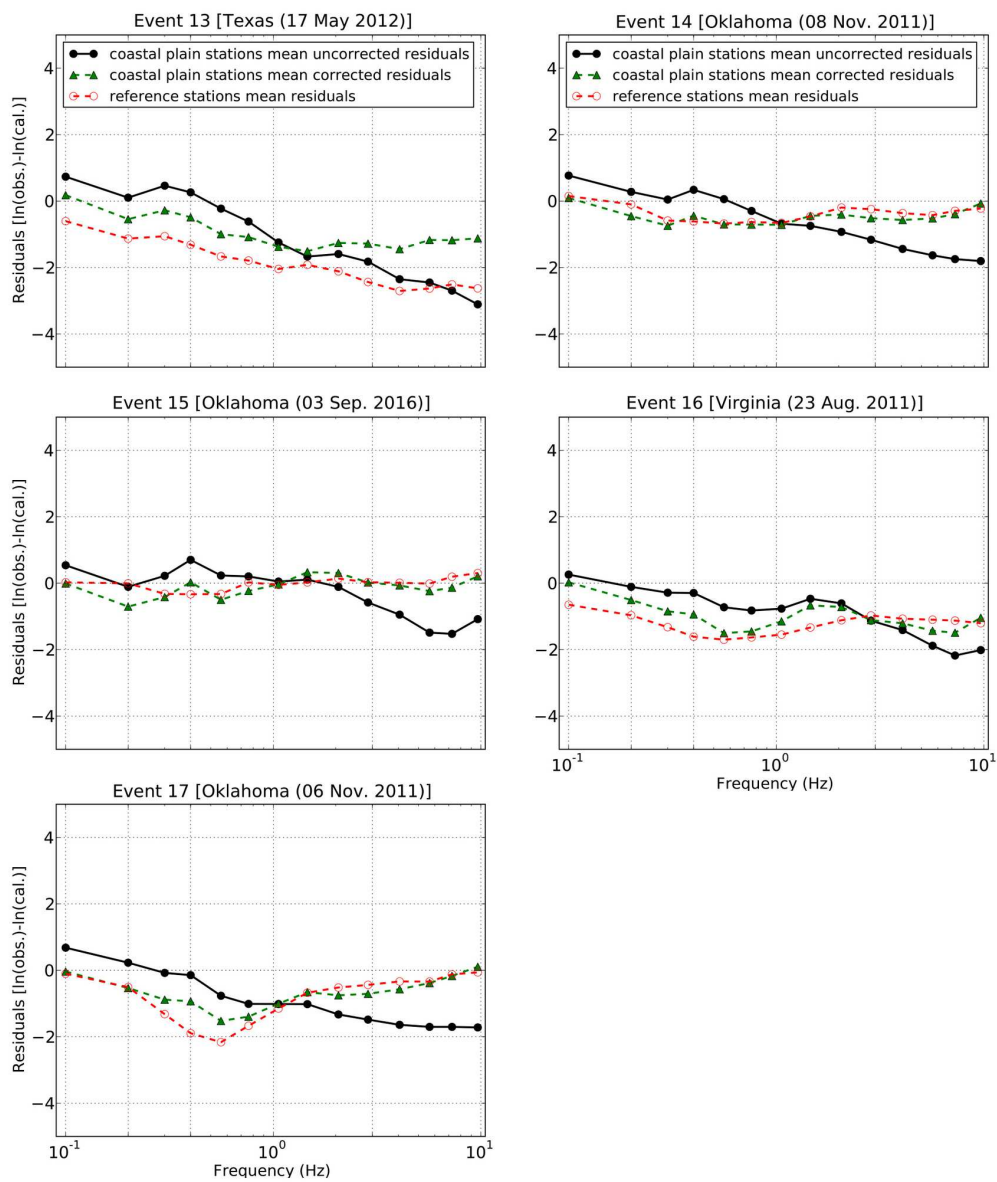


Figure 4.17: Same as Figure 4.15-4.16 but for earthquake numbers 13-17 in Table 4.1.

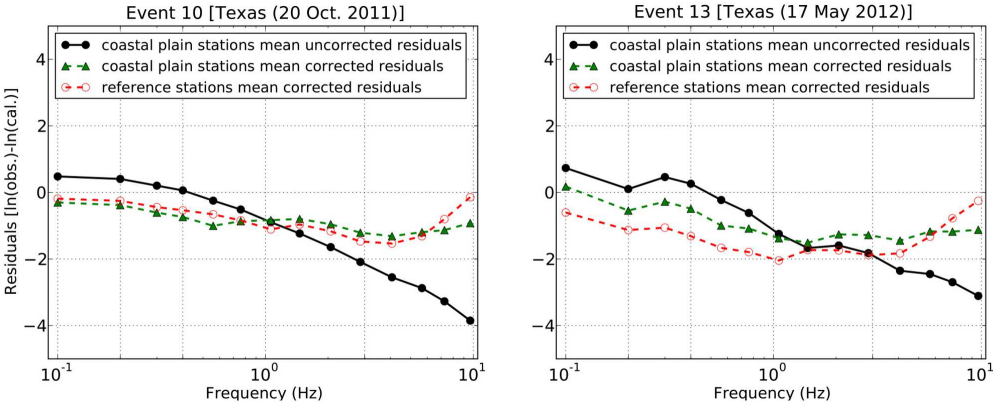


Figure 4.18: Mean residuals as a function of frequency for earthquake numbers 10 and 13 in Table 4.1 (located in the Coastal Plain of Texas). At each frequency, the mean residual is obtained by averaging all the residuals at the Coastal Plain stations or at the reference stations respectively. The residuals at reference stations outside the Coastal Plain have been corrected for attenuation effects of the sediments near the source.

Table 4.1: Earthquakes Used in This Study

event number	State	Date (mm/dd/yyyy)	Latitude (°)	Longitude (°)	Moment Magnitude	Depth (km)
01	Arkansas	04/08/2011	35.261	-92.362	3.86	4.0
02	Arkansas	11/20/2010	35.316	-92.317	3.87	5.0
03	Arkansas	02/18/2011	35.271	-92.377	4.07	8.0
04	South Carolina	02/15/2014	33.813	-82.063	4.11	5.0
05	Kentucky	11/10/2012	37.135	-82.978	4.16	14.0
06	Delaware	11/30/2017	39.205	-75.421	4.18	3.0
07	Oklahoma	10/13/2010	35.202	-97.309	4.33	14.0
08	Tennessee	12/12/2018	35.61	-84.74	4.35	4.0
09	Texas	09/11/2011	32.874	-100.804	4.41	5.0
10	Texas	10/20/2011	28.806	-98.147	4.59	3.0
11	Arkansas	02/28/2011	35.265	-92.34	4.65	4.0
12	Oklahoma	11/05/2011	35.57	-96.703	4.70	3.0
13	Texas	05/17/2012	31.902	-94.332	4.81	5.0
14	Oklahoma	11/08/2011	35.541	-96.754	4.83	8.0
15	Oklahoma	09/03/2016	36.429	-96.923	5.55	8.0
16	Virginia	08/23/2011	37.936	-77.933	5.65	6.0
17	Oklahoma	11/06/2011	35.537	-96.747	5.65	6.0

Table 4.2: Network Instruments Used in This Study

Network	Instrument type	Sample rate (sample/s)	Number of stations
TA	Broadband	40	429
US	Broadband	40	13
N4	Broadband	40,100	35
Z9	Broadband	50	35
LD	Broadband-short period	40,50,100	6

Table 4.3: Number of Recordings for Each Earthquake Used in This Study

Event number	Total recordings	Coastal Plain recordings	Distance range (km)
01	205	101	64 ~ 988
02	143	54	199 ~ 996
03	111	27	64 ~ 816
04	131	69	67 ~ 1000
05	157	92	218 ~ 996
06	41	8	170 ~ 986
07	156	56	39 ~ 898
08	97	26	68 ~ 991
09	127	77	112 ~ 897
10	67	45	33 ~ 893
11	167	71	66 ~ 900
12	217	111	24 ~ 998
13	138	68	34 ~ 997
14	193	99	25 ~ 900
15	35	13	116 ~ 964
16	25	17	434 ~ 893
17	220	109	26 ~ 984

Table 4.4: Linear Regression Coefficients of Natural Logarithms of Lg Fourier Spectra Amplitude Ratios as a Function of Sediment Thickness in Kilometers

Thickness range (Z) (km)		$0 < Z \leq Z_0$		$Z > Z_0$			
Center frequency (Hz)	Z_0 (km)	a_1	b_1	a_2	b_2	Error in a_2	Error in b_2
0.1	2.5	0.0	0.2449	0.4585	0.0615	0.0749	0.0092
0.3	0.8	0.0	1.0059	0.7935	0.0140	0.0400	0.0062
0.56	0.35	0.0	2.4482	0.8624	-0.0158	0.0381	0.0062
0.76	0.2	0.0	3.4803	0.7077	-0.0584	0.0373	0.0063
1.06	0.13	0.0	3.2598	0.4348	-0.0844	0.0386	0.0066
1.46	0.07	0.0	4.1536	0.2992	-0.1202	0.0401	0.0070
2.06	0.06	0.0	3.7848	0.2362	-0.1520	0.0423	0.0075
2.86	0.06	0.0	1.5930	0.1056	-0.1662	0.0458	0.0083

Table 4.5: Linear Regression Coefficients of Natural Logarithms of Lg Fourier Spectra Amplitude Ratios as a Function of Sediment Thickness in Kilometers at the 84 percentile level

Thickness range (Z) (km)		$0 < Z \leq Z_0$		$Z > Z_0$	
Center frequency (Hz)	Z_0 (km)	a_1	b_1	a_2	b_2
0.1	2.5	0.0	0.4916	1.0751	0.0615
0.3	0.8	0.0	1.8011	1.4297	0.014
0.56	0.35	0.0	4.4646	1.5681	-0.0158
0.76	0.2	0.0	7.2294	1.4576	-0.0584
1.06	0.13	0.0	9.3909	1.2318	-0.0844
1.46	0.07	0.0	16.1138	1.1364	-0.1202
2.06	0.06	0.0	18.444	1.1158	-0.152
2.86	0.06	0.0	17.2875	1.0472	-0.1662

Table 4.6: Linear Regression Coefficients of Natural Logarithms of Lg Fourier Spectra Amplitude Ratios as a Function of Sediment Thickness in Kilometers at the 16 percentile level

Thickness range (Z) (km)		$0 < Z \leq Z_0$		$Z > Z_0$	
Center frequency (Hz)	Z_0 (km)	a_1	b_1	a_2	b_2
0.1	2.5	0.0	-0.0017	-0.1581	0.0615
0.3	0.8	0.0	0.2107	0.1574	0.014
0.56	0.35	0.0	0.4317	0.1566	-0.0158
0.76	0.2	0.0	-0.2688	-0.0421	-0.0584
1.06	0.13	0.0	-2.8713	-0.3623	-0.0844
1.46	0.07	0.0	-7.8067	-0.5381	-0.1202
2.06	0.06	0.0	-10.8744	-0.6433	-0.152
2.86	0.06	0.0	-14.1015	-0.8361	-0.1662

Table 4.7: Seismic stations in the Coastal Plain

Station Name	Latitude (°)	Longitude (°)	Depth to Basement (km)
E02	29.443	-82.0674	1.07
E13	31.223	-82.0919	1.34
E15	31.3632	-82.0969	1.324
E17	31.5016	-82.0986	1.322
E18	31.5665	-82.0996	1.334
E19	31.6177	-82.1113	1.325
E20	31.6967	-82.0796	1.283
E21	31.738	-82.071	1.25
E22	31.8477	-82.0899	1.215
E23	31.8887	-82.0737	1.194
E24	31.9445	-82.097	1.197
E25	31.9918	-82.1135	1.184
E26	32.0979	-82.0991	1.145
E27	32.2362	-82.1091	1.048
E28	32.3359	-82.0967	0.981
E29	32.4908	-82.1032	0.863
E30	32.6958	-82.1091	0.678
E31	32.9866	-82.107	0.44
JCT	30.4794	-99.8022	0.145
NATX	31.7598	-94.661	4.918
OXF	34.5118	-89.4092	0.601
TIGA	31.4389	-83.5898	1.504
U45A	36.3481	-88.7635	0.244
V44A	35.8282	-89.8954	0.828
V45A	35.7403	-88.9591	0.251
VBMS	32.2185	-90.5177	7.016

Station Name	Latitude (°)	Longitude (°)	Depth to Basement (km)
W02	30.5774	-83.8902	2.482
W05	31.2724	-83.8978	1.79
W06	31.4486	-83.895	1.644
W07	31.611	-83.911	1.429
W11	31.9587	-83.9083	1.07
W12	32.0095	-83.8885	1.011
W13	32.055	-83.8933	0.924
W15A	32.138	-83.8985	0.815
W16	32.1794	-83.8841	0.751
W17	32.2427	-83.9045	0.724
W19	32.3132	-83.9064	0.543
W20	32.3665	-83.9198	0.493
W21	32.404	-83.8587	0.432
W22	32.4492	-83.8973	0.355
W23	32.5234	-83.886	0.301
W24	32.6437	-83.897	0.136
W42A	35.2732	-91.5224	0.321
W45A	35.1568	-89.186	0.337
W45B	35.1568	-89.186	0.337
W58A	35.0208	-79.2333	0.092
W59A	35.1673	-78.443	0.09
W60A	35.0528	-77.7133	0.277
WHTX	31.9913	-97.4561	0.29
X42A	34.5532	-91.6262	1.112
X44A	34.4998	-90.1462	1.109
X45A	34.4241	-89.3931	1.142

Station Name	Latitude (°)	Longitude (°)	Depth to Basement (km)
X57A	34.4643	-80.094	0.148
X58A	34.5548	-79.3388	0.152
X59A	34.572	-78.6023	0.153
X60A	34.5773	-77.9768	0.257
Y35A	33.9059	-97.0374	0.129
Y36A	33.8996	-96.2848	0.416
Y37A	33.9789	-95.621	0.415
Y38A	33.9278	-94.7311	0.218
Y39A	33.938	-94.0936	0.508
Y40A	34.0124	-93.2798	0.617
Y41A	33.8807	-92.6113	1.149
Y42A	33.8364	-91.7871	1.577
Y43A	33.9121	-90.9285	3.046
Y45A	33.8656	-89.5431	1.106
Y57A	34.017	-80.3915	0.21
Y58A	33.9057	-79.6665	0.316
Z34A	33.3712	-97.9158	0.01
Z35B	33.3309	-97.253	0.284
Z36A	33.2702	-96.4344	1.187
Z37A	33.1981	-95.6229	3.146
Z38A	33.2599	-94.9851	3.116
Z38B	33.2599	-94.9852	3.116
Z39A	33.2418	-94.1822	2.112
Z40A	33.2584	-93.3995	2.078
Z41A	33.2577	-92.803	2.562
Z42A	33.2739	-91.9474	2.039
Z43A	33.21	-91.2441	2.539
Z45A	33.3705	-89.6913	1.113

Station Name	Latitude (°)	Longitude (°)	Depth to Basement (km)
Z46A	33.1933	-88.9414	1.125
Z55A	33.2211	-82.1359	0.281
Z56A	33.3253	-81.3687	0.328
136A	32.4746	-96.5297	2.113
137A	32.5973	-95.7559	4.141
138A	32.6604	-95.0887	4.143
139A	32.6795	-94.3927	3.059
140A	32.6408	-93.574	3.056
141A	32.6046	-92.9049	4.091
142A	32.5488	-91.9457	4.023
143A	32.7032	-91.4036	2.03
144A	32.6304	-90.4226	4.078
145A	32.6035	-89.9287	3.093
146A	32.6368	-89.0573	1.164
146B	32.6368	-89.0573	1.164
153A	32.6499	-83.8316	0.22
154A	32.6131	-83.1066	0.445
155A	32.6219	-82.4665	0.636
157A	32.678	-80.9972	0.829
230A	31.8878	-101.112	0.02
232A	31.888	-99.6469	0.01
233A	32.0179	-98.8998	0.01
234A	32.004	-98.1368	0.146
236A	31.9997	-96.531	1.868
237A	32.0015	-95.8084	6.126
237B	32.0015	-95.8084	6.126
238A	32.0034	-95.1203	5.126

Station Name	Latitude (°)	Longitude (°)	Depth to Basement (km)
239A	32.0179	-94.4707	3.1
240A	32.0387	-93.7626	3.119
241A	32.0227	-92.9188	6.059
242A	32.0617	-92.1521	5.057
244A	32.0422	-90.6856	7.059
245A	32.0322	-89.8958	5.104
252A	31.9962	-84.7357	0.779
254A	31.9457	-83.2905	1.063
255A	31.9263	-82.4758	1.11
256A	31.9799	-81.8878	1.177
257A	31.9746	-81.0261	1.194
331A	31.3085	-100.427	0.005
334A	31.3325	-98.2379	0.157
335A	31.2819	-97.4271	0.417
337A	31.3159	-95.8854	7.65
338A	31.3567	-95.3106	7.637
339A	31.3331	-94.556	5.082
340A	31.4167	-93.8896	3.057
341A	31.3334	-93.1681	8.093
342A	31.3747	-92.3249	10.037
343A	31.2839	-91.6169	10.015
344A	31.4527	-90.7318	11.078
344B	31.4527	-90.7319	11.078
345A	31.308	-90.0309	9.134
352A	31.4793	-84.9274	1.465
353A	31.3474	-84.2172	1.577

Station Name	Latitude (°)	Longitude (°)	Depth to Basement (km)
355A	31.3438	-82.8518	1.283
356A	31.3247	-82.1275	1.33
435B	30.7827	-97.585	0.548
436A	30.7702	-96.796	4.359
438A	30.75	-95.4741	8.097
439A	30.7937	-94.766	7.09
440A	30.7456	-93.9587	8.059
441A	30.7498	-93.1898	9.053
441B	30.7498	-93.1898	9.053
442A	30.7119	-92.4314	12.015
444A	30.7153	-90.7463	11.04
445A	30.7303	-90.338	10.051
533A	30.0718	-99.0351	0.274
534A	30.0284	-98.4753	0.236
538A	30.2219	-95.49	11.059
539A	30.1084	-94.7236	11.015
540A	30.2093	-93.9796	11.01
541A	30.0596	-93.1875	12.0
542A	30.1247	-92.5513	11.999
543A	30.0856	-91.8557	12.004
633A	29.4591	-99.1766	0.72
636A	29.481	-97.057	9.09
638A	29.4193	-95.4481	12.008
733A	28.7192	-99.2939	5.169
734A	28.8473	-98.5576	3.121
735B	28.8553	-97.8082	10.09
736A	28.955	-97.0673	10.045
737A	28.7639	-96.4402	12.011
833A	28.3236	-99.3939	8.171